The Astrophysical Journal Supplement Series, 237:32 (36pp), 2018 August https://doi.org/10.3847/1538-4365/aacdf7

The Search for Spatial Extension in High-latitude Sources Detected by the *Fermi* Large Area Telescope

M. Ackermann[1], M. Ajello[2], L. Baldini[3], J. Ballet[4], G. Barbiellini[5,6], D. Bastieri[7,8], R. Bellazzini[9], E. Bissaldi[10,11], R. D. Blandford[12], E. D. Bloom[12], R. Bonino[13,14], E. Bottacini[12,15], T. J. Brandt[16], J. Bregeon[17], P. Bruel[18], R. Buehler[1], R. A. Cameron[12], R. Caputo[19], P. A. Caraveo[20], D. Castro[16,21], E. Cavazzuti[22], E. Charles[12], C. C. Cheung[23], G. Chiaro[20], S. Ciprini[24,25], J. Cohen-Tanugi[17], D. Costantin[8], S. Cutini[24,25], F. D'Ammando[26,27], F. de Palma[11,28], A. Desai[2], N. Di Lalla[3], M. Di Mauro[12], L. Di Venere[10,11], C. Favuzzi[10,11], J. Finke[23], A. Franckowiak[1], Y. Fukazawa[29], S. Funk[30], P. Fusco[10,11], F. Gargano[11], D. Gasparrini[24,25], N. Giglietto[10,11], F. Giordano[10,11], M. Giroletti[26], D. Green[16,31], I. A. Grenier[4], L. Guillemot[32,33], S. Guiriec[16,34], E. Hays[16], J. W. Hewitt[35], D. Horan[18], G. Jóhannesson[36,37], S. Kensei[29], M. Kuss[9], S. Larsson[38,39], L. Latronico[13], M. Lemoine-Goumard[40], J. Li[41], F. Longo[5,6], F. Loparco[10,11], M. N. Lovellette[23], P. Lubrano[25], J. D. Magill[31], S. Maldera[13], A. Manfreda[3], M. N. Mazziotta[11], J. E. McEnery[16,31], M. Meyer[12], T. Mizuno[42], M. E. Monzani[12], A. Morselli[43], I. V. Moskalenko[12], M. Negro[13,14], E. Nuss[17], N. Omodei[12], M. Orienti[26], E. Orlando[12], J. F. Ormes[44], M. Palatiello[5,6], V. S. Paliya[2], D. Paneque[45], J. S. Perkins[16], M. Persic[5,46], M. Pesce-Rollins[9], F. Piron[17], T. A. Porter[12], G. Principe[30], S. Rainò[10,11], R. Rando[7,8], B. Rani[16], S. Razzaque[47], A. Reimer[12,48], O. Reimer[12,48], T. Reposeur[40], C. Sgrò[9], E. J. Siskind[49], G. Spandre[9], P. Spinelli[10,11], D. J. Suson[50], H. Tajima[12,51], J. B. Thayer[12], L. Tibaldo[52,53], D. F. Torres[41,54], G. Tosti[25,55], J. Valverde[18], T. M. Venters[16], M. Vogel[56], K. Wood[57], M. Wood[12], G. Zaharijas[58,59]

The *Fermi*-LAT Collaboration, and

J. Biteau[60]

[1] Deutsches Elektronen Synchrotron DESY, D-15738 Zeuthen, Germany
[2] Department of Physics and Astronomy, Clemson University, Kinard Lab of Physics, Clemson, SC 29634-0978, USA
[3] Università di Pisa and Istituto Nazionale di Fisica Nucleare, Sezione di Pisa I-56127 Pisa, Italy
[4] Laboratoire AIM, CEA-IRFU/CNRS/Université Paris Diderot, Service d'Astrophysique, CEA Saclay, F-91191 Gif sur Yvette, France
[5] Istituto Nazionale di Fisica Nucleare, Sezione di Trieste, I-34127 Trieste, Italy
[6] Dipartimento di Fisica, Università di Trieste, I-34127 Trieste, Italy
[7] Istituto Nazionale di Fisica Nucleare, Sezione di Padova, I-35131 Padova, Italy
[8] Dipartimento di Fisica e Astronomia "G. Galilei," Università di Padova, I-35131 Padova, Italy
[9] Istituto Nazionale di Fisica Nucleare, Sezione di Pisa, I-56127 Pisa, Italy
[10] Dipartimento di Fisica "M. Merlin" dell'Università e del Politecnico di Bari, I-70126 Bari, Italy
[11] Istituto Nazionale di Fisica Nucleare, Sezione di Bari, I-70126 Bari, Italy
[12] W.W. Hansen Experimental Physics Laboratory, Kavli Institute for Particle Astrophysics and Cosmology, Department of Physics and SLAC National Accelerator Laboratory, Stanford University, Stanford, CA 94305, USA; mameyer@stanford.edu, mdwood@slac.stanford.edu
[13] Istituto Nazionale di Fisica Nucleare, Sezione di Torino, I-10125 Torino, Italy
[14] Dipartimento di Fisica, Università degli Studi di Torino, I-10125 Torino, Italy
[15] Department of Physics and Astronomy, University of Padova, Vicolo Osservatorio 3, I-35122 Padova, Italy
[16] NASA Goddard Space Flight Center, Greenbelt, MD 20771, USA
[17] Laboratoire Univers et Particules de Montpellier, Université Montpellier, CNRS/IN2P3, F-34095 Montpellier, France
[18] Laboratoire Leprince-Ringuet, École polytechnique, CNRS/IN2P3, F-91128 Palaiseau, France
[19] Center for Research and Exploration in Space Science and Technology (CRESST) and NASA Goddard Space Flight Center, Greenbelt, MD 20771, USA regina.caputo@nasa.gov
[20] INAF-Istituto di Astrofisica Spaziale e Fisica Cosmica Milano, via E. Bassini 15, I-20133 Milano, Italy
[21] Harvard-Smithsonian Center for Astrophysics, Cambridge, MA 02138, USA
[22] Italian Space Agency, Via del Politecnico snc, I-00133 Roma, Italy
[23] Space Science Division, Naval Research Laboratory, Washington, DC 20375-5352, USA
[24] Space Science Data Center—Agenzia Spaziale Italiana, Via del Politecnico, snc, I-00133, Roma, Italy
[25] Istituto Nazionale di Fisica Nucleare, Sezione di Perugia, I-06123 Perugia, Italy
[26] INAF Istituto di Radioastronomia, I-40129 Bologna, Italy
[27] Dipartimento di Astronomia, Università di Bologna, I-40127 Bologna, Italy
[28] Università Telematica Pegaso, Piazza Trieste e Trento, 48, I-80132 Napoli, Italy
[29] Department of Physical Sciences, Hiroshima University, Higashi-Hiroshima, Hiroshima 739-8526, Japan
[30] Friedrich-Alexander-Universität Erlangen-Nürnberg, Erlangen Centre for Astroparticle Physics, Erwin-Rommel-Str. 1, D-91058 Erlangen, Germany
[31] Department of Astronomy, University of Maryland, College Park, MD 20742, USA
[32] Laboratoire de Physique et Chimie de l'Environnement et de l'Espace—Université d'Orléans / CNRS, F-45071 Orléans Cedex 02, France
[33] Station de radioastronomie de Nançay, Observatoire de Paris, CNRS/INSU, F-18330 Nançay, France
[34] The George Washington University, Department of Physics, 725 21st St, NW, Washington, DC 20052, USA
[35] University of North Florida, Department of Physics, 1 UNF Drive, Jacksonville, FL 32224, USA
[36] Science Institute, University of Iceland, IS-107 Reykjavik, Iceland
[37] KTH Royal Institute of Technology and Stockholm University, Roslagstullsbacken 23, SE-106 91 Stockholm, Sweden
[38] Department of Physics, KTH Royal Institute of Technology, AlbaNova, SE-106 91 Stockholm, Sweden
[39] The Oskar Klein Centre for Cosmoparticle Physics, AlbaNova, SE-106 91 Stockholm, Sweden
[40] Centre d'Études Nucléaires de Bordeaux Gradignan, IN2P3/CNRS, Université Bordeaux 1, BP120, F-33175 Gradignan Cedex, France
[41] Institute of Space Sciences (CSICIEEC), Campus UAB, Carrer de Magrans s/n, E-08193 Barcelona, Spain
[42] Hiroshima Astrophysical Science Center, Hiroshima University, Higashi-Hiroshima, Hiroshima 739-8526, Japan
[43] Istituto Nazionale di Fisica Nucleare, Sezione di Roma "Tor Vergata," I-00133 Roma, Italy
[44] Department of Physics and Astronomy, University of Denver, Denver, CO 80208, USA
[45] Max-Planck-Institut für Physik, D-80805 München, Germany

[46] Osservatorio Astronomico di Trieste, Istituto Nazionale di Astrofisica, I-34143 Trieste, Italy
[47] Department of Physics, University of Johannesburg, P.O. Box 524, Auckland Park 2006, South Africa
[48] Institut für Astro- und Teilchenphysik and Institut für Theoretische Physik, Leopold-Franzens-Universität Innsbruck, A-6020 Innsbruck, Austria
[49] NYCB Real-Time Computing Inc., Lattingtown, NY 11560-1025, USA
[50] Purdue University Northwest, Hammond, IN 46323, USA
[51] Solar-Terrestrial Environment Laboratory, Nagoya University, Nagoya 464-8601, Japan
[52] CNRS, IRAP, F-31028 Toulouse cedex 4, France
[53] GAHEC, Universit de Toulouse, UPS-OMP, IRAP, F-31400 Toulouse, France
[54] Institució Catalana de Recerca i Estudis Avançats (ICREA), E-08010 Barcelona, Spain
[55] Dipartimento di Fisica, Università degli Studi di Perugia, I-06123 Perugia, Italy
[56] California State University, Los Angeles, Department of Physics and Astronomy, Los Angeles, CA 90032, USA
[57] Praxis Inc., Alexandria, VA 22303, resident at Naval Research Laboratory, Washington, DC 20375, USA
[58] Istituto Nazionale di Fisica Nucleare, Sezione di Trieste, and Università di Trieste, I-34127 Trieste, Italy
[59] Center for Astrophysics and Cosmology, University of Nova Gorica, Nova Gorica, Slovenia
[60] Institut de Physique Nucléaire, Université Paris-Sud, Univ. Paris/Saclay, 15 rue Georges Clemenceau, 91406 Orsay, Cedex, France
Received 2018 April 17; revised 2018 June 14; accepted 2018 June 14; published 2018 August 7

Abstract

We present a search for spatial extension in high-latitude ($|b| > 5°$) sources in recent *Fermi* point source catalogs. The result is the *Fermi* High-Latitude Extended Sources Catalog, which provides source extensions (or upper limits thereof) and likelihood profiles for a suite of tested source morphologies. We find 24 extended sources, 19 of which were not previously characterized as extended. These include sources that are potentially associated with supernova remnants and star-forming regions. We also found extended γ-ray emission in the vicinity of the Cen A radio lobes and—at GeV energies for the first time—spatially coincident with the radio emission of the SNR CTA 1, as well as from the Crab Nebula. We also searched for halos around active galactic nuclei, which are predicted from electromagnetic cascades induced by the e^+e^- pairs that are deflected in intergalactic magnetic fields. These pairs are produced when γ-rays interact with background radiation fields. We do not find evidence for extension in individual sources or in stacked source samples. This enables us to place limits on the flux of the extended source components, which are then used to constrain the intergalactic magnetic field to be stronger than 3×10^{-16} G for a coherence length $\lambda \gtrsim 10$ kpc, even when conservative assumptions on the source duty cycle are made. This improves previous limits by several orders of magnitude.

Key words: BL Lacertae objects: general – catalogs – gamma rays: general – ISM: H II Regions – ISM: supernova remnants

1. Introduction

Extended γ-ray sources provide a unique probe into a plethora of physics topics, ranging from the acceleration of relativistic particles and emission of (very) high-energy γ-rays to searches for new physics. Known astrophysical sources from which spatial extension has been observed at γ-ray energies include supernova remnants (SNRs, Aharonian et al. 2006; Acero et al. 2016b), pulsar wind nebulae (PWNe, Grondin et al. 2013; Abdalla et al. 2017), and molecular clouds (Strong et al. 1982; Aharonian et al. 2008). Star-forming regions (SFRs) may constitute an additional extended γ-ray source class; one has been identified so far at γ-ray energies, namely the Cygnus Cocoon (Ackermann et al. 2011). Furthermore, spatial extension at γ-ray energies has been detected from nearby galaxies, such as the Magellanic Clouds (Abdo et al. 2010a; Ackermann et al. 2016c) and M31 (Ackermann et al. 2017a), as well as from the lobes of active galactic nuclei (AGNs), such as Cen A (Abdo et al. 2010b).

Extended γ-ray emission from otherwise point-like AGN could be due to electromagnetic cascades (Protheroe & Stanev 1993). The γ-rays interact with photons of the extragalactic background light (EBL, Hauser & Dwek 2001; Kashlinsky 2005) to form e^+e^- pairs (Nikishov 1962; Gould & Schréder 1967a, 1967b; Dwek & Krennrich 2013). The e^+e^- pairs can, in turn, inverse-Compton (IC) scatter photons of the cosmic microwave background (CMB), thereby initiating the cascade. The pairs are deflected in the intergalactic magnetic field (IGMF); depending on its strength and coherence length, an extended γ-ray halo may form around AGNs, often referred to as pair halo beam-broadened cascades (Aharonian et al. 1994). The cascade emission can also lead to an excess in the GeV regime of γ-ray spectra, and the non-observation of this feature has been used to derive lower limits on the IGMF strength—or conversely, on the filling factor of the IGMF (Neronov & Vovk 2010; Dolag et al. 2011; Tavecchio et al. 2011; Taylor et al. 2011; Vovk et al. 2012). These limits depend on the activity time of AGNs (Dermer et al. 2011; Finke et al. 2015) and on their intrinsic spectra (Arlen et al. 2014).

Apart from the intrinsic extension of astrophysical objects, extended emission from unidentified γ-ray emitters that lack a counterpart at other wavelengths can be used to probe the nature of dark matter (DM). The observed universe includes a significant component of matter that does not interact like any known field in the Standard Model of particle physics. Though solid observational evidence exists for the gravitational influence of DM from the earliest moments of the universe's history to the present day, no direct measurements have been made (Zwicky 1933; Rubin et al. 1980; Olive 2003). For instance, extended emission should be produced in the case of the annihilation or decay of weakly interacting massive particles gravitationally bound in virialized sub-structures of the halo of the Milky Way (e.g., Kuhlen et al. 2008; Pieri et al. 2008; Mirabal et al. 2012; Zechlin & Horns 2012).

The above searches for source extension profit from the all-sky survey of the Large Area Telescope (LAT) on board the *Fermi* satellite, which detects γ-rays with energies from 20 MeV to over 300 GeV (Atwood et al. 2009). It has

discovered a wealth of γ-ray sources, culminating in the two most recent γ-ray source catalogs: the *Fermi* Third Source Catalog (3FGL, Acero et al. 2015) and Third Hard-Source Catalog (3FHL, Ajello et al. 2017). Together, these two catalogs contain more than 3000 sources. With the release of the latest event selection and reconstruction software, and associated analysis tools (`Pass 8`, Atwood et al. 2012), the reconstruction of the photon arrival directions has improved significantly: a reduction of the 68% containment radius of the point-spread function (PSF), particularly at high energies (>10 GeV), has been demonstrated by the 3FHL. In combination with an eight-year data set, this provides an improved sensitivity to our search for spatial extensions.

This work follows several previous searches for spatially extended sources at GeV energies. Lande et al. (2012) reported the first systematic search for spatially extended sources in LAT data; they identified 21 extended sources, based on an analysis of two years of `Pass 7` data. The most recent search for extended sources, the Fermi Galactic Extended Source Catalog (FGES), looked for new sources within 7° of the Galactic Plane, using six years of `Pass 8` data above 10 GeV (Ackermann et al. 2017c). This search reported 46 extended sources, eight of which were new extended sources with clear associations. Counting all FGES associated sources, as well as sources found in other dedicated analyses, the LAT has detected 55 extended sources.

We report here on the *Fermi* High-Latitude Extended Sources Catalog (FHES), a comprehensive search for spatially extended γ-ray sources above 5° Galactic latitude using 7.5 years of `Pass 8` data above 1 GeV. The FHES encompasses a region of the sky complementary to the FGES, which only considered low Galactic latitudes. The FHES has a lower energy threshold than FGES because we remove the region of the Galactic Ridge where the emission coming from the interstellar medium is very large at 1 GeV. Due to its lower energy threshold, the FHES is also sensitive to source populations with softer spectra.

In Section 2, we discuss the *Fermi*-LAT instrument and the data set, sources, and background models used for this analysis, as well as the methodology developed to build the extended source catalog. The catalog and a study of individual objects are described in Section 3. In Section 4, we turn to sources located at $|b| > 20°$ that show weak evidence for extension, and present a source stacking analysis of AGN samples in the search of pair-halo emission. Due to the absence of a clear pair-halo signal, we derive limits on the IGMF in Section 5. Finally, we conclude in Section 6.

2. Fermi-LAT Data and Analysis

The *Fermi*-LAT is a pair-conversion telescope. Incoming γ-rays pass through the anti-coincidence detector and convert in the tracker to e^+e^- pairs. The charged particle direction is reconstructed using the information in the tracker, and the energy is estimated from depositions in the calorimeter. Detailed descriptions of the LAT and its performance can be found in dedicated papers (Atwood et al. 2009, 2012).

2.1. Data Selection

We analyze 90 months of LAT data (2008 August 4 to 2016 February 4) and select the `P8R2 SOURCE` class of events, which is the recommended class for most analyses and provides good sensitivity for analysis of point sources and extended sources.[61] The `Pass 8` data benefit from an improved PSF, effective area, and energy reach. More accurate Monte Carlo simulations of the detector and the environment in low-Earth orbit (Atwood et al. 2012) have reduced the systematic uncertainty in the LAT instrument response functions (IRFs). We have selected events in the energy range from 1 GeV to 1 TeV, which is determined by the angular resolution at lower energies and declining acceptance with increasing energy. Each source is analyzed with a binned maximum-likelihood analysis, using eight logarithmic bins per decade in energy and a region of interest (ROI) of 6° × 6° with an angular pixelization of 0°.025. We summarize our data selection in Table 1.

Table 1
Summary of *Fermi*-LAT Data Selection Criteria

Selection	Criteria
Observation Period	2008 August 4 to 2016 February 4
Mission Elapsed Time (s)[a]	239557414 to 476239414
Energy Range	1 GeV-1 TeV
Fit Regions	6°.0 × 6°.0 ($\|b\| > 5°$; 2689 ROIs)
Zenith Range	$\theta_z < 100°$
Data Quality Cut[b]	`DATA_QUAL==1` `LAT_CONFIG==1`

Notes.
[a] *Fermi* Mission Elapsed Time is defined as seconds since 2001 January 1, 00:00:00 UTC.
[b] Standard data quality selection with the *gtmktime* Science Tool.

Within the different event classes, `Pass 8` offers *event types*, subdivisions based on event-by-event uncertainties in the directional and energy measurements, which can increase the sensitivity of likelihood-based analyses. In this work, we use the set of four PSF event-type selections that subdivide the events in our data sample according to the quality of their directional reconstruction. Specifically, the data sample is split by event type into two data selections that are analyzed in a joint likelihood: `evtype` = 32 (PSF3, which corresponds to the best quality of angular reconstruction) and `evtype` = 28 (PSF0+PSF1+PSF2). We choose to combine the three worst PSF event types for computational efficiency. In Monte Carlo studies, we found that PSF3 events provide most of the power for distinguishing between point-like and extended hypotheses. The data reduction and exposure calculations are performed using the LAT *ScienceTools* version 11-05-03,[62] *fermipy* (Wood et al. 2017) version 00-15-01,[63] and the `P8R2_SOURCE_V6` IRFs. We enable the correction for energy dispersion for all model components except the Galactic diffuse and isotropic components.

We perform an independent analysis on 2469 and 220 ROIs centered on the positions of the sources with $|b| > 5°$ listed in the 3FGL and 3FHL, respectively. Among the 3FHL sources considered, we exclude sources that have an association with a 3FGL source or an angular separation from a 3FGL source that is less than twice its 95% positional uncertainty. The analysis procedure is outlined in Section 2.2. The cut on Galactic

[61] https://fermi.gsfc.nasa.gov/ssc/data/analysis/documentation/Cicerone/Cicerone_Data/LAT_DP.html
[62] http://fermi.gsfc.nasa.gov/ssc/data/analysis/software
[63] http://fermipy.readthedocs.io

latitude is chosen to avoid regions where systematic errors in the diffuse emission model could bias the measurement of the angular extension or produce spurious detections. We additionally exclude the following 3FGL and 3FHL sources:

1. SMC (3FGL J0059.0−7242e)
2. LMC (3FGL J0526.6−6825e) and four sources in the vicinity of the LMC (3FGL J0524.5–6937, 3FGL J 0525.2–6614, 3FGL J0456.2–6924, and 3FHL J0537.9–6909)
3. Cygnus Loop (3FGL J2051.0+3040e)
4. Cen A Lobes (3FGL J1324.0−4330e)

Those sources have angular sizes that are comparable to, or significantly larger than, our chosen ROI size of $6^\circ \times 6^\circ$. In the case of the LMC, Cygnus Loop, and Cen A Lobes, these sources also have complex morphologies that are not approximated well by the disk and Gaussian models that we use in the present work when testing for angular extension. Note that, while we exclude the LMC and SMC from our analysis, we model the emission from these regions using the spatial templates from the 3FHL. Our sample includes four sources that were modeled as point-like objects in the 3FGL but have subsequently been measured to have angular extension: Fornax A (Ackermann et al. 2016b), SNR G295.5 +09.7 (Acero et al. 2016b), SNR G150.3+04.5 (Ackermann et al. 2016a), and M31 (Ackermann et al. 2017a). These sources were handled consistently with all other potentially extended sources in the fitting procedure.

For the Crab and CTA 1 pulsars (3FGL J0534.5+2201 and 3FGL J0007.1+7303), we use pulsar phase information to constrain pulsar emission in these regions. For CTA 1, we use an eight-year ephemeris derived from `Pass 8` LAT data above 100 MeV (Kerr et al. 2015). For the Crab Pulsar, we use an ephemeris derived from radio observations with the Jodrell Bank telescope (Lyne et al. 1993).[64]

2.2. ROI Model and Optimization

For each ROI, we start from a baseline model that includes sources from the 3FGL and standard templates for isotropic and Galactic diffuse emission.[65] We include 3FGL sources in a $10^\circ \times 10^\circ$ region centered on the ROI. We model each 3FGL source using the same spectral parameterization as used in the 3FGL. The 3FGL uses one of three different spectral parameterizations depending on the source association and evidence for spectral curvature: power law (PL), log-parabola (LP), and power law with exponential cutoff (PLE). We switch to the LP parameterization for all PL sources detected in our analysis with Test Statistic (Chernoff 1954), (TS) > 100. This ensures that we have an accurate model for background sources that may show spectral curvature, and it comes without loss of generality because the PL is a special case of an LP. For extended sources, we use the spatial models from the 3FHL (Ackermann et al. 2017b) that include new or improved spatial templates for some high-latitude extended sources, including the LMC, Fornax A, and SNR G150.3+4.5.

An extended source could be characterized as a cluster of point sources in the 3FGL because the 3FGL does not include a criterion for distinguishing between point-like and extended emission. Therefore, the baseline model excludes 3FGL sources that are unassociated and have either TS < 100 or analysis flags indicating confusion with diffuse emission (flags 5, 6, or 8). Removing unassociated sources ensures that the characterization of new extended sources is not biased by the 3FGL sources included in the baseline model. If the unassociated sources are genuine point sources, they will be added back into the model in the course of the ROI optimization (see below).

Starting from the baseline model, we proceed to optimize the model by fitting the spectral and spatial properties of the model components. We illustrate the analysis procedure in the flow chart in Figure 1. We first fit the spectral parameters (flux normalization and spectral shape parameters) of the Galactic interstellar emission model and all sources in the model with an amplitude of at least one expected photon for the initial 3FGL model parameters. We then individually fit the positions of all point sources that are inside the ROI and $>0.^\circ1$ from the ROI boundary. When fitting the position of a source, we fix its spectral shape parameters but refit its normalization. After relocalizing point sources, we re-fit the spectral parameters of all model components.

After optimizing the parameters of the baseline model components, we further refine the model by identifying and adding new point source candidates. The identification of new point sources is performed in two successive passes, focusing on the outer ($R > R_{\rm inner}$) and inner ($R \leqslant R_{\rm inner}$) ROI, where R is the angular distance from the ROI center and $R_{\rm inner} = 1.^\circ0$. Sources found to be significantly extended (having a test statistic of extension, $\mathrm{TS_{ext}}$, >16) are reanalyzed with $R_{\rm inner} = 1.^\circ5$ to minimize bias from point sources that are confused with the target source.

In the first pass, we use a likelihood-based source-finding algorithm to look for point sources with $R > R_{\rm inner}$. We identify candidates by generating a TS map for a point source that has a PL spectrum with a PL index $\Gamma = 2$. When generating the TS map, we fix the parameters of the background sources and fit only the amplitude of the test source. We add a source at every peak in the TS map with $R > R_{\rm inner}$ and TS > 9 that is at least $0.^\circ5$ from a peak with higher TS. New source candidates are modeled with a PL if the source is detected with TS < 100, and an LP otherwise. Both the normalization and spectral shape (Γ for PL, and index α and curvature β for LP) parameters of new source candidates are fit in this procedure. We then generate a new TS map after adding the point sources to the model and repeat the procedure until no candidates are found satisfying our criteria ($R > R_{\rm inner}$, TS > 9). After completing the search for point sources in the outer ROI, we re-fit the normalization and spectral shape parameters of all model components.

In the final pass of the analysis, we look for new point-source candidates in the inner ROI while simultaneously testing the central source for extension. The analysis proceeds iteratively, as follows, for two independent hypotheses that we denote as extension (extended source) and halo (extended source plus a superimposed point source):

1. We perform tests for extension (as described in the next paragraph) against the null model with n point sources in the inner ROI (n includes the source of interest but excludes 3FGL point sources included in the baseline model).

[64] http://www.jb.man.ac.uk/~pulsar/crab.html

[65] Galactic IEM: gll iem v06.fits, Isotropic: iso P8R2 SOURCE V6 v06.txt. Please see: http://fermi.gsfc.nasa.gov/ssc/data/access/lat/BackgroundModels.html.

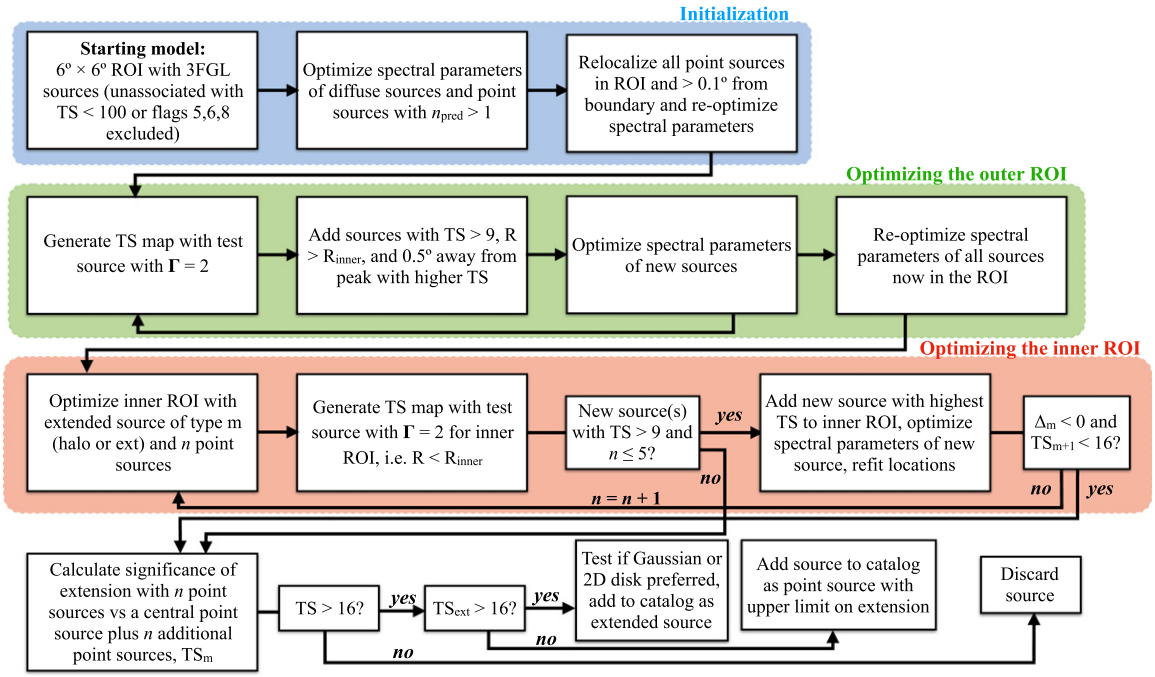

Figure 1. Flow chart for the analysis procedure. See text for further details.

2. We derive a model with $n+1$ point sources by searching for additional point sources with TS > 9 in the inner ROI using the same source-finding algorithm that was applied in the outer ROI optimization. If a peak with TS > 9 is found in the TS map, we add a new point source at this location. If more than one source candidate is found, we select the one with the highest peak TS. We then individually refit the source positions of the central source and any point sources added up to this iteration in the inner ROI, starting from the source with the highest TS.
3. We repeat steps 1 and 2 until we find that the extension/halo hypothesis is preferred over a model with $n+1$ point sources (according to the criteria in Equations (1) and (2)), no point sources with TS > 9 are found in the source-finding step, or the number of iterations exceeds five.

At each iteration n, we test for extended emission by comparing the likelihood of the hypothesis with a central point source and n additional point sources ($\mathcal{L}_n$) versus the likelihoods for two alternative hypotheses: replacing the central source with a symmetric 2D Gaussian ($\mathcal{L}_{n+\mathrm{ext}}$), and superimposing a 2D symmetric Gaussian on the central source ($\mathcal{L}_{n+\mathrm{halo}}$) (with n additional point sources). For the extended hypothesis, we replace the central point source with an extended source that has the same spectral parameterization. We then perform a simultaneous fit of the position, angular size, and spectral parameters (normalization and shape) of the central source. In this fit, we free the normalization and spectral shape parameters of sources within 1°.0 of the central source and normalizations of sources within 1°.5 of the central source.

For the halo hypothesis, we add a new extended source component with position fixed to that of the central source with a PL spectral parameterization with index Γ_{halo} that is independent of the central source. The normalization, index, and angular size of the halo component are left as free parameters. The normalization of the central source and all sources within 1°.0 of the central source are freed. We parameterize the angular size of the extended component with the intrinsic 68% containment radius, which we denote with R_{ext} and R_{halo} for the case of the extended and halo model, respectively.

To distinguish an extended source from a cluster of point sources, we compare models using the Akaike information criterion (AIC, Akaike 1974) given by AIC $= 2k - 2\ln\mathcal{L}$, where k is the number of parameters in the model. The formulation of the AIC penalizes models with a larger number of parameters, and hence minimizes overfitting. The best model will minimize the AIC. Models with fewer parameters are preferred unless a model with more parameters provides a substantially better fit. We define Δ_m as the difference between the AIC of the models with and without extension,

$$\begin{aligned}\Delta_m &= \mathrm{AIC}_{n+m} - \mathrm{AIC}_{n+1} \\ &= 2(\ln\mathcal{L}_{n+1} - \ln\mathcal{L}_{n+m} + \nu_{n+\mathrm{m}} - \nu_{n+1}),\end{aligned} \quad (1)$$

where $m =$ ext (halo) for the extension (halo) hypothesis, $\mathcal{L}_{n+1}$ is the likelihood for the model with $n+1$ point sources, $\mathcal{L}_{n+m}$ is the likelihood for the model with extended emission, and ν_X is the number of degrees of freedom of the given model. If $\Delta_m > 0$, then a model with an additional point source is preferred over a model with extension.

In cases where a bright extended source is superimposed on a fainter point source, the criterion defined in Equation (1) will tend to prefer the extended source model with n point sources even when a model with extension and $n+1$ point sources gives a better fit to the data (smaller AIC). To distinguish this scenario, we define TS_{m+1} as twice the difference in the log-likelihood of extended source models with n and $n+1$ point sources,

$$\mathrm{TS}_{m+1} = 2(\ln\mathcal{L}_{n+m+1} - \ln\mathcal{L}_{n+m}), \quad (2)$$

where $\mathcal{L}_{n+m+1}$ is the likelihood for the extended source model with $n+1$ point sources. If no additional point sources are

found in the subsequent iteration, then Δ_m and TS_{m+1} are undefined.

For the extension and halo hypotheses, we select a best-fit model of the inner ROI with n point sources, where n is the first iteration for which $\Delta_m < 0$ and $\mathrm{TS}_{m+1} < 16$, or for which no additional point sources are found (at a level of 3σ). Given the best-fit iteration n, the evidence for extended emission is evaluated from the likelihood ratio between models with and without an extended component,

$$\mathrm{TS}_m = 2(\ln \mathcal{L}_{n+m} - \ln \mathcal{L}_n). \quad (3)$$

Because the hypotheses are nested, we expect the test statistics for the extension and halo hypotheses ($\mathrm{TS}_{\mathrm{ext}}$ and $\mathrm{TS}_{\mathrm{halo}}$ respectively) to be distributed as χ^2_ν, where ν is the difference in the number of degrees of freedom ($\nu = 1$ and 3 for the extension and halo hypotheses, respectively). We identify a source as extended if $\mathrm{TS}_{\mathrm{ext}} > 16$. Sources that exceed the threshold for extension are additionally fit with a 2D disk morphology, and the Gaussian or disk morphology is chosen on the basis of the model with the largest likelihood.

We find that some extended sources are composites of multiple 3FGL sources, which results in multiple analysis seeds being associated with the same source. Where the same extended source is detected in multiple analysis seeds (spatial overlap of the 68% containment circle greater than 50%), we merge the analysis seeds into a single seed with position equal to the average of the seed positions. We then perform a new analysis of the source using the merged analysis seed and drop the original analysis seeds from the catalog. Six of the extended FHES sources were found to be composites of two or more 3FGL sources. Merging these seeds resulted in the removal of 15 of the original analysis seeds.

If we detect a point source with $\mathrm{TS}_{\mathrm{halo}} > 16$, we create a new extended source and analyze the ROI with a model that includes both the point source and an extended component with the same morphological and spectral parameters as the best-fit halo. We then run the analysis pipeline on the extended component, refitting both its position and extension. We convert the candidate halo into a separate extended FHES source if it is detected with $\mathrm{TS} > 25$. Nine of the extended FHES sources are found by the search for extended halo emission.

2.3. Diffuse and IRF Systematics

The two primary sources of systematic error in our analysis are the instrument response functions (IRFs) and the Galactic interstellar emission model (IEM). We take the total systematic error from the larger of the errors induced by the IRFs and IEM. Due to the strong gradient in IEM intensity with Galactic latitude, IEM uncertainties are typically subdominant for sources with $|b| > 20^\circ$.

Our nominal Galactic IEM is the recommended one for `PASS8` source analysis, which we denote as IEM-STD. IEM-STD is based on the IEM developed with `P7REP` data (Acero et al. 2016a). IEM-STD has the same spatial distribution as the `P7REP` model, but has been rescaled with a small, energy-dependent correction to account for the difference in the influence of energy dispersion in the `P7REP` and `PASS8` data sets. To quantify the impact of diffuse systematics, we repeat our analysis with nine alternative IEMs: the eight models from Acero et al. (2016b) (IEM-A0 to IEM-A7) and the IEM developed for the study of diffuse emission in the inner Galaxy (IEM-B Ackermann et al. 2017b). Because the models from Acero et al. (2016b) were developed with `P7REP` data, we apply the same energy dispersion correction that was used for IEM-STD to obtain models appropriate for `PASS8` analysis.

To evaluate the IEM-induced systematic uncertainty on a fitted quantity P, we follow the method of Acero et al. (2016b) by calculating the dispersion between the nominal value obtained with IEM-STD and the value obtained with the nine alternative IEMs,

$$\delta P_{\mathrm{sys}} = \sqrt{\frac{1}{\sum_i \sigma_i^{-2}} \sum_i \sigma_i^{-2} (P_{\mathrm{STD}} - P_i)^2} \quad (4)$$

where P_{STD} is the measured value obtained with IEM-STD, and P_i and σ_i are the values and statistical uncertainties for P obtained with the nine alternative IEMs.

The primary instrumental uncertainty relevant for studies of extension is the PSF. To evaluate the systematic uncertainty on the PSF, we consider two bracketing PSF models based on the recommended systematic error band for the PSF 68% containment radius.[66] We define the following piecewise scaling function for the relative PSF uncertainty versus energy:

$$f(E) = \begin{cases} 0.05 & E \leqslant 10\ \mathrm{GeV} \\ 0.05 + 0.1 \times \log_{10}(E/10\ \mathrm{GeV}) & E > 10\ \mathrm{GeV} \end{cases}. \quad (5)$$

This function defines a constant 5% error below 10 GeV that rises to 25% at 1 TeV. We note that the increase in the systematic uncertainty above 10 GeV is driven by the statistical precision of the in-flight validation sample, rather than an observed discrepancy in the model of the PSF. We construct bracketing models of the PSF versus reconstruction angle and energy, $P_{\mathrm{min}}(\theta; E)$ and $P_{\mathrm{max}}(\theta; E)$, by scaling the average PSF, $P(\theta; E)$, with this function such that $P_{\mathrm{min}}(\theta; E) = P(\theta \times (1 + f(E)); E)(1 + f(E))^2$ and $P_{\mathrm{max}}(\theta; E) = P(\theta \times (1 + f(E))^{-1}; E)(1 + f(E))^{-2}$. Applying this model to sources detected with $\mathrm{TS}_{\mathrm{ext}} > 9$, we find a median systematic error on the 68% containment radius of $0^\circ.005$. With the exception of the brightest LAT sources, the systematic error is much smaller than the statistical error.

2.4. Source Associations

Because our seeds are taken from the 3FGL and 3FHL, we expect the majority of the FHES sources to have a direct counterpart with a source from at least one of these two catalogs. Rather than performing an independent search for associations, we assign associations by taking the association of the closest 3FGL or 3FHL counterpart. Positional uncertainties of both FHES point sources and extended sources are evaluated by fitting a paraboloid to log-likelihood values sampled on a grid centered on the best-fit position. The resulting positional error ellipse is parameterized by 68% uncertainties along the semiminor and semimajor ellipse axes and a position angle.

For the FHES sources that are best-fit by a point source morphology, we identify the γ-ray counterpart by finding the nearest 3FGL or 3FHL point source with angular separation

[66] https://fermi.gsfc.nasa.gov/ssc/data/analysis/LAT_caveats.html

$<1.5 \times \sqrt{\theta_{95,\mathrm{FHES}}^2 + \theta_{95,X}^2}$, where $\theta_{95,\mathrm{FHES}}$ and $\theta_{95,\mathrm{X}}$ are the symmetric 95% positional uncertainties of the FHES source and 3FGL or 3FHL source, respectively. Our association threshold, which is more inclusive than that used in previous LAT catalogs, is chosen to achieve a false negative rate $\lesssim$0.1%. The more inclusive association threshold is motivated by the fact that the data sets used for the FHES and the 3FGL are largely independent due to the difference in exposure and the transition from P7REP to PASS8. Where we find both a 3FGL and a 3FHL counterpart, we take the source association and classification from the 3FGL.

For sources that have blazar associations, we take the blazar characteristics (redshift, optical class, synchrotron peak frequency) from the 3LAC (Ackermann et al. 2015) or 3FHL for sources with a 3FGL or 3FHL association, respectively.

Associations for the FHES extended sources are performed on a case-by-case basis by examining positional and morphological correlations with multiwavelength counterparts. In several cases, we find that an extended source may be a composite of 3FGL sources. We identify a 3FGL or 3FHL source as a composite counterpart if it is encompassed within the intrinsic radius of the extended source and has no point-source counterpart in the best-fit model of the ROI. The associations and 3FGL counterparts for FHES extended sources are discussed further in Section 3.2.

2.5. Flux and Extension Likelihood Profiles

After obtaining the best-fit model for each source, we extract likelihood profiles that we use for the analysis of stacked samples (Section 4.4) and modeling of pair cascades (Section 5). The likelihood profiles are evaluated on a regular grid of parameter values $\boldsymbol{x}_i$ by maximizing the likelihood with respect to a set of nuisance parameters ($\boldsymbol{\theta}$) at each point in the coordinate grid. The nuisance parameters that maximize the likelihood at each grid point are denoted with $\hat{\boldsymbol{\theta}}$. The tabulated profile likelihood values are included in the LIKELIHOOD table of the FITS catalog file (see Appendix B). The likelihood profiles extracted for each source are:

1. $\mathcal{L}_{\mathrm{ext}}(R_{\mathrm{ext}}; \hat{\boldsymbol{\theta}})$: Likelihood versus angular extension (R_{ext}) of the source of interest (ext_dloglike column in the LIKELIHOOD Table). The scan in angular extension is performed on a logarithmic grid between 0.°00316 and 1.°77.
2. $\mathcal{L}_{\mathrm{halo}}(F_{\mathrm{halo}}, R_{\mathrm{halo}}, \Gamma_{\mathrm{halo}}; \hat{\boldsymbol{\theta}})$: Likelihood for a halo component with a 2D Gaussian morphology and a PL spectrum parameterized by flux (F_{halo}), extension (R_{halo}), and spectral index (Γ_{halo}). The likelihood is evaluated on a logarithmic grid in R_{halo} with 15 steps between 0.°0316 and 1.°77, a logarithmic grid in F_{halo} with 60 steps between 10^{-10} MeV cm^{-2} s^{-1} and 10^{-4} MeV cm^{-2} s^{-1}, and a grid in Γ_{halo} between 1 and 4 in steps of 0.25. (halo_dloglike column in the LIKELIHOOD Table)
3. $\mathcal{L}_{\mathrm{halo},i}(F_{\mathrm{halo}}, R_{\mathrm{halo}}; \hat{\boldsymbol{\theta}})$: Likelihood for a halo component with flux (F_{halo}) and extension (R_{halo}) in energy bin i (halo_sed_dloglike column in the LIKELIHOOD Table). The likelihood is evaluated on a logarithmic grid in R_{halo} with 15 steps between 0.°0316 and 1.°77. Likelihood evaluation points in F_{halo} are chosen individually for a given R_{halo} and energy bin i to sample points around the peak of the likelihood function.
4. $\mathcal{L}_{\mathrm{src},i}(F; \hat{\boldsymbol{\theta}})$: Likelihood versus source flux in energy bin i (src_sed_dloglike column in the LIKELIHOOD Table). Likelihood evaluation points in F are chosen individually for a given energy bin to sample points around the peak of the likelihood function.

For all likelihood profiles, the nuisance parameters include the normalizations of both diffuse components and all sources in the inner ROI. In the case of the likelihood versus extension, we also simultaneously fit the normalization and spectral shape parameters of the source of interest. Following the approach developed for DM analyses of the SMC and LMC (Buckley et al. 2015; Caputo et al. 2016), when evaluating the likelihood profiles versus flux in a given energy bin i ($\mathcal{L}_{\mathrm{halo},i}(F_{\mathrm{halo}}, R_{\mathrm{halo}}; \hat{\boldsymbol{\theta}})$ and $\mathcal{L}_{\mathrm{src},i}(F; \hat{\boldsymbol{\theta}})$), we fit the nuisance parameters while applying a prior on their values derived from the broadband (full energy range) fit. The profile likelihood is given by

$$\mathcal{L}_i(\boldsymbol{x}; \hat{\boldsymbol{\theta}}_i) = \max_{\boldsymbol{\theta}} \mathcal{L}_i(\boldsymbol{x}; \boldsymbol{\theta}) \prod_j N(\theta_j - \tilde{\theta}_j, 5\sigma_j), \quad (6)$$

where $\boldsymbol{x}$ represents the parameters of interest, N is the normal distribution, $\tilde{\theta}_j$ and σ_j are the value and uncertainty on θ_j obtained from the broadband fit. This prior constrains the amplitude of each nuisance parameter to lie within 5σ of its value from the broadband fit.

3. Extension Catalog

As described in Section 2, this analysis searches for source extension using 3FGL and 3FHL point sources as targets. There are 55 known extended sources in these catalogs, which include the most current compilation of spatially extended LAT sources.[67] Most of these sources are Galactic SNRs and PWNe and are well within the Galactic plane ($|b| < 5°$). At higher latitudes, extended sources are generally galaxies: for example, the Magellanic Clouds, the lobes of Centaurus A, and Fornax A.

From our analysis of 2689 seed positions, we identify 24 extended sources and 2520 sources consistent with a point-like morphology. The extended source list includes 23 with statistically significant extension ($\mathrm{TS}_{\mathrm{ext}} \geqslant 16$), as well as M31, which falls slightly below our detection threshold ($\mathrm{TS}_{\mathrm{ext}} = 15.5$). M31 was previously detected as extended (Ackermann et al. 2017a) and the measured extension from that work is in good agreement with this analysis.

Using the procedure outlined in Section 2.4, we find a γ-ray association for all but 70 of the 2520 FHES point sources. From the 220 seeds that are initialized with a 3FHL source, only five sources are not detected in our analysis or do not have a 3FHL association (note that, if there is a 3FGL counterpart for a 3FHL source, we use the 3FGL source position). The unassociated sources have integrated fluxes between 4.3×10^{-11} cm^{-2} s^{-1} and 1.1×10^{-9} cm^{-2} s^{-1}, with a median 2.5×10^{-10} cm^{-2} s^{-1}, which is a factor of $\sim$2 lower than the median of the full catalog (4.7×10^{-10} cm^{-2} s^{-1}). Table 2 summarizes the number of sources with a 3FGL or 3FHL association. FHES point sources without a 3FGL or 3FHL association are excluded from the search for angular extension and are not included in the available FHES data products.

[67] https://fermi.gsfc.nasa.gov/ssc/data/access/lat/3FHL/

Table 2
Summary of Analysis Seeds and FHES Sources

Category	Number
Analysis Seeds	
3FGL	2469
3FHL	220
Total	2689
Point Sources	
3FGL Association	1112
3FHL Association	218
3FGL and 3FHL Association	1120
Unassociated[a]	70
Total	2520
Extended Sources	
Known	5
Associated	5
Unassociated	6
Confused	8
Total	24

Note. Number of unassociated extended sources excludes sources classified as confused.
[a] FHES point sources without a 3FGL or 3FHL association are excluded from further analysis.

A summary of the results of the spatial analyses for the extended sources is shown in Table 3. In Table 4, we show the measured properties of these sources (position, size, flux, and spectral index) along with their statistical errors and systematic errors obtained from the nine alternative IEMs and the two bracketing PSF models. Of the 24 extended sources reported in this work, 19 are newly detected. Nine of the newly detected sources were found via the halo test (indicated with a dagger in Tables 3 and 4) and do not have a direct counterpart in the 3FGL or 3FHL. The characteristics of the five previously detected extended sources obtained in this study are in agreement with those found in previous publications (references are provided in Section 3.1). Five of the new sources have potential associations, and the remaining are classified as unassociated. We have separated the unassociated sources into two categories, based on the spectral index of their PL spectrum: $\Gamma < 2.3$ (hard) and $\Gamma > 2.3$ (soft) for the 2D Gaussian extension. The distinction between hard and soft sources is made because the soft sources might resemble a mismodeling of the Galactic diffuse emission, which also has a soft spectrum.

We identify 8 of the 19 newly identified extended sources as "confused," indicating sources that may be spurious, that could be affected by systematic uncertainties in the IEM, or that are seen in the direction of H II regions. The ionized gas is not accounted for in the current IEM, although it can significantly contribute to the diffuse γ-ray emission in the case of massive H II regions (Remy et al. 2017). These sources are grouped into a separate section at the bottom of Tables 3 and 4. We categorize a source as confused if TS_{ext} falls below our detection threshold when analyzed with at least one of the alternative IEMs, or if the fractional systematic uncertainty on the source flux exceeds 50%. We also categorize FHES J0430.5+3525 as confused based on a separate analysis with an IEM based on *Planck* dust maps (Abergel et al. 2014). Finally, we characterize FHES J0000.2+6826 as confused after our inspection of the velocity-integrated map of H_α emission from the Wisconsin H-Alpha Mapper (WHAM) Sky Survey. All but one of the confused sources are unassociated, and four of them (FHES J0000.2+6826, FHES J0242.5+5229, FHES J0430.5+3525, and FHES J0940.6−6128) have soft spectral indices similar to that expected from Galactic diffuse emission.

The format of the extended source catalog follows the previous *Fermi*-LAT catalogs. A FITS file with analysis results for all 2520 point sources and 24 extended sources is available in multiple locations.[68] The format of the catalog file is described in Appendix B.

Figure 2 shows the distribution of FHES sources in Galactic coordinates. We note that all of the new extended sources are found at low latitudes ($4° \lesssim |b| \lesssim 20°$),[69] implying potential Galactic origin. We found the sources were generally associated with either SNRs or SFRs, the two exceptions being the ρ Oph Cloud, which was originally discovered by *COS B* at γ-ray energies (Mayer-Hasselwander et al. 1980) and was previously found as an extended object in γ-rays (Lande et al. 2012; Abrahams et al. 2017), and the Crab Nebula, which did not pass the extension criteria threshold in Ackermann et al. (2017c). Figure 3 shows the detected extension and extension upper limits for all the sources investigated in this analysis. We see that the extension upper limit is generally correlated with the flux. The outlier with the small extension and high flux is the Crab Nebula.

3.1. Known Extended Sources

The five sources in our analysis that are 3FGL point sources but have already observed extensions are:

1. FHES J0322.2−3710: Fornax A (Ackermann et al. 2016b),
2. FHES J0043.1+4112: M31 (Ackermann et al. 2017a),
3. FHES J1626.9−2431: ρ Oph cloud (Lande et al. 2012; Abrahams et al. 2017),
4. FHES J0426.4+5529: SNR G150.3+04.5 (Acero et al. 2016b; Ackermann et al. 2016a),
5. FHES J1208.7−5229: SNR G295.5+09.7 (Acero et al. 2016b).

These sources are included in Table 3 and their spectral and spatial properties are in agreement with the published results.

3.2. Individual Sources of Interest

Previously unidentified extended sources are discussed in further detail in Sections 3.2.1–3.2.7. These extended objects often encompass multiple 3FGL sources. We performed searches in archival radio, infrared, optical, UV, and X-ray data to look for potential associations. These surveys were accessed using SkyView.[70] Data include the IR band from the Digital Sky Survey (DSS and DSS2); both the Low Frequency Instrument (LFI) on the *Planck* satellite at 30 GHz, 44 GHz, and 70 GHz, and the High Frequency Instrument (HFI) at 353 GHz; the *K* and K_a frequencies (23 and 33 GHz respectively) on the *Wilkinson Microwave Anisotropy Probe* (*WMAP*); the

[68] http://www-glast.stanford.edu/pub_data/1261/ and https://zenodo.org/record/1324474.
[69] We find three source at latitudes $|b|$ slightly below our cut value of 5°. The reason is that we consider seed positions $|b| > 5°$, but our ROIs have sizes $6° \times 6°$. Thus, the FHES source positions can have latitudes as low as $|b| = 2°$.
[70] https://skyview.gsfc.nasa.gov

Table 3
FHES Extended Sources

Name	l (°)	b (°)	Association	Class	TS	Model	TS_{ext}	R_{ext}(°)
FHES J0006.7+7314[b]	119.67	10.65	SNR G119.5+10.2	snr	38.0	D	37.3 (37.3)	0.98 ± 0.05 ± 0.04
FHES J0043.2+4109[a]	121.27	−21.68	M31	gal	72.9	G	15.5 (13.2)	0.52 ± 0.12 ± 0.02
FHES J0322.2−3710[a]	240.12	−56.78	Fornax A	rdg	70.5	G	25.7 (24.6)	0.342 ± 0.051 ± 0.007
FHES J0426.4+5529[a]	150.21	4.45	SNR G150.3+04.5	snr	377.2	G	366.2 (255.6)	1.41 ± 0.06 ± 0.05
FHES J0534.5+2201	184.55	−5.78	Crab Nebula	PWN	7879.4	G	42.7 (11.7)	0.030 ± 0.003 ± 0.007
FHES J1208.7−5229[a]	296.36	9.84	SNR G295.5+09.7	snr	84.6	D	76.9 (70.9)	0.70 ± 0.03 ± 0.02
FHES J1325.3−3946[b]	309.99	22.63	Cen A Lobes	rdg	38.9	D	35.5 (35.5)	1.46 ± 0.06 ± 0.27
FHES J1332.6−4130	311.17	20.70	Cen A Lobes	rdg	56.6	D	30.0 (30.0)	0.62 ± 0.04 ± 0.10
FHES J1501.0−6310[b]	316.95	−3.89			148.4	G	95.9 (35.7)	1.29 ± 0.13 ± 0.25
FHES J1626.9−2431[a]	353.06	16.73	ρ Oph Cloud	mc	411.7	G	79.9 (77.6)	0.29 ± 0.03 ± 0.01
FHES J1642.1−5428	332.48	−5.43	SNR G332.5−05.6	snr	45.2	D	26.4 (21.8)	0.57 ± 0.02 ± 0.05
FHES J1723.5−0501	17.90	16.96			89.5	G	52.9 (47.4)	0.73 ± 0.10 ± 0.01
FHES J1741.6−3917[b]	350.73	−4.72			189.1	D	188.2 (137.2)	1.35 ± 0.03 ± 0.29
FHES J2129.9+5833	99.13	5.33			87.7	G	49.4 (42.6)	1.09 ± 0.13 ± 0.03
FHES J2208.4+6443	106.62	7.15			136.1	G	65.2 (37.0)	0.93 ± 0.11 ± 0.11
FHES J2304.0+5406[b]	107.50	−5.52			46.1	G	43.3 (34.1)	1.58 ± 0.35 ± 0.17
				Confused Sources				
FHES J0000.2+6826	118.24	6.05	NGC 7822	sfr	194.7	D	149.7 (113.5)	0.98 ± 0.04 ± 0.01
FHES J0242.5+5229[b]	139.54	−6.76			95.0	G	26.9 (26.9)	0.84 ± 0.18 ± 0.32
FHES J0430.5+3525[c]	165.28	−8.86			153.6	G	100.1 (100.1)	1.11 ± 0.10 ± 0.09
FHES J0631.5−0940	219.36	−8.79			42.3	D	19.7 (12.7)	0.86 ± 0.04 ± 0.08
FHES J0737.3−3205[b]	246.44	−5.30			63.6	D	61.1 (61.1)	0.69 ± 0.03 ± 0.36
FHES J0940.6−6128[b]	282.10	−6.58			56.8	D	54.2 (8.2)	1.97 ± 0.08 ± 0.56
FHES J1232.9−7105[c]	301.42	−8.28			58.6	D	25.8 (0.0)	0.62 ± 0.03 ± 0.31
FHES J1743.7−1609[b]	10.72	7.01			33.8	G	30.5 (15.6)	1.02 ± 0.22 ± 0.37

Note. The TS column gives the test statistic for detection (likelihood ratio of models with and without the source). The TS_{ext} column gives the value of TS_{ext} obtained under the primary analysis, and in parentheses, the smallest value obtained under the bracketing PSF models or alternative IEMs. The class column gives the class designator (snr—Supernova Remnant, rdg—Radio Galaxy, pwn—Pulsar Wind Nebula, mc—Molecular Cloud, sfr—Star-forming Region, gal—Galaxy). The model column indicates the best-fit spatial model for each source (G—Gaussian, D—Disk). Here, R_{ext} is the 68% containment radius of the best-fit spatial model (for the disk model $R_{ext} = 0.82R$ where R is the disk radius). The first and second errors on R_{ext} are statistical and systematic, respectively.
[a] Detected as extended in previous publication.
[b] Detected via halo test (no 3FGL or 3FHL counterpart).
[c] Identified as spurious in previous publication.

Sydney University Molonglo Sky Survey (SUMMS) at a frequency of 843 MHz; and finally, the Westerbork Northern Sky Survey (WENSS) at a frequency of 325 MHz. We looked for potential associations to known sources in the TeV energy band with TeVCat.[71]

For sources that we suspect to be associated with cosmic-ray interactions with the Interstellar Medium (ISM), we perform comparisons with maps of dust optical depth at 353 GHz (τ_{353}) from *Planck* Public Data Release 1 (Abergel et al. 2014). Thermal dust emission has been shown to be correlated with components of the ISM, and the *Planck* τ_{353} map provides much better information than the ISM tracers used for the official *Fermi* IEM (Acero et al. 2016a).

In this search for counterparts of the 19 sources previously not known to be extended, we found five sources with potential associations: two sources in regions of SNRs that were previously undetected by the LAT (Sections 3.2.1 and 3.2.2); two sources near the Cen A Lobes, which extend beyond the current model based on *WMAP* data (Section 3.2.3); and one in the direction of the Crab Nebula (Section 3.2.4), which is the only source with an extension comparable to the systematic uncertainty on the IRFs. Three of the more tentative associations are found in SFRs, and are discussed in Section 3.2.5.

[71] http://tevcat.uchicago.edu/

Three unassociated extended sources have a spectral and spatial morphology that is consistent with SNRs or PWNe. These are further discussed in Section 3.2.6. The sources with soft spectra consistent with the Galactic diffuse emission are discussed in Section 3.2.7. With the exception of the possible SFR source FHES J0430.5+3525, sources identified as confused are not discussed further.

3.2.1. CTA 1: SNR G119.5+10.2 (FHES J0006.7+7314)

The SNR CTA 1 is located about 1400 pc away in the constellation of Cepheus, and has an estimated age of 1.3×10^4 years (Slane et al. 2004). The pulsar, PSR J0007+7303, located within the SNR CTA 1, is the first γ-ray only pulsar discovered with the *Fermi*-LAT (Abdo et al. 2008). The associated PWN has been detected at very-high γ-ray energies with VERITAS (Aliu et al. 2013). In the first two years of LAT observations, extended emission that could have been related to the PWN was detected at the $\sim 2\sigma$ level. A subsequent LAT analysis of PSR J0007+7303 with over seven years of `Pass 8` data found no evidence for extended γ-ray emission over the 0.°3 region encompassing the TeV source VER J0006+729 (Li et al. 2016).

We perform this analysis in the off-pulse of the pulsar γ-ray emission using an eight-year γ-ray ephemeris and the phase interval $\phi \in [0.55, 1.05]$. We include a point-source component at the location of PSR J0007+7303 (TS = 153) to

Table 4
Measured Properties of FHES Extended Sources with their Statistical and Systematic Errors

Name	l (°)	b (°)	$\delta\theta_{\rm stat}$(°)	$\delta\theta_{\rm sys}$(°)	$R_{\rm ext}$(°)	Index	Flux (1 GeV–1 TeV) [$\times 10^{-10}$ cm^{-2} s^{-1}]
FHES J0006.7+7314[b]	119.67	10.65	0.13	0.18	0.98 ± 0.05 ± 0.04	2.24 ± 0.16 ± 0.02	18.0 ± 3.5 ± 3.4
FHES J0043.2+4109[a]	121.27	−21.68	0.12	0.03	0.52 ± 0.12 ± 0.02	2.66 ± 0.21 ± 0.01	7.6 ± 1.0 ± 0.3
FHES J0322.2−3710[a]	240.117	−56.784	0.078	0.003	0.342 ± 0.051 ± 0.007	2.16 ± 0.13 ± 0.00	5.9 ± 1.0 ± 0.1
FHES J0426.4+5529[a]	150.21	4.45	0.10	0.25	1.41 ± 0.06 ± 0.05	1.81 ± 0.04 ± 0.12	56.7 ± 4.3 ± 21.1
FHES J0534.5+2201	184.552	−5.781	0.002	0.000	0.030 ± 0.003 ± 0.007	1.79 ± 0.04 ± 0.00	412.3 ± 8.7 ± 1.4
FHES J1208.7−5229[a]	296.36	9.84	0.06	0.06	0.70 ± 0.03 ± 0.02	1.81 ± 0.09 ± 0.05	9.6 ± 1.6 ± 1.3
FHES J1325.3−3946[b]	309.99	22.63	0.16	0.67	1.46 ± 0.06 ± 0.27	2.22 ± 0.14 ± 0.08	17.7 ± 3.0 ± 6.5
FHES J1332.6−4130	311.17	20.70	0.10	0.10	0.62 ± 0.04 ± 0.10	2.08 ± 0.12 ± 0.04	8.6 ± 1.3 ± 2.5
FHES J1501.0−6310[b]	316.95	−3.89	0.15	0.33	1.29 ± 0.13 ± 0.25	2.44 ± 0.09 ± 0.07	60.7 ± 5.2 ± 10.6
FHES J1626.9−2431[a]	353.06	16.73	0.03	0.05	0.29 ± 0.03 ± 0.01	2.55 ± 0.07 ± 0.03	43.4 ± 2.6 ± 4.9
FHES J1642.1−5428	332.48	−5.43	0.06	0.10	0.57 ± 0.02 ± 0.05	1.78 ± 0.12 ± 0.08	7.0 ± 1.9 ± 2.3
FHES J1723.5−0501	17.90	16.96	0.13	0.15	0.73 ± 0.10 ± 0.01	1.97 ± 0.08 ± 0.06	18.3 ± 2.5 ± 2.1
FHES J1741.6−3917[b]	350.73	−4.72	0.07	0.26	1.35 ± 0.03 ± 0.29	1.80 ± 0.04 ± 0.06	47.5 ± 4.6 ± 17.3
FHES J2129.9+5833	99.13	5.33	0.15	0.43	1.09 ± 0.13 ± 0.03	2.30 ± 0.12 ± 0.04	31.1 ± 3.8 ± 2.3
FHES J2208.4+6443	106.62	7.15	0.12	0.13	0.93 ± 0.11 ± 0.11	2.78 ± 0.14 ± 0.15	32.4 ± 2.9 ± 9.9
FHES J2304.0+5406[b]	107.50	−5.52	0.29	0.12	1.58 ± 0.35 ± 0.17	1.95 ± 0.08 ± 0.15	21.6 ± 3.7 ± 7.8
Confused Sources							
FHES J0000.2+6826	118.24	6.05	0.09	0.22	0.98 ± 0.04 ± 0.01	2.72 ± 0.11 ± 0.07	41.5 ± 3.1 ± 3.4
FHES J0242.5+5229[b]	139.54	−6.76	0.14	0.20	0.84 ± 0.18 ± 0.32	2.59 ± 0.17 ± 0.29	19.8 ± 2.2 ± 20.9
FHES J0430.5+3525[c]	165.28	−8.86	0.13	0.12	1.11 ± 0.10 ± 0.09	2.59 ± 0.11 ± 0.05	40.5 ± 3.4 ± 4.3
FHES J0631.5−0940	219.36	−8.79	0.11	0.57	0.86 ± 0.04 ± 0.08	2.21 ± 0.12 ± 0.10	15.5 ± 2.6 ± 1.4
FHES J0737.3−3205[b]	246.44	−5.30	0.07	0.03	0.69 ± 0.03 ± 0.36	1.85 ± 0.08 ± 0.07	11.6 ± 2.1 ± 3.6
FHES J0940.6−6128[b]	282.10	−6.58	0.15	1.07	1.97 ± 0.08 ± 0.56	2.45 ± 0.11 ± 0.35	40.9 ± 5.5 ± 28.0
FHES J1232.9−7105[c]	301.42	−8.28	0.09	0.74	0.62 ± 0.03 ± 0.31	2.31 ± 0.14 ± 0.57	11.1 ± 1.6 ± 10.4
FHES J1743.7−1609[b]	10.72	7.01	0.24	0.32	1.02 ± 0.22 ± 0.37	2.07 ± 0.11 ± 0.13	19.8 ± 3.8 ± 24.4

Notes. Here, $\delta\theta_{\rm stat}$ and $\delta\theta_{\rm sys}$ are the statistical and systematic 68% positional uncertainties. The first and second errors on $R_{\rm ext}$, Index, and Flux are statistical and systematic. The systematic error is the larger of the IRF and IEM systematics. No systematic errors are given for the Crab Nebula position because no measurable change in the best-fit position was observed for either the bracketing PSF models or alternative IEMs. We define $R_{\rm ext}$ as the 68% containment radius of the best-fit spatial model (for the disk model $R_{\rm ext} = 0.82R$ where R is the disk radius). The Index column gives the spectral index for sources parameterized with a PL spectrum and the spectral slope at 1 GeV for sources parameterized with an LP or PLE spectrum.
[a] Detected as extended in previous publication.
[b] Detected via halo test (no 3FGL or 3FHL counterpart).
[c] Identified as spurious in previous publication.

model the off-peak emission from the pulsar. The best-fit model also includes a new point source to the west of the PSR location. Li et al. (2016) identified this object as a variable source and found a probable association with the quasar S5 0016+73.

We find evidence for an extended γ-ray source FHES J0006.7+7314 that is correlated with the radio emission at 1420 MHz (Pineault et al. 1997), which is evident from the TS map (Figure 4, left), where the source is shown overlaid with the radio emission contours from the CTA 1 SNR. The map is generated with the central source from the ROI removed and a point source added instead at each pixel (modeled using a power law with index $\Gamma = 2$). The extension is fit best by a disk with $R_{\rm ext} = 0.^\circ98 \pm 0.^\circ05 \pm 0.^\circ04$. The γ-ray emission is somewhat larger in angular extent than the radio shell ($D \sim 1.^\circ5$), with a suggestion of elongation beyond the northern edge of the shell. The TeV γ-ray emission is located farther north, inside the incomplete radio shell, and is also shown in the figure. There is an obvious difference in angular size between the TeV and GeV γ-ray emission. A morphology similar to the GeV emission is seen in *ROSAT* PSPC X-ray images of the region (Seward et al. 1995; Slane et al. 1997). In the right panel of Figure 4, we compare the *Fermi*-LAT spectrum of FHES J0006.7+7314 to the one of the VERITAS source, VER J0006+729. There is evidence for mismatch in the flux normalization observed between the two spectra, even when taking into account the difference in angular size. This could indicate a spectral break at higher energies, or the observation of two separate sources. However, the spectral indices agree well with each other.

3.2.2. SNR G332.5−05.6 (FHES J1642.1−5428)

SNR G332.5-5.6, located in the constellation Norma, is between 7000–9000 years old and is ∼3.4 kpc away (Reynoso & Green 2007). It has been detected in radio and in X-ray wavelengths as an extended object by *XMM-Newton* (Suárez et al. 2015) and *Suzaku* (Zhu et al. 2015), as well as by *ATCA* and *ROSAT* (Reynoso & Green 2007). It was not detected in the first LAT SNR Catalog (Acero et al. 2016b); however, in the 3FGL (3FGL J1645.9−5420), it was classified as having a potential association with an SNR or PWN. X-ray observations show strong X-ray emission from the center of the remnant, which has morphology similar to that of the central radio emission. No radio, X-ray, or γ-ray pulsars have been found in the vicinity of SNR G332.5-5.6. Figure 5 shows the TS map of the extended γ-ray emission in the region. We find the disk radius of FHES J1642.1−5428 to be $0.^\circ57 \pm 0.^\circ02 \pm 0.^\circ05$, with a spectral index $\Gamma = 1.78 \pm 0.12 \pm 0.08$, making it one of the hardest sources in the catalog.

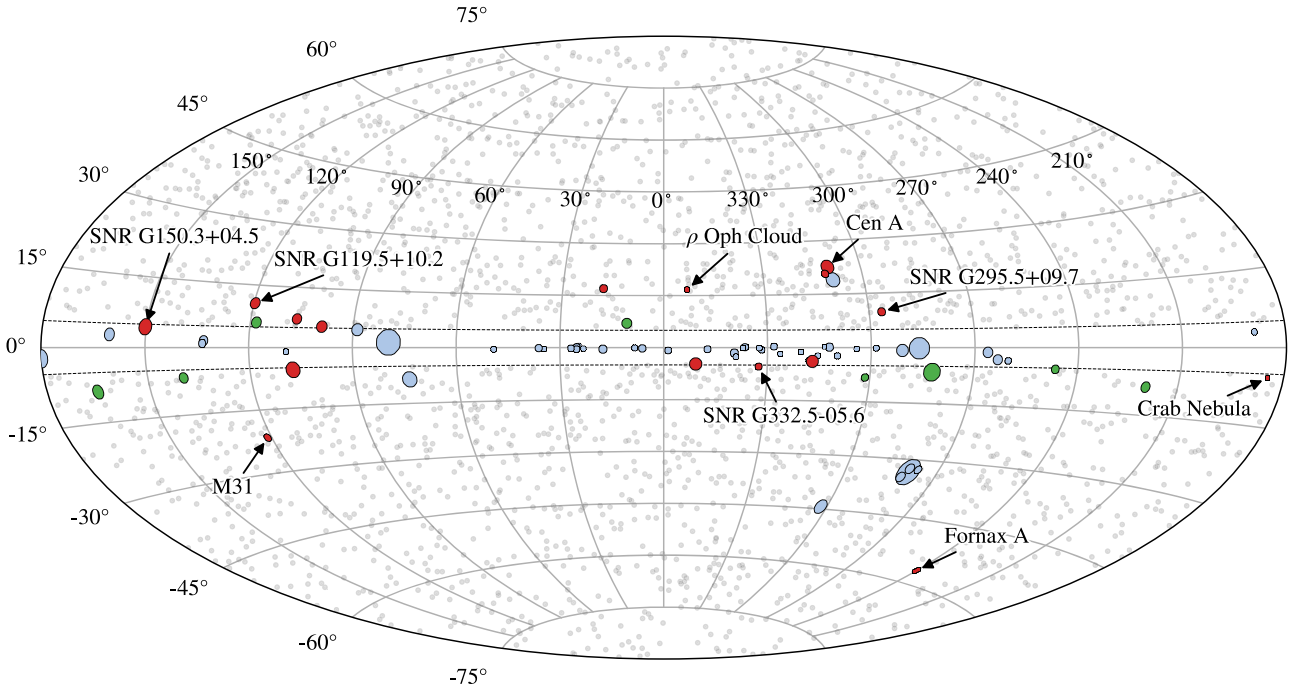

Figure 2. Distribution of FHES sources in Galactic coordinates. Light gray markers indicate FHES sources that are fit best by a point-source morphology. Red and green circles with black outlines indicate the 19 FHES sources that are fit best by an extended morphology. Green circles indicate the eight sources identified as confused based on the analysis with alternative IEMs. Two of the confused sources have already been identified as spurious in previous publications (Remy et al. 2017). The size of the marker is drawn to the scale of the intrinsic 68% containment radius of the source. Labeled sources are those with a previously published detection of extension or an association with a multiwavelength counterpart. Blue circles indicate the position and angular size of the 53 known LAT extended sources that fell outside our latitude selection or were explicitly excluded from the analysis. The dashed lines indicate the boundary of the latitude selection.

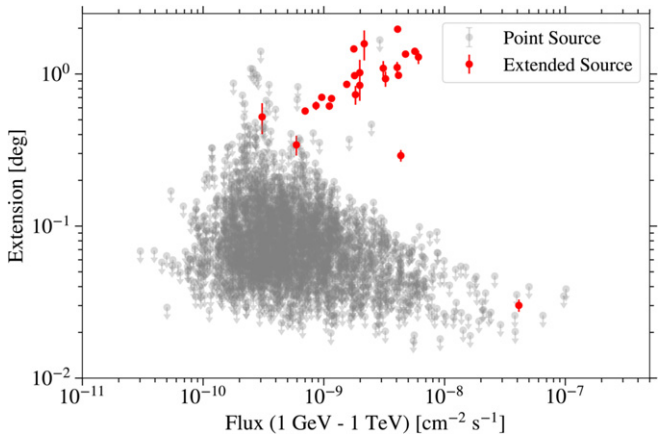

Figure 3. Extension vs. flux above 1 GeV for sources in the FHES catalog. Gray points show the 95% CL upper limit on the angular extension for point sources ($TS_{ext} < 16$). Red points show the best-fit value and 1σ errors on the extension (68% containment radius) for extended sources ($TS_{ext} > 16$).

3.2.3. Cen A Lobes (FHES J1325.3−3946 and FHES J1332.6−4130)

Cen A is one of the brightest radio sources in the sky. It was first identified as a γ-ray source by *COS B* (Swanenburg et al. 1981), and later by *OSSE* (Kinzer et al. 1995) and *EGRET* (Thompson et al. 1995). It was also one of the first γ-ray sources to be identified with a galaxy (NGC 5128) outside our Milky Way (Israel 1998). Extending from the bright central source is a pair of radio lobes with a total angular extent of $\sim 10^\circ$, which makes Cen A the largest non-thermal extragalactic radio source visible from the Earth. At a distance of 3.7 Mpc, it is also the closest radio-loud galaxy. The radio lobes are approximately 600 kpc across. Extended γ-ray emission, coming from the lobes as well as the radio core, has been detected at γ-ray energies with the LAT (Abdo et al. 2010b). Very high energy γ-ray emission has been observed with H.E.S.S., which is consistent only with the core and inner jets (Aharonian et al. 2009). The LAT γ-ray emission from the lobes is consistent with the morphology found with *WMAP* as well as the 30 GHz *Planck* data (Sun et al. 2016).

In addition to the γ-ray emission, which follows the 3FHL template of the lobes based on *WMAP*, there appear to be additional extended γ-ray components beyond the edge of the northern Cen A Lobe. Figure 6 shows a map of the Cen A region with the position and extension of the two FHES sources overlaid. We note that the analysis of these two sources was performed independently and the background models do not include the neighboring FHES extended source. However, the optimization procedure partially compensates for excess emission outside the search region via the inclusion of point-source components. Given that the best-fit disk models of these two sources partially overlap, it is likely that these two sources belong to a single diffuse emission component associated with Cen A.

Figure 7 shows the individual TS maps for the two sources with the two distinct regions around the north lobe: one directly north (FHES J1325.3−3946) and one west (FHES J1332.6−4130). We find the extension of the northern (western) source to be $1.^\circ 46 \pm 0.^\circ 06 \pm 0.^\circ 27$ ($0.^\circ 62 \pm 0.^\circ 04 \pm 0.^\circ 10$) and the spectral index to be $\Gamma = 2.22 \pm 0.14 \pm 0.08$ ($\Gamma = 2.08 \pm 0.12 \pm 0.04$). These sources, the western one in particular, are harder than both the north and south lobes, which have spectral indices of $\Gamma = 2.52^{+0.16}_{-0.19}$ and $\Gamma = 2.60^{+0.14}_{-0.15}$, respectively. The origin of this emission beyond the edge of the radio contours is unclear so far.

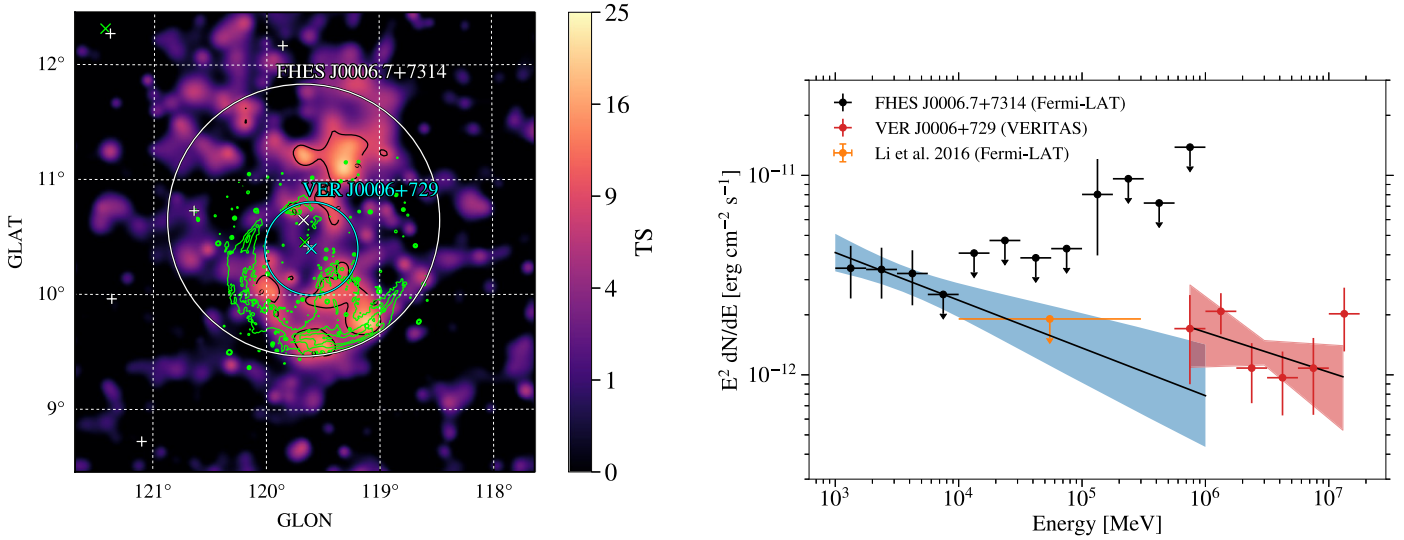

Figure 4. Left: TS map of FHES J0006.7+7314, which is associated with the CTA 1 SNR (SNR G119.5+10.2). The white circle with central marker × indicates the best-fit disk extension and centroid of the FHES source. White crosses indicate the positions of point-source candidates with TS > 9 from the best-fit model for the region. Green crosses indicate the positions of sources in the 3FGL catalog. Green contours show the map of radio continuum emission from the CTA 1 SNR measured at 1420 MHz (Pineault et al. 1997). The cyan circle and cross indicate the angular extent (68% containment) and centroid of the TeV source VER J0006 +729 (Aliu et al. 2013). Right: spectral energy distributions of FHES J0006.7+7314 from this analysis and the VERITAS spectrum of VER J0006+729. Upper limit points for FHES J0006.7+7314 are computed at 95% C.L. The orange marker shows the 99% upper limit from Li et al. (2016) on the energy flux between 10 GeV and 300 GeV measured within the 0.°3 angular extent of VER J0006+729.

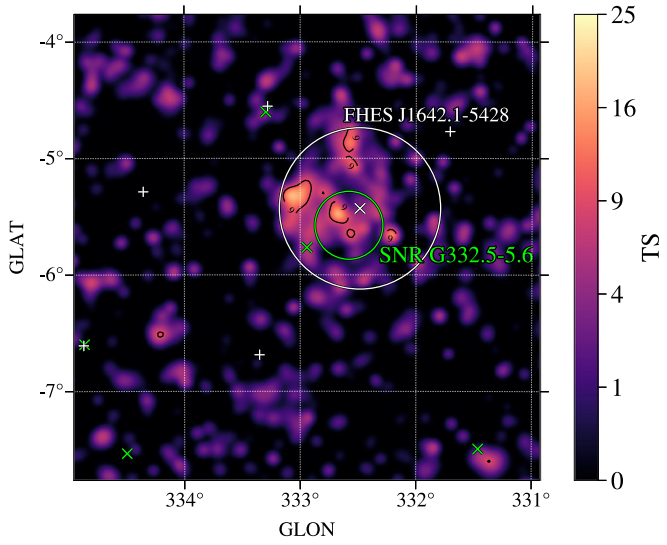

Figure 5. TS map of FHES J1642.1−5428, which is associated with SNR G332.5−05.6. The white circle with central marker × indicates the best-fit disk extension and centroid of the FHES source. White crosses indicate the positions of point-source candidates with TS > 9 from the best-fit model for the region. The green circle indicates the angular extent of the radio SNR from Reynoso & Green (2007). Green crosses indicate the positions of sources in the 3FGL catalog.

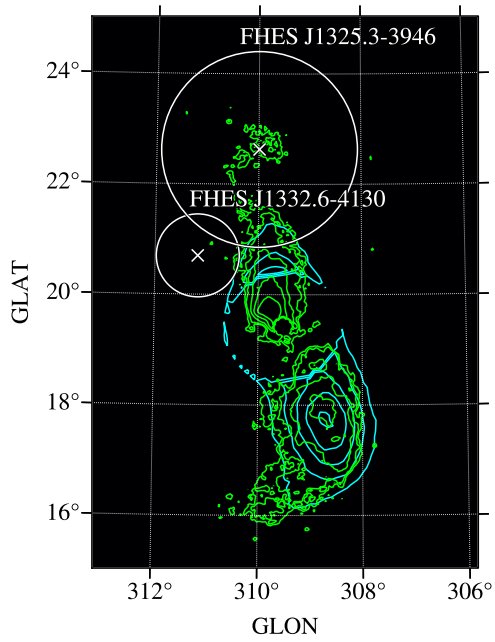

Figure 6. Map of the Cen A region, showing contours for the LAT γ-ray Cen A Lobes template (cyan) and Parkes radio continuum map at 5 GHz (green). The white circles with central marker × indicate the best-fit disk radius and centroid of the two FHES sources associated with Cen A: FHES J1325.3 −3946 and FHES J1332.6−4130.

3.2.4. Crab Nebula (FHES J0534.5+2201)

The Crab Nebula is a PWN associated with the young pulsar PSR J0534+2200, which is the compact remnant of a supernova explosion that occurred in the year 1054 AD, at a distance of ∼2 kpc (see, e.g., Hester 2008, for a review). In the 3FGL, the γ-ray emission from the Crab Nebula was decomposed into three components: an Inverse Compton component (IC; 3FGL J0534.5+2201i), a synchrotron component (3FGL J0534.5+2201s), and the Crab pulsar (3FGL J0534.5+2201). The point-like emission of the Crab Pulsar dominates the nebula at energies below 10 GeV, while the IC component dominates above 10 GeV. Due to the strong degeneracy between the IC and pulsar components, it is not possible to obtain a stable fit to both components simultaneously. To constrain the contribution of the Crab pulsar, we perform an independent phased analysis of the region using a joint fit to on- ($\phi \in [0.0, 0.68]$) and off-pulse ($\phi \in [0.68, 1.0]$) selections in which we set the amplitude of the pulsar to zero in the off-pulse interval. With this analysis, we obtain a best-fit PLE parameterization for the on-pulse pulsar emission with

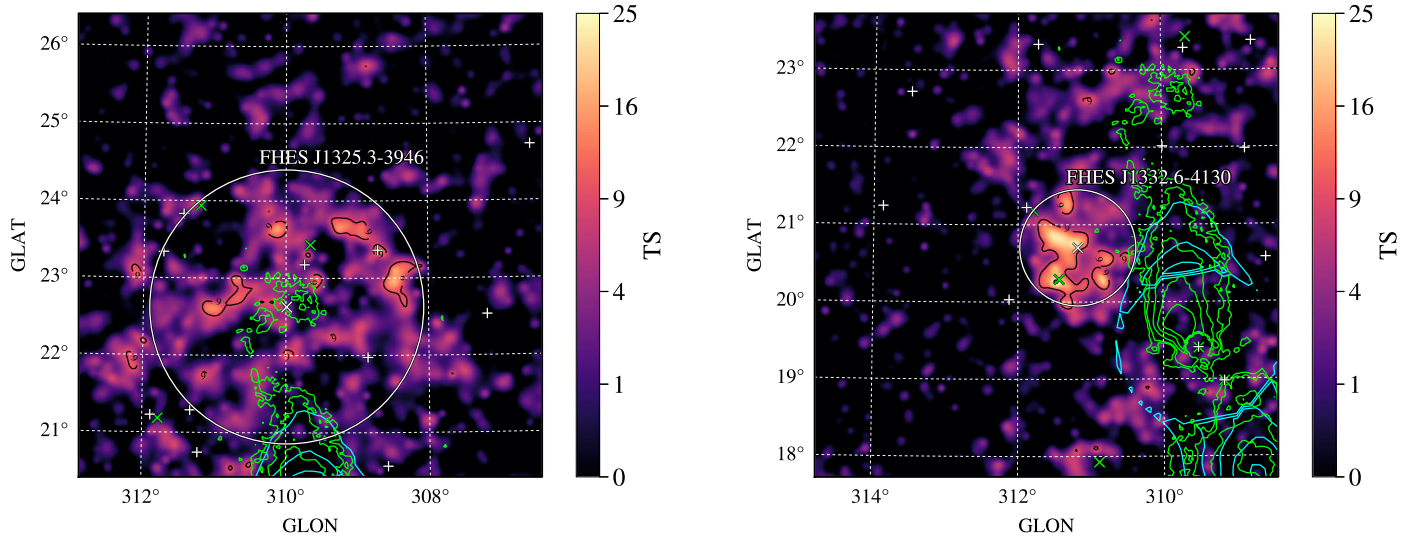

Figure 7. TS maps of FHES J1325.3−3946 and FHES J1332.6−4130, which are associated with the Cen A lobes. The white circle with central marker × indicates the best-fit disk extension and centroid of the FHES source. White crosses indicate the positions of point-source candidates with TS > 9 from the best-fit model for the region. Green crosses indicate the positions of sources in the 3FGL catalog. Overlaid are contours of the LAT γ-ray Cen A Lobes template (cyan) and Parkes radio continuum map at 5 GHz (green).

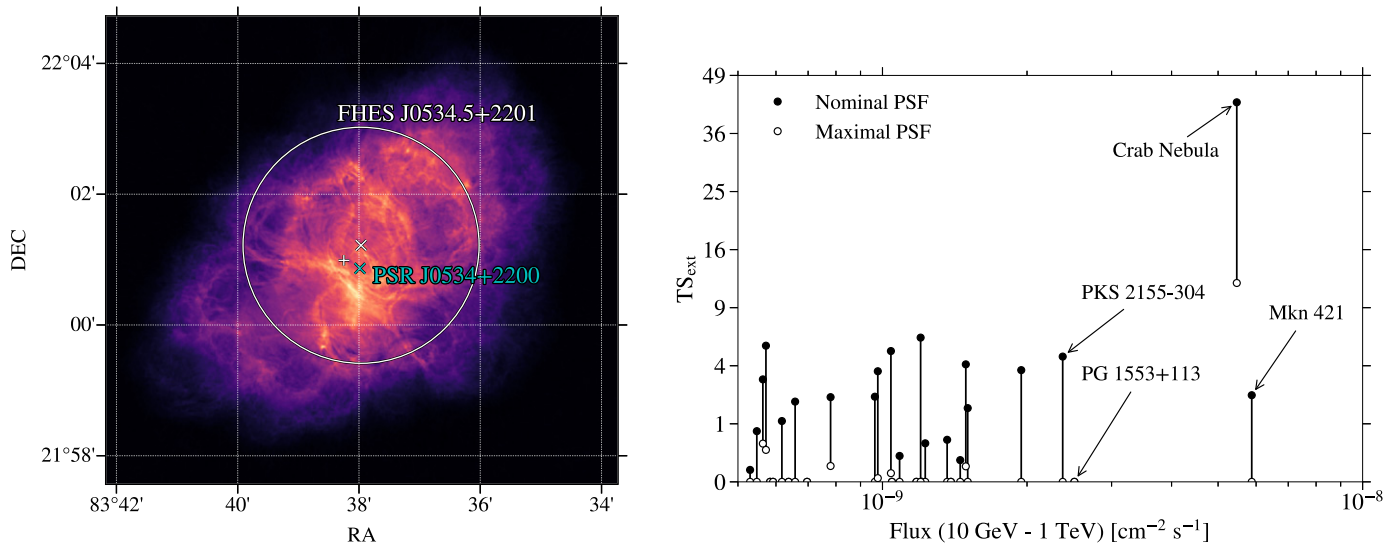

Figure 8. Left: VLA radio image of the Crab Nebula at 3 GHz (Dubner et al. 2017), overlaid with the position and 68% containment radius of FHES J0534.5+2201 (white × marker and circle). The cyan marker indicates the location of PSR J0534+2200 as determined from optical/radio measurements. Right: TS_{ext} vs. photon flux above 10 GeV. Filled and open circles show the value of TS_{ext} obtained with the nominal and bracketing models of the PSF.

$N_0 = 6.06 \times 10^{-9}\,\mathrm{cm^{-2}\,s^{-1}\,MeV^{-1}}$ at 0.635 GeV, $\Gamma = 2.24$, and $E_c = 15.4$ GeV. When fitting the extension of the Crab Nebula, we fix the spectral model of the pulsar to the one obtained from the phased analysis and remove the synchrotron component from the model.

Our analysis detects an extension of $0.^{\circ}030 \pm 0.^{\circ}003 \pm 0.^{\circ}007$ in FHES J0534.5+2201, which is associated with the IC component of the Crab Nebula (3FGL J0534.5+2201i). The left panel of Figure 8 shows a VLA radio image of the Crab Nebula overlaid with the 68% containment radius of FHES J0534.5+2201. The nebula spectrum is fit with an LP that has a spectral index $\alpha = 1.79 \pm 0.04$ and curvature $\beta = (1.67 \pm 0.70) \times 10^{-2}$.

The extension of FHES J0534.5+2201 is comparable to the LAT angular resolution (68% containment radius) for the best-reconstructed events at high energy ($\sim 0.^{\circ}03$ for PSF3 events with $E > 30$ GeV), and is therefore particularly sensitive to systematic uncertainties of the LAT PSF model. Bracketing models for the PSF systematic uncertainty discussed in Section 2.3 were developed by comparing the nominal PSF model derived from Monte Carlo simulations of the detector against the angular distribution of high-latitude blazars.

Using a model that increases the size of the PSF according to Equation (5), we find that TS_{ext} drops from 42.7 to 11.7. In the right panel of Figure 8, we show the value of TS_{ext} obtained for the sources with photon flux above 10 GeV larger than $5 \times 10^{-10}\,\mathrm{cm^{-2}\,s^{-1}}$. If the extension of FHES J0534.5+2201 arises from systematic errors in the PSF, we would expect to see a trend toward increasing TS_{ext} in higher flux objects; however, this was not observed. The BL Lac object Mkn 421, which has comparable flux to the Crab Nebula above 10 GeV, has TS_{ext} of 2.2 and 0.0 for the nominal and bracketing models of the PSF, respectively. Given the absence of significant extension in high-latitude sources of comparable flux, we

conclude that the measured extension is probably intrinsic to the Crab Nebula rather than the result of an instrumental artifact.

Furthermore, the measured extension of FHES J0534.5+2201 agrees well with predictions from simple synchrotron-self-Compton models when the spatial extension of the photon densities is modeled with two-dimensional Gaussian distributions that emit synchrotron radiation in an homogeneous magnetic field (e.g., Hillas et al. 1998; Meyer et al. 2010). In addition, the result is consistent with recent results from the H.E.S.S. Collaboration, who measured an extension of $0.^{\circ}022 \pm 0.^{\circ}001 \pm 0.^{\circ}003$ of the IC component of the nebula above energies of 700 GeV (Holler et al. 2017).[72]

3.2.5. FHES Sources in SFR Regions: FHES J0430.5+3525, FHES J0000.2+6826, FHES J2129.9+5833

SFRs are found in giant molecular clouds. These clouds collapse and produce stars of all spectral types, some of which are massive O- and B-type stars. Because of their relatively short life spans, higher densities of the latter are found in and near their parent SFRs. Those stars produce strong radiation fields, stellar winds, and supernova explosions that create large bubbles in the clouds. The density of SNRs in those regions is larger than the Galactic average. SFRs are thus expected to be sites of efficient cosmic-ray acceleration through different processes (Bykov 2014). Models include diffusive acceleration by the shockwaves of SNRs (Caprioli 2015) and by the termination shock of massive stellar winds (Lang et al. 2005), as well as stochastic acceleration by the magnetic turbulence induced by all those shockwaves (Bykov & Toptygin 2001; Maurin et al. 2016). The Cygnus Cocoon is the only SFR firmly associated with an extended γ-ray source seen by the LAT (Ackermann et al. 2011). It may be associated with the ARGO J2031+4157 source at TeV energies (Bartoli et al. 2014). Other SFRs have potential associations with GeV point sources, such as the G25.0+0.0 region (Katsuta et al. 2017), NGC 3603 (Yang & Aharonian 2017), and Westerlund 2 (Yang et al. 2017), but it is difficult to estimate the contribution from unresolved sources unrelated to cosmic-ray production in such complex regions, as was demonstrated for 30 Doradus in the LMC (Abdo et al. 2010e; Abramowski et al. 2015). Other γ-ray sources detected beyond TeV energies are also tentatively associated with SFRs, such as Westerlund 1 (Ohm et al. 2013) and HESS J1848-018 (Chaves et al. 2008; de Naurois & H.E.S.S. Collaboration 2013). Our analysis finds three extended sources spatially consistent with the directions of SFR regions. They are described in more detail below.

SFRs present unique challenges for modeling the ISM and associated diffuse γ-ray emission. The intense radiation fields near OB associations give rise to sharp gradients in both dust properties and temperature. Both our standard and alternative IEMs use dust corrections derived from the Schlegel-Finkbeiner-Davis (SFD) map of Schlegel et al. (1998). Generally, we have found a correlation between the sources listed in this section and the SFD maps, which trace the interstellar reddening related to the color excess, E(B-V). The SFD map uses a relatively coarse correction for dust temperature, with an angular resolution of $0.^{\circ}7$. In the vicinity of SFRs, where dust temperature can vary on much smaller angular scales, IEM models including SFD information have localized biases that can induce spurious sources (see, e.g., Figure 11 in Abdo et al. 2010c) or suppress real sources.

Because all of the alternative IEMs considered in Section 2.3 use the same SFD-based corrections, we are not able to evaluate the systematic uncertainties associated with these corrections. Comparison with IEMs derived from *Planck* dust maps would test this hypothesis directly. We have analyzed the three extended FHES sources associated with SFRs via an IEM with *Planck*-derived dust corrections that was fit to eight years of `Pass 8` LAT data. As demonstrated in Remy et al. (2017), improved treatment of the IEM rules out some of these (FHES J0430.5+3525 for example) as extended sources. Additionally, we used results from the WHAM Sky Survey to see if any of these sources were spatially coincident with ionized gas missing from the IEM. We found that one source (FHES J0000.2+6826), which partially overlaps with NGC 7822, a SFR at a distance of 1 kpc with a diameter of $\sim 0.^{\circ}4$ (Quireza et al. 2006), is also spatially coincident with a large region of H_{α} emission.

FHES J0000.2+6826 is a soft-spectrum source ($\Gamma = 2.72 \pm 0.11 \pm 0.07$) that is modeled best by a disk with $R_{\rm ext} = 0.^{\circ}98 \pm 0.^{\circ}04 \pm 0.^{\circ}01$. The best-fit model encompasses four 3FGL sources.[73] All four sources are unassociated and were measured in the 3FGL with indices between 2.4 and 2.7. The spectral indices of the 3FGL sources are consistent, within one standard deviation, with the index measured for FHES J0000.2+6826. Figure 9 shows a comparison of the LAT TS map of the region to the H_{α} emission, SFD, and *Planck* dust maps. Although there is no correlation with the cold dust (*Planck*), a large deficit in the SFD map is observed in the southern part of FHES J0000.2+6826. This feature is not observed in the *Planck* map and is likely attributable to dust temperature variations within NGC 7822. The γ-ray map is correlated best with H_{α} emission coming from regions of ionized gas, which is not accounted for in the IEM. For comparison, we have also indicated the location of the dozens of O- and B-type stars in the region in Figure 9. There appears to be an overdensity of O- and B-type stars inside FHES J0000.2+6826, particularly toward the southern edge of the source. As we can not rule out the possibility that the γ-ray emission is due to ionized gas not accounted for in the IEM, we mark this source as confused.

FHES J0430.5+3525 is located near NGC 1579, an SFR at a distance of 700 pc (Kharchenko et al. 2013). It is a soft-spectrum source ($\Gamma = 2.59 \pm 0.11 \pm 0.05$) that is modeled best by a disk with $R_{\rm ext} = 1.^{\circ}11 \pm 0.10 \pm 0.^{\circ}09$. The best-fit model encompasses three 3FGL sources that do not have point-source counterparts.[74] FHES J0430.5+3525 is a composite of these three sources, which are unassociated and also have spectral indices measured in the 3FGL between 2.4 and 2.7. Remy et al. (2017) found that this excess is due to dark neutral gas, and when combining HI, CO, and DNM gas components, the excess toward NGC 1579 disappears (see Figure 7 of Remy et al. 2017).

[72] We note that the H.E.S.S. results are quoted in terms of the width of a 2D Gaussian $\sigma = 0.^{\circ}0145$, whereas our results are given in terms of the 68% confidence radius. The two quantities are related through $r_{68} = \sqrt{-2\sigma^2 \ln(1 - 0.68)}$

[73] 3FGL sources in the region of FHES J0000.2+6826: 3FGL J2356.9+6812, 3FGL J0004.2+6757, 3FGL J0008.5+6853, and 3FGL J2355.4+6939.

[74] The 3FGL sources in the region of FHES J0430.5+3525: 3FGL J0431.7+3503, 3FGL J0426.3+3510, and 3FGL J0429.8+3611c.

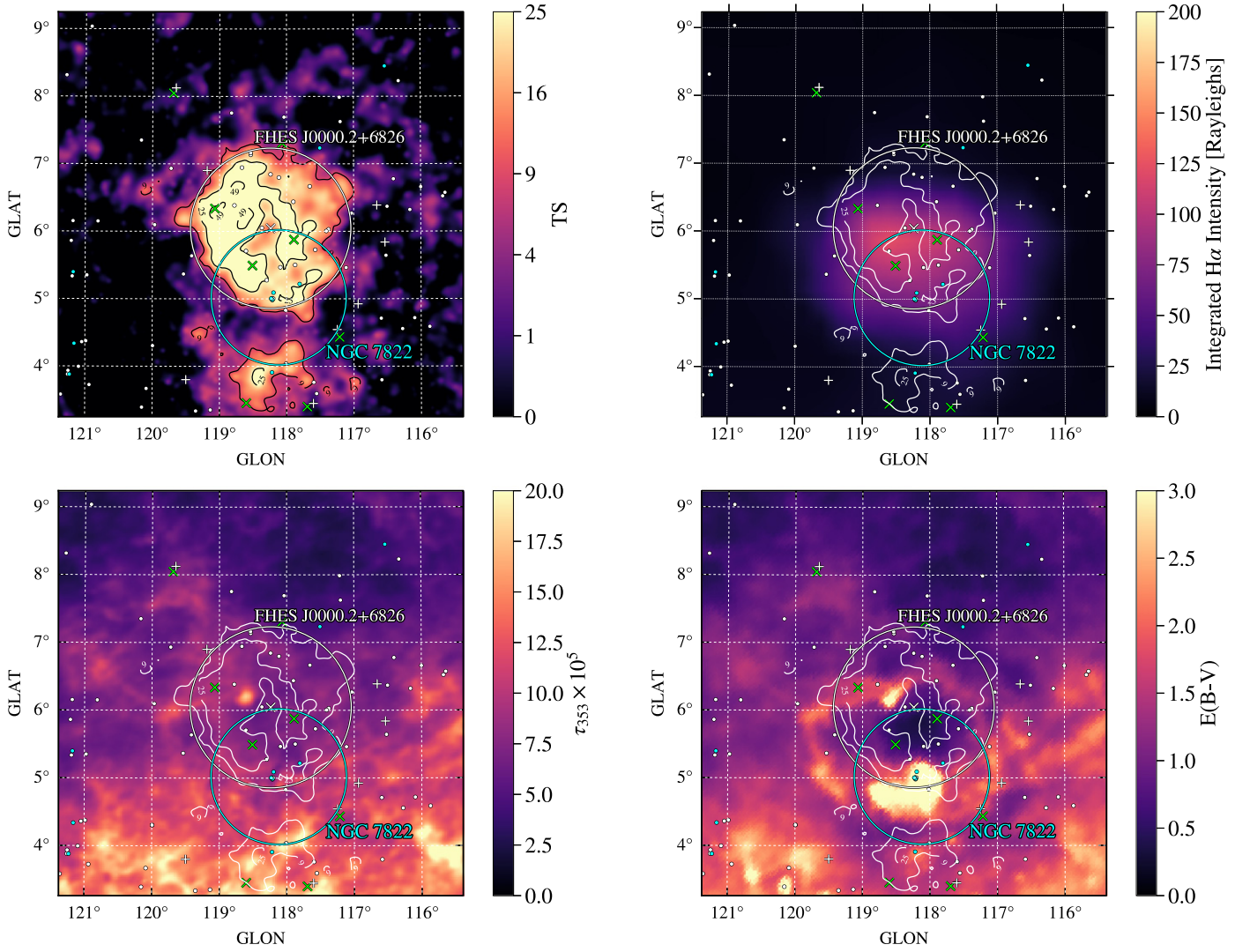

Figure 9. TS map of FHES J0000.2+6826 (top). The top right plot shows the velocity-integrated map of H_α from the WHAM Sky Survey, with the LAT TS isocontours overlaid. Bottom panels show maps of the *Planck* dust optical depth at 353 GHz (left) and SFD dust reddening (right), with LAT TS isocontours overlaid. The white circle with central marker × indicates the best-fit disk extension and centroid of the FHES source. White crosses indicate the positions of point-source candidates with TS > 9 from the best-fit model for the region. The LAT TS isocontours are also shown in white. Green crosses indicate the positions of sources in the 3FGL catalog. Filled white and cyan markers indicate the positions of B and O stars from the SIMBAD database. The cyan circle indicates the location of the H II region NGC 7822.

FHES J2129.9+5833 is located near IC 1396, which is a large and comparatively faint-emission nebula and SFR over 30 pc across, located about 735 pc away. It has an intermediate spectral hardness ($\Gamma = 2.30 \pm 0.12 \pm 0.04$) and is best-modeled spatially by a disk with $R_{\rm ext} = 1\overset{\circ}{.}09 \pm 0\overset{\circ}{.}13 \pm 0\overset{\circ}{.}03$. The γ-ray emission appears to be located primarily in a comparatively low-density region of dust, gas, and stars as seen in Figure 10. No obvious features are visible in either the SFD dust reddening or *Planck* dust optical depth maps of the region. There is a possibility that this is a newly found source belonging to a more common class of extended γ-ray emitters, such as SNRs or PWNe, and not necessarily emission from the SFR itself.

3.2.6. FHES Sources Potentially Associated with SNR/PWN: FHES J1723.5−0501, FHES J1741.6−3917, FHES J2304.0+5406

There are over 30 SNRs and PWNe with known γ-ray emission generally found at lower latitudes, near the Galactic plane (Acero et al. 2016b). Extragalactic SNRs were also detected in the Magellanic Clouds. In addition to the previously detected SNRs CTA 1 and SNR G332.5−05.6 discussed in Sections 3.2.1 and 3.2.2, we find two additional sources, one close to the Galactic plane at $b = -4\overset{\circ}{.}8$ (FHES J1741.6−3917) and the other (FHES J1723.5−0501) at a higher latitude, $b = 17\overset{\circ}{.}9$, which is coincident with an unclassified radio shell. Furthermore, we identify one more source as a potential SNR candidate that, however, lacks a multiwavelength counterpart: FHES J2304.0+5406 at $b = -5\overset{\circ}{.}5$.

FHES J1723.5−0501 is the highest-latitude unassociated candidate, and its TS map is shown in Figure 11 (left). It encompasses a shell-like structure in the NVSS (1.4 GHz) image (Figure 11, right) and has an angular extent of $R_{\rm ext} = 0\overset{\circ}{.}73 \pm 0\overset{\circ}{.}10 \pm 0\overset{\circ}{.}01$ and a hard spectral index ($\Gamma = 1.97 \pm 0.08 \pm 0.06$). The size of the radio shell ($D \sim 0\overset{\circ}{.}7$), seen best along the southwestern edge of the γ-ray emission, is comparable to the size of the FHES source. There are no previously known SNRs at this location. FHES J1723.5−0501 encompasses the unassociated source

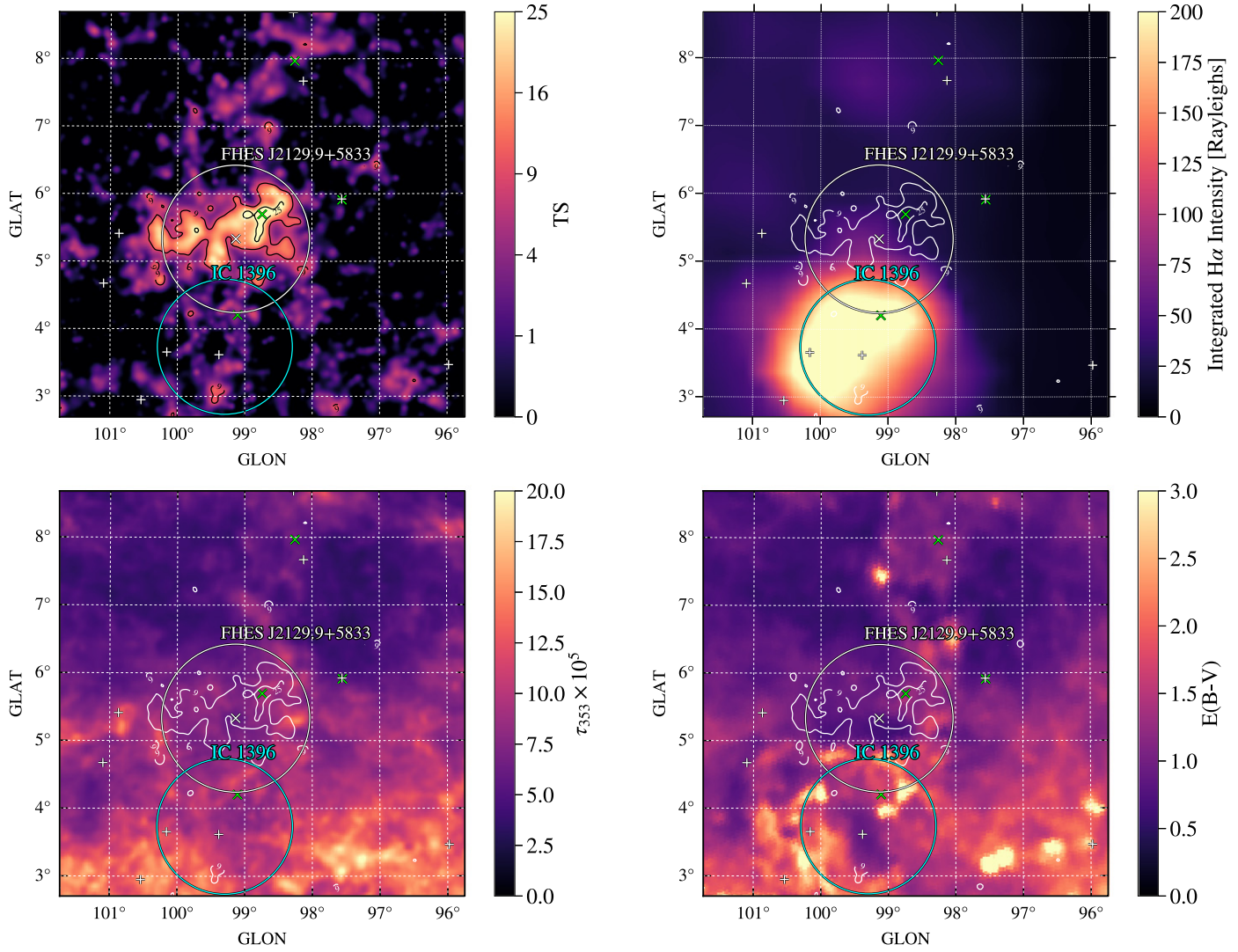

Figure 10. TS map of FHES J2129.9+5833 (top). The top right plot shows the velocity-integrated map of H_α from the WHAM Sky Survey, with the LAT TS isocontours overlaid. Bottom panels show maps of *Planck* dust optical depth at 353 GHz (left) and SFD dust reddening (right), with LAT TS isocontours overlaid. The white circle with central marker × indicates the best-fit disk extension and centroid of the FHES source. White crosses indicate the positions of point-source candidates with TS > 9 from the best-fit model for the region. The LAT TS isocontours are also shown in white. Green crosses indicate the positions of sources in the 3FGL catalog. The cyan circle indicates the location of the H II region IC 1396.

3FGL J1725.0−0513, which does not have a point-source counterpart in our model of the region. Given its high latitude, we suggest that this source could be associated with a type Ia SNR because these are not necessarily located close to the regions of star formation. SN 1006 represents an example of a remnant of a type Ia supernova explosion detected in γ-rays at high Galactic latitude (Condon et al. 2017).

FHES J1741.6−3917 has a large angular extent ($R_{\rm ext} = 0.^\circ35 \pm 0.^\circ03 \pm 0.^\circ29$) and encompasses the known, radio-detected SNR G351.0−5.4 (de Gasperin et al. 2014). However, the γ-ray emission appears to be much larger than the radio SNR. The TS map is shown in Figure 12. It has a hard spectral index ($\Gamma = 1.80 \pm 0.04 \pm 0.06$), which suggests that it may be associated with a young, shell-type SNR similar to, e.g., Tycho's SNR or Cas A (Abdo et al. 2010d; Archambault et al. 2017a). FHES J1741.6−3917 is near to, or encompasses, three point sources that have direct 3FGL counterparts: 3FGL J1748.5−3912, 3FGL J1733.5−3941, and 3FGL J 1747.6−4037. Sources 3FGL J1748.5−3912 and 3FGL J 1733.5−3941 are both unassociated. Source 3FGL J1747.6 −4037 is located on the southern edge of FHES J1741.6−3917 and is associated with the millisecond pulsar PSR J1747 −4036. We note that the characteristics of FHES J1741.6 −3917 match well with the new γ-ray source G350.6−4.7 reported by Araya (2018), based on an analysis of eight years of LAT data. Source G350.6−4.7 is found at the same location ($l = 350.^\circ6$, $b = -4.^\circ7$), with similar angular extent and spectrum ($\Gamma = 1.68 \pm 0.04 \pm 0.14$, $R = 1.^\circ7 \pm 0.^\circ2$).

In addition to the previous sources, we also found one new unassociated hard-spectrum source. The hardness of the spectrum for FHES J2304.0+5406 ($\Gamma = 1.95 \pm 0.08 \pm 0.15$) may imply an association with an SNR or PWN. However, there is no clear overlap with known objects in the TeV, X-ray, or radio wavelengths in the considered multi-wavelength surveys and catalogs. For this extended object, there are 3FGL and 3FHL sources within the 68% containment

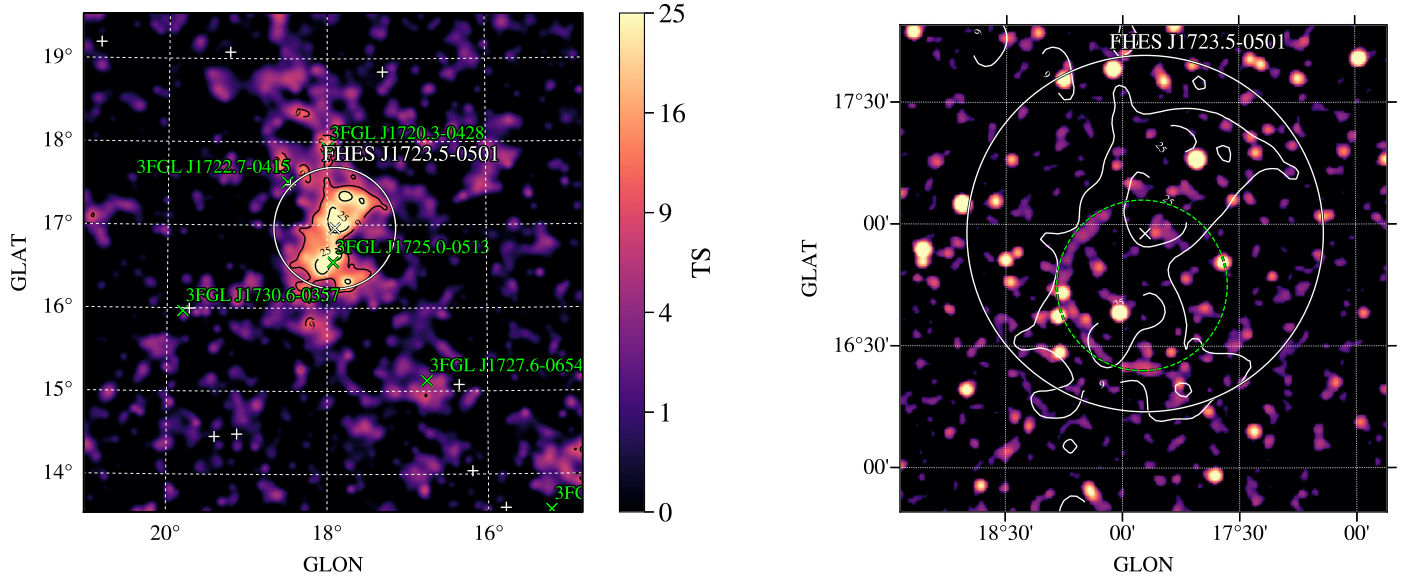

Figure 11. Left: TS map of FHES J1723.5−0501. The white circle with central marker × indicates the extension (68% containment radius) and centroid of the FHES source. White crosses indicate the positions of point-source candidates with TS > 9 from the best-fit model for the region. Green crosses indicate the positions of sources in the 3FGL catalog. Right: map of continuum emission at 1.4 GHz from NVSS (Condon et al. 1998), smoothed with a Gaussian kernel of radius 0.°012. White contours show the TS map of FHES J1723.5−0501. The dashed green circle traces the circular feature observed in the radio map.

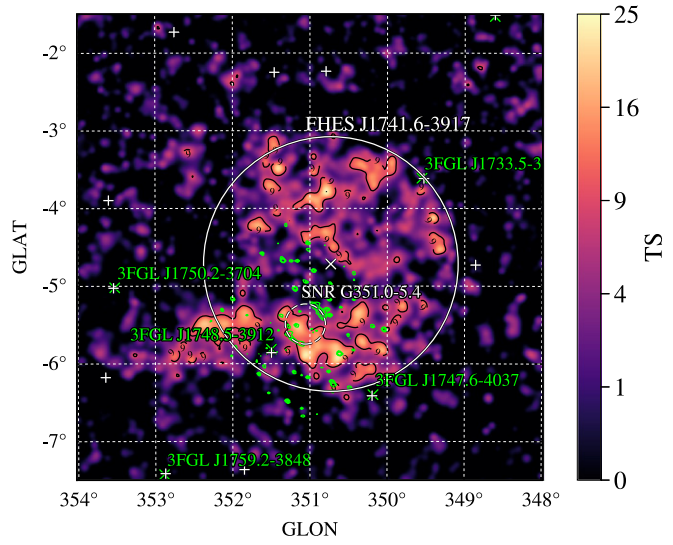

Figure 12. TS map (Γ = 2) of FHES J1741.6−3917. The white circle with central marker × indicates the best-fit disk extension and centroid of the FHES source. White crosses indicate the positions of point-source candidates with TS > 9 from the best-fit model for the region. Green crosses indicate the positions of sources in the 3FGL catalog. Green contours show the GMRT radio map of SNR G351.0−5.4 at 325 MHz from de Gasperin et al. (2014).

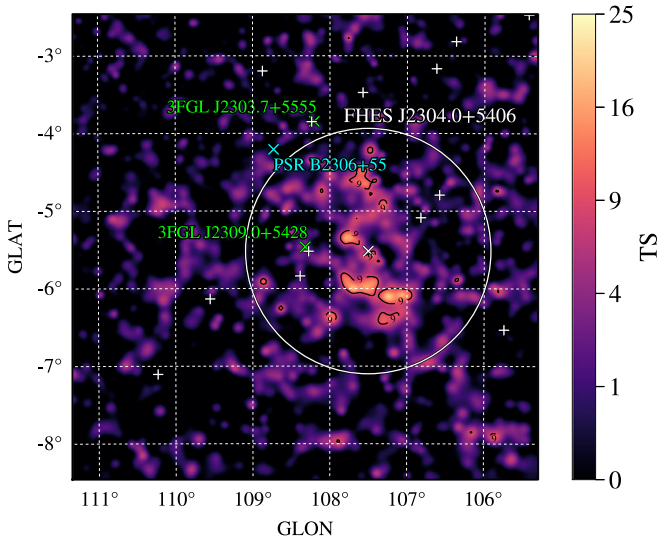

Figure 13. TS map of the unassociated, hard-spectrum source FHES J2304.0 +5406. The map is generated with a point-source morphology and a PL spectrum (Γ = 2). The white circle with central marker × indicates the extension (68% containment radius) and centroid of the FHES source. White crosses indicate the positions of point-source candidates with TS > 9 from the best-fit model for the region. Green crosses indicate the positions of sources in the 3FGL catalog.

radius; however, both 3FGL/3FHL sources have point-source counterparts in our model. They are hence presumably unrelated to the FHES sources.[75]

FHES J2304.0+5406 has a large angular extent ($R_{\rm ext}$ = 1.58 ± 0.35 ± 0.°17), as seen in the TS map shown in Figure 13 (right). There is a nearby pulsar PSR B2306+55 (∼2 kpc away) at the northwest edge of the source. However, it is quite old (∼10 Myr), so any associated SNR would be too old to drive particle acceleration. Additionally, the pulsar has a relatively low spin-down power (7.3×10^{31} erg s^{-1}), which would be too low to power a γ-ray bright PWN (Acero et al. 2013).

3.2.7. Unassociated Soft-spectrum Sources: FHES J1501.0−6310, FHES J2208.4+6443

The remaining two soft-spectrum candidates have spectral indices similar to that expected for Galactic diffuse emission (Γ ∼ 2.7).

FHES J1501.0−6310 is fit best with an extension of size $R_{\rm ext}$ = 1.°29 ± 0.°13 ± 0.°25 and a spectral index of Γ = 2.44 ± 0.09 ± 0.07. The TS map is shown in Figure 14 (left).

[75] The sources are: 3FHL 2308.8+5424, with an angular separation of 0.°77 and spectral index Γ = 2.06 ± 0.53; and 3FGL 2309.0+5428, with a separation of 0.°82 and Γ = 1.70 ± 0.25. The 3FHL source is associated with 1RXS J2300852.2+542559, an AGN of unknown class.

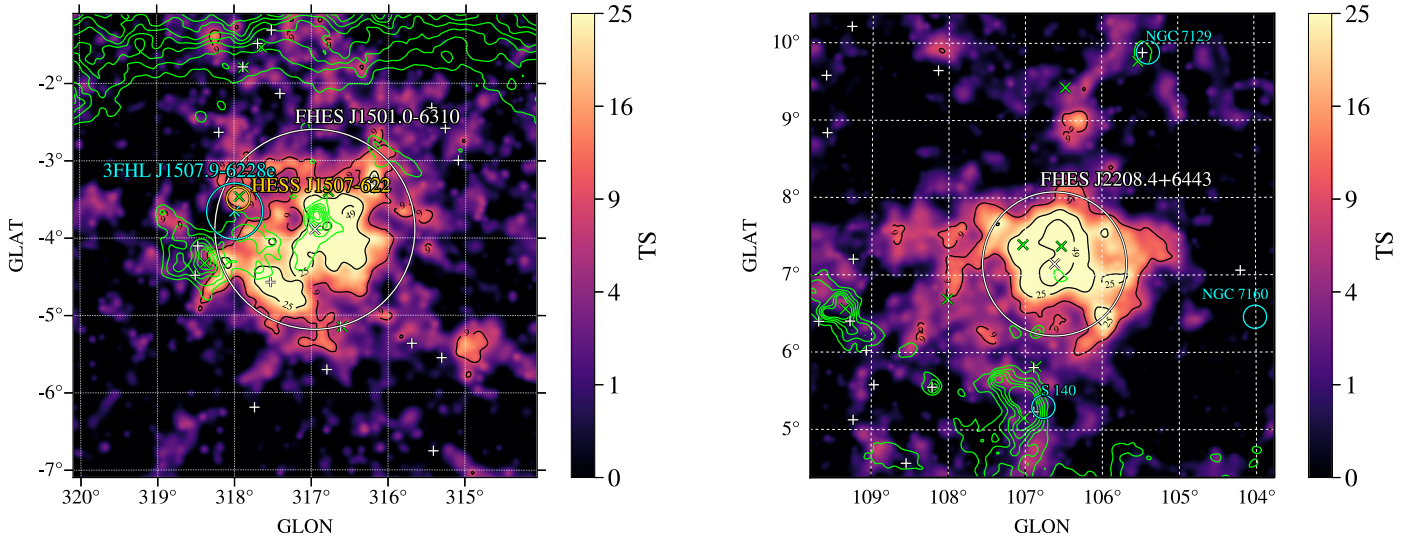

Figure 14. TS maps of unassociated, soft-spectrum sources FHES J1501.0−6310 (left) and FHES J2208.4+6443 (right). Green contours show the *Planck* dust optical depth at 353 GHz. The white circle with central marker × indicates the extension (68% containment radius) and centroid of the FHES source. White crosses indicate the positions of point-source candidates with TS > 9 from the best-fit model for the region. Green crosses indicate the positions of sources in the 3FGL catalog. The 3FHL and H.E.S.S. source extensions are shown as cyan and yellow contours (left). Cyan circles indicate the locations of H II regions (right).

Three 3FGL/3FHL sources have an angular separation $d < R_{\rm ext}$, namely 3FGL J1457.6–6249 ($d = 0.^\circ53$), 3FGL J1503.7–6426 ($d = 0.^\circ94$), and 3FHL J1507.9–6228e ($d = 1.^\circ40$); they have spectra $\Gamma = 2.45 \pm 0.12$, $\Gamma = 2.33 \pm 0.07$, and $\Gamma = 1.86 \pm 0.15$, respectively. The source 3FGL J1503.7–6426 is classified as a blazar of unknown type, while the other sources do not have a multiwavelength counterpart. In our model, 3FHL J1507.9–6228e is an extended source that replaces 3FGL J1506.6–6219; it is represented spatially as a disk of radius $0.^\circ36$. This source may be associated with the unidentified H.E.S.S. source HESS J1507–622 (Acero et al. 2011), which is located at the same position but has a smaller spatial extent ($R = 0.15 \pm 0.^\circ02$). The 3FHL/3FGL sources have harder spectra than the FHES source, yet the measured spectral index of the latter fits well with the spectral index of the H.E.S.S. source ($\Gamma = 2.24 \pm 0.16_{\rm stat} \pm 0.20_{\rm sys}$) and the one found in a dedicated *Fermi* analysis of TeV detected PWNe that gave $\Gamma = 2.33 \pm 0.48$ for energies above 10 GeV (Acero et al. 2013). The 3FHL and H.E.S.S. source extensions are shown as cyan and yellow contours, respectively (Figure 14; left). We also show the *Planck* dust optical depth contours (green contours). The FHES source encompasses the regions with high dust optical depth that are in the direction of the Circinus molecular cloud complex.

FHES J2208.4+6443 comprises the two unassociated 3FGL sources (3FGL J2206.5+6451 with $d = 0.^\circ25$ and $\Gamma = 2.84 \pm 0.25$, as well as 3FGL J2210.2+6509 with $d = 0.^\circ48$ and $\Gamma = 2.48 \pm 0.16$). It has an angular extent $R_{\rm ext} = 0.^\circ93 \pm 0.^\circ11 \pm 0.^\circ11$ and a spectral index of $\Gamma = 2.78 \pm 0.14 \pm 0.15$, making it the softest source in our analysis. Both 3FGL sources are unassociated. The FHES source is located within the Cepheus Bubble, which is a large region ($D \sim 10^\circ$) containing several SFRs (Ábrahám et al. 2000; Kun et al. 2008). Although not located within an SFR, FHES J2208.4+6443 is in the vicinity of several, the nearest being S140 (∼2° south at the peak of the dust map), NGC 7129 (∼2° north), and NGC 7160 (∼2° east). We note that IC 1396, which is tentatively associated with FHES J2129.9+5833, is an SFR that also lies in the Cepheus Bubble.

4. Search for Extended Emission from Extragalactic Sources

All of the unassociated extended sources in our analysis are detected at Galactic latitudes $|b| < 20^\circ$, indicating a Galactic origin. We now turn to sources at higher latitudes. These are most probably of extragalactic origin. The most common extragalactic sources observed at γ-ray energies are blazars (radio-loud AGNs with their jets orientated closely to the line of sight). As discussed in Section 1 and further below, extended emission of blazars could be caused by secondary γ-rays from electromagnetic cascades. Interestingly, some authors found evidence for extended emission around AGNs in analyses of *Fermi*-LAT data (Chen et al. 2015a; Kotelnikov et al. 2015), while others did not detect any significant extension with combined *Fermi*-LAT and H.E.S.S. observations (Abramowski et al. 2014), VERITAS observations (Archambault et al. 2017b), or *Fermi*-LAT data only (Neronov et al. 2011; Ackermann et al. 2013).

Alternatively, extended γ-ray emission from unassociated sources could be due to a DM annihilation signal from sub-halos of the Milky Way. Searches performed on the unassociated 3FGL sources have yielded upper limits (Buckley & Hooper 2010; Ackermann et al. 2012) or are inconclusive (Mirabal et al. 2012). Recently, however, two possible DM sub-halos were identified (Bertoni et al. 2016; Xia et al. 2017), on which we comment below.

4.1. High-latitude Extended Candidates

To search for sub-threshold extended extragalactic candidates, we examine a sample of 1688 high-latitude point sources listed in the 3FGL and 3FHL with $|b| > 20^\circ$ containing 1360 AGN and 328 unassociated sources. In composing this sample, we exclude high-latitude sources detected as extended (FHES J1325.3−3946, FHES J1332.6−4130, FHES J0043.1+4112, and FHES J0322.2−3710) and sources with pulsar

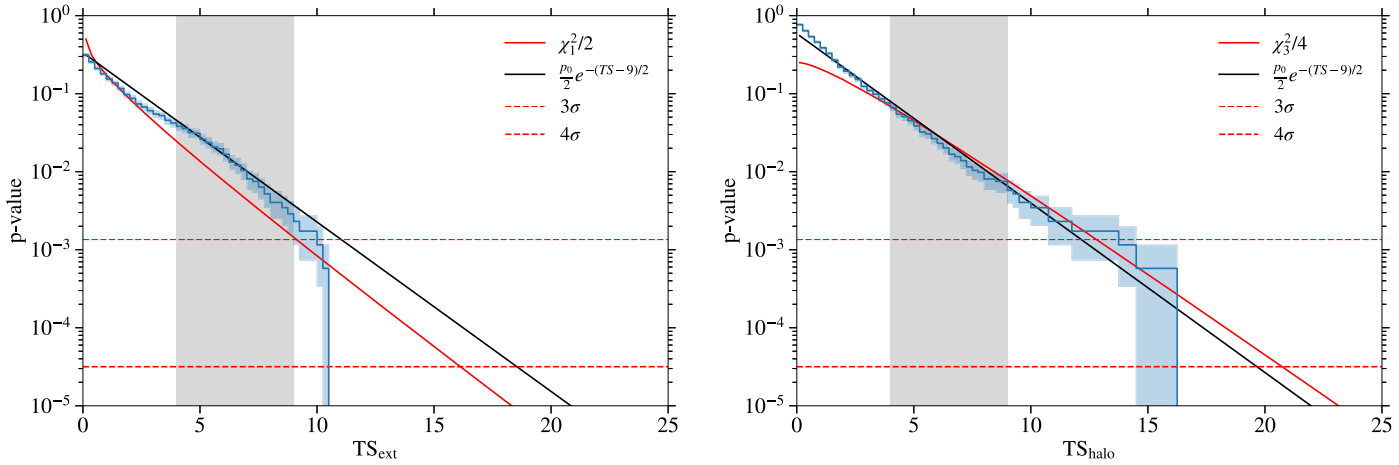

Figure 15. Cumulative distributions of TS_{ext} (left) and TS_{halo} (right) derived from 1688 FHES sources in the high-latitude sample ($|b| > 20°$). The solid black line shows the best fit to the distribution derived with parameterization in Equation (7). The shaded region indicates the range of the distribution that was used to fit the parameterization. The red curve is the theoretical distribution for a likelihood ratio with the number of degrees of freedom of the given test.

Table 5
Analysis Results for the Five Most Significant High-latitude Extended Source Candidates ($|b| > 20°$)

Name	l (deg)	b (deg)	Association	Class	z	TS_{ext}	p_{local}	R_{ext}(deg)	Δ_{ext}
3FGL J2142.2−2546	23.41	−47.98	PMN J2142−2551	bcu	⋯	10.6	3.0×10^{-3} (2.7σ)	0.14 ± 0.03	⋯
3FGL J0002.2−4152	334.25	−71.99	1RXS J000135.5−415519	bcu	⋯	10.4	3.3×10^{-3} (2.7σ)	0.12 ± 0.03	⋯
3FGL J2103.9−6233	332.69	−38.95	PMN J2103−6232	bcu	⋯	10.1	3.7×10^{-3} (2.7σ)	0.07 ± 0.01	⋯
3FGL J0107.0−1208	137.64	−74.63	PMN J0107−1211	bcu	⋯	9.5	4.8×10^{-3} (2.6σ)	0.64 ± 0.12	−1.9
3FGL J0434.3−1411c	210.82	−36.55	CO cloud		⋯	9.2	5.4×10^{-3} (2.5σ)	0.77 ± 0.17	−0.1

Note. Here, Δ_{ext} is the difference in the Akaike Information Criterion between the best-fit extended source model and a model with one additional point source (see Equation (1)).

Table 6
Analysis Results for the Five Most Significant High-latitude Halo Candidates ($|b| > 20°$)

Name	l (deg)	b (deg)	Association	Class	z	TS_{halo}	p_{local}	R_{halo}(deg)	Γ_{halo}	Δ_{halo}
3FGL J0850.0+4855	170.47	39.27	GB6 J0850+4855	bll	⋯	16.3	1.2×10^{-4} (3.7σ)	0.52 ± 0.13	2.15 ± 0.22	−7.8
3FHL J0901.5+6712	147.19	37.28	1RXS J090140.8+671158		⋯	14.7	2.7×10^{-4} (3.5σ)	0.78 ± 0.25	4.00 ± 0.28	⋯
3FGL J0107.0−1208	137.64	−74.63	PMN J0107−1211	bcu	⋯	13.8	4.4×10^{-4} (3.3σ)	0.75 ± 0.15	2.10 ± 0.21	−2.5
3FGL J0626.6−4259	251.05	−22.44	1RXS J062635.9−425810	bcu	⋯	10.8	1.9×10^{-3} (2.9σ)	0.66 ± 0.21	2.13 ± 0.22	−1.1
3FGL J2318.6+1912	94.49	−38.40	TXS 2315+189	bcu	⋯	10.8	2.0×10^{-3} (2.9σ)	0.57 ± 0.18	2.62 ± 0.32	−5.6

Note. Here, Δ_{halo} is the difference in the Akaike Information Criterion between the best-fit halo model and a model with one additional point source (see Equation (1)).

associations. At these high Galactic latitudes, the intensity of the Galactic diffuse emission is much lower and the effect of systematic uncertainties from the IEM should be less severe. Tables 5 and 6 present the five most significant sub-threshold candidates when ordering sources by TS_{ext} and TS_{halo}.

In the absence of systematic effects, we expect the null distributions of TS_{ext} and TS_{halo} to follow a mixture of χ^2 distributions. However, modeling uncertainties can cause deviations from a purely statistical distribution. These uncertainties could include systematic uncertainties in the IEM and IRFs or the contribution of unresolved sources. Rather than model these systematic effects directly, we derive an empirical model for the null distribution by fitting a function to the measured distributions of TS_{ext} and TS_{halo} in our sample. We model the tail of the distributions with an exponential function:

$$f(\mathrm{TS}_{\mathrm{ext/halo}}; p_0) = \frac{p_0}{2} e^{-(\mathrm{TS}_{\mathrm{ext/halo}}-9)/2}, \quad (7)$$

where p_0 is the p-value for $TS_{ext/halo} > 9$. We restrict our fit to the range of the TS distribution between 4 and 9 where the upper bound is chosen to avoid biasing the fit with the distribution of genuinely extended sources that may be detected with $TS_{ext/halo} > 9$.

In Figure 15, we show the cumulative distribution of TS_{ext} and TS_{halo} against the best-fit parameterization derived with Equation (7). We find best-fit values of $p_0 = 3.51 \times 10^{-3}$ and $p_0 = 6.14 \times 10^{-3}$ for TS_{ext} and TS_{halo}, respectively. In the case of TS_{ext}, we expect the distribution to follow $\chi^2_1/2$ (one bounded degree of freedom), which has a tail probability 1.35×10^{-3} for $TS_{ext/halo} > 9$. The larger than expected tail probability implies that IRF or modeling uncertainties are skewing the distribution toward higher TS_{ext} values. In the case of TS_{halo}, we expect the distribution to follow $\chi^2_3/4$ (three degrees of freedom with two bounded parameters). Here, we observe a better match with the theoretical expectation.

Using these parameterizations, we derive the values of $p_{\rm local}$ shown in Tables 5 and 6.

We note that the parameterization of Equation (7) ignores the potential influence of source properties (e.g., latitude, flux, or spectral hardness) on the distribution of $\mathrm{TS_{halo}}$ and $\mathrm{TS_{ext}}$. Distributions of $\mathrm{TS_{halo}}$ and $\mathrm{TS_{ext}}$ for different subpopulations did not show a strong relationship with source properties, and accounting for these differences in the parameterization would have had a small effect on the implied local significance. When examining all FHES sources, the largest effect was seen when comparing low- and high-latitude sources ($|b| < 20^\circ$ and $|b| \geqslant 20^\circ$); the distribution of low-latitude sources was found to be more skewed toward large TS values. This effect could be attributed to genuine sub-threshold sources of Galactic origin or the influence of residuals in the IEM. A similar effect was observed in the $\mathrm{TS_{ext}}$ distributions of fainter ($\mathrm{TS} < 100$) versus brighter ($\mathrm{TS} > 100$) sources. This behavior is consistent with the greater susceptibility of faint sources to confusion due to their higher spatial density.

The two most significant candidates are 3FGL J0850.0+4855, with $\mathrm{TS_{halo}} = 16.3$ (3.6σ), and 3FGL J2142.2−2546, with $\mathrm{TS_{ext}} = 10.6$ (2.9σ). The former is associated with low synchrotron peak (LSP) BL Lac object GB6 J0850+4855 at unknown redshift, and the latter is associated with PMN J2142−2551, an active galaxy of uncertain type (bcu class) with unknown redshift. Both objects are consistent with an intermediate extension ($0\overset{\circ}{.}14$ and $0\overset{\circ}{.}5$) that could suggest confusion with a nearby sub-threshold point source. Although both sources have similar spectral indices ($\Gamma \sim 2.4$), 3FGL J2142.2−2546 (the extension candidate) is detected with a much lower significance than 3FGL J0850.0+4855 (the halo candidate) ($\mathrm{TS} = 81.4$ versus $\mathrm{TS} = 1771.4$).

We evaluate the global significance of the two highest TS candidates by treating every object in the high-latitude sample as an independent trial, such that the probability of observing an object with $p_{\rm local} > p$ is $1 - (1 - p)^N$, where N is the trials factor corresponding to the number of objects in our sample. Using a trial factor of 1688 for the number of sources in the high-latitude sample, we derive global significances for 3FGL J2142.2−2546 and 3FGL J0850.0+4855 of -1.5σ and 0.7σ, respectively. The most significant unassociated source is 3FGL J0434.3−1411c, which has $\mathrm{TS_{ext}} = 9.2$ (2.7σ) and a global significance of -0.4σ. We conclude that both are consistent with being drawn from our parameterizations for the null distributions of $\mathrm{TS_{ext}}$ and $\mathrm{TS_{halo}}$.

4.2. High-latitude Unassociated Sources

There are 328 unassociated objects in the high-latitude sample. With no obvious counterparts at other wavelengths, the γ-ray emission of these sources could be due to annihilation of DM particles in DM subhalos of the Milky Way. Due to the proximity of such subhalos to Earth, the emission could likely be extended. We find no evidence for an individual unassociated source with statistically significant extension.

Several other recent works have identified possible DM subhalo candidates among the sample of unassociated 3FGL sources. Bertoni et al. (2016) identify 3FGL J2212.5+0703 as an unassociated source that shows evidence for spatial extension of $0\overset{\circ}{.}25$ with a statistical significance of 5.1σ, although they also find that a model with a second nearby point source provides an equally good fit to the data. Xia et al. (2017) identify 3FGL J1924.8−1034 as another potential DM subhalo candidate and report a significance for spatial extension of 5.4σ for a best-fit extension radius of $0\overset{\circ}{.}15$. Our analysis finds no evidence for significant extension in either of these sources ($\mathrm{TS_{ext}} \sim 0$). In both cases, a model with two close point sources is strongly preferred over one with angular extension ($\Delta_{\rm ext} = 11.9$ and $\Delta_{\rm ext} = 29.4$ for 3FGL J2212.5+0703 and 3FGL J1924.8−1034, respectively).

4.3. Individual TeV-selected AGNs

AGNs with strong TeV emission are among the best candidates for secondary cascade emission because the amplitude of the cascade component is expected to be proportional to the fraction of the primary emission that is absorbed by the EBL. We consider the sample of 38 TeV-selected AGNs compiled in Biteau & Williams (2015), which have all been detected above ∼100 GeV. The cascade component could appear as an extended component superimposed on the point-like emission of the AGN.

Table 7 shows the analysis results for all objects in the TeV-selected AGN sample. No source shows evidence for extension with $\mathrm{TS_{ext}} > 9$, and upper limits on the angular extension lie between $0\overset{\circ}{.}02$ and $0\overset{\circ}{.}09$. PKS 1510−08 shows a hint of a halo component with $\mathrm{TS_{halo}} = 9.4$ (2.6σ), where the significance is quoted prior to trial penalization. However, the halo model is only marginally preferred over a model with an additional point source ($\Delta_{\rm halo} \sim 0$). Using the model for the null distribution of $\mathrm{TS_{halo}}$ derived in Section 4.1 and a trials factor of 38, we find a global significance for halo emission associated with PKS 1510−08 of 0.9σ.

4.4. Stacking Analysis

Interest in stacking *Fermi*-LAT data to search for IGMF induced pair halos was partly triggered by the initial study of Ando & Kusenko (2010), who found a hint of extension in the stacked images of 170 AGNs observed over 11 months. In their analysis, AGNs detected above 10 GeV at large Galactic latitudes, $|b| > 10^\circ$, were compared to an early version of the PSF based on ground-based beam tests as well as Monte-Carlo simulations. A comparison to the profile of the Crab Nebula by Neronov et al. (2011) nonetheless suggested an instrumental effect. This was further investigated by the *Fermi*-LAT collaboration (Ackermann et al. 2013) with an updated PSF based on on-orbit data, using bright pulsars (Vela and Geminga) as control point-like sources. The AGN and pulsar extensions relative to the PSF proved to be consistent with zero in the 3–30 GeV energy range, where both samples contain ample statistics. More recently, Chen et al. (2015a) selected, a priori, a subset of 24 nearby high-synchrotron-peaked BL Lacs (HSP). It was searched for potential IGMF-induced extension and compared with reference samples of 26 flat-spectrum radio quasars (FSRQs), as well as the Geminga and Crab pulsars. This yielded a 2.3σ indication for extension in the HSP sample around 1 GeV.

We search for extended emission by stacking 3FHL and 3FGL samples of AGN from which significant cascade emission could be expected. The considered samples are:

1. *HSPs.* We select HSPs with a synchrotron peak $\nu_{\rm sync} > 10^{15}$ Hz. Such sources are promising emitters of very-high-energy γ rays necessary to induce the cascade. This selection leaves us with 299 sources.

Table 7
Analysis Results for the Sample of 38 TeV-selected AGN

Name	l (deg)	b (deg)	Association	z	Class	Energy Flux (eV cm^{-2} s^{-1})	TS$_{\rm ext}$	$R_{\rm ext}$ (deg)	TS$_{\rm halo}$	$\Delta_{\rm halo}$
3FGL J0013.9−1853	74.53	−78.09	RBS 0030	0.094	bll	1.1 ± 0.4	0.0	<0.05	0.1	⋯
3FGL J0152.6+0148	152.38	−57.54	PMN J0152+0146	0.080	bll	4.0 ± 0.8	0.0	<0.04	0.8	⋯
3FGL J0222.6+4301	140.15	−16.77	3C 66A	0.444	BLL	42.1 ± 2.5	0.1	<0.02	0.4	⋯
3FGL J0232.8+2016	152.94	−36.59	1ES 0229+200	0.139	bll	2.0 ± 0.6	0.0	<0.05	0.9	⋯
3FGL J0303.4−2407	214.62	−60.18	PKS 0301−243	0.260	BLL	18.4 ± 1.9	0.0	<0.02	0.5	⋯
3FGL J0316.6+4119	150.19	−13.71	IC 310	0.019	rdg	1.6 ± 0.6	0.0	<0.05	1.9	⋯
3FGL J0319.8+1847	165.10	−31.70	RBS 0413	0.190	bll	4.1 ± 0.9	7.7	<0.09	6.7	⋯
3FGL J0349.2−1158	201.93	−45.71	1ES 0347−121	0.185	bll	2.7 ± 0.8	1.3	<0.08	1.2	⋯
3FGL J0416.8+0104	191.81	−33.16	1ES 0414+009	0.287	bll	3.7 ± 0.9	0.0	<0.05	0.0	⋯
3FGL J0449.4−4350	248.80	−39.92	PKS 0447−439	0.205	bll	37.2 ± 2.6	0.0	<0.03	0.2	⋯
3FGL J0521.7+2113	183.60	−8.71	TXS 0518+211	0.108	bll	39.6 ± 2.7	0.4	<0.03	3.4	⋯
3FGL J0648.8+1516	198.98	6.33	RX J0648.7+1516	0.179	bll	11.8 ± 1.6	0.0	<0.04	0.3	⋯
3FGL J0710.3+5908	157.41	25.42	1H 0658+595	0.125	bll	4.8 ± 0.9	0.0	<0.02	0.0	⋯
3FGL J0721.9+7120	143.98	28.02	S5 0716+71	0.127	BLL	34.0 ± 1.8	0.0	<0.03	4.1	⋯
3FGL J0809.8+5218	166.25	32.91	1ES 0806+524	0.138	bll	15.0 ± 1.5	0.0	<0.03	0.3	⋯
3FGL J1010.2−3120	266.91	20.05	1RXS J101015.9−311909	0.143	bll	5.8 ± 1.1	0.0	<0.02	0.0	⋯
3FGL J1015.0+4925	165.53	52.71	1H 1013+498	0.212	bll	34.5 ± 2.4	0.0	<0.02	0.5	⋯
3FGL J1103.5−2329	273.18	33.08	1ES 1101−232	0.186	bll	3.8 ± 0.9	0.1	<0.07	2.8	⋯
3FGL J1104.4+3812	179.83	65.04	Mkn 421	0.031	BLL	222.3 ± 6.5	2.2	<0.02	1.6	⋯
3FGL J1136.6+7009	131.90	45.65	Mkn 180	0.045	bll	6.1 ± 0.9	0.0	<0.02	0.5	⋯
3FGL J1217.8+3007	188.85	82.06	1ES 1215+303	0.130	bll	20.5 ± 1.9	0.0	<0.03	2.0	⋯
3FGL J1221.3+3010	186.40	82.74	PG 1218+304	0.182	bll	22.9 ± 2.2	3.1	<0.04	3.1	⋯
3FGL J1221.4+2814	201.69	83.29	W Comae	0.103	bll	5.1 ± 0.9	5.9	<0.07	4.1	⋯
3FGL J1224.9+2122	255.06	81.66	4C +21.35	0.435	FSRQ	13.5 ± 1.3	1.1	<0.03	1.6	⋯
3FGL J1256.1−0547	305.10	57.06	3C 279	0.536	FSRQ	11.4 ± 1.1	5.5	<0.05	4.3	⋯
3FGL J1314.7−4237	307.56	20.05	MS 13121−4221	⋯	bcu	2.8 ± 0.8	0.0	<0.03	0.8	⋯
3FGL J1427.0+2347	29.49	68.20	PKS 1424+240	⋯	BLL	45.4 ± 2.8	4.1	<0.03	3.2	⋯
3FGL J1428.5+4240	77.50	64.90	H 1426+428	0.129	bll	6.2 ± 1.1	2.4	<0.04	1.0	⋯
3FGL J1512.8−0906	351.28	40.14	PKS 1510−08	0.360	FSRQ	20.6 ± 1.5	2.2	<0.04	9.4	−1.8
3FGL J1555.7+1111	21.91	43.96	PG 1553+113	⋯	BLL	84.8 ± 3.9	0.0	<0.02	5.3	⋯
3FGL J1653.9+3945	63.60	38.85	Mkn 501	0.034	BLL	78.5 ± 3.7	3.7	<0.03	3.5	⋯
3FGL J2000.0+6509	98.01	17.67	1ES 1959+650	0.047	bll	36.8 ± 2.3	3.6	<0.03	3.4	⋯
3FGL J2009.3−4849	350.39	−32.60	PKS 2005−489	0.071	BLL	13.8 ± 1.6	0.1	<0.03	1.7	⋯
3FGL J2158.8−3013	17.73	−52.24	PKS 2155−304	0.116	bll	78.1 ± 3.9	4.7	<0.03	2.1	⋯
3FGL J2202.7+4217	92.60	−10.45	BL Lacertae	0.069	BLL	15.3 ± 1.3	1.9	<0.04	6.7	⋯
3FGL J2250.1+3825	98.25	−18.56	B3 2247+381	0.119	bll	5.6 ± 1.0	0.6	<0.04	3.3	⋯
3FGL J2347.0+5142	112.89	−9.91	1ES 2344+514	0.044	bll	13.9 ± 1.4	0.0	<0.02	0.9	⋯
3FGL J2359.3−3038	12.82	−78.03	H 2356−309	0.165	bll	2.6 ± 0.7	0.0	<0.03	0.5	⋯

Note. The class column gives the class designator following the convention of the 3FGL: bll = BL Lac type of blazar, rdg = radio galaxy, FSRQ = flat spectrum radio quasar, bcu = active galaxy of uncertain type. As in the 3FGL, designations shown in capital letters are firm identifications; lower-case letters indicate associations. Energy flux is integrated from the spectral model between 10 GeV and 1 TeV.

2. *Non-variable HSPs.* In this sub-sample of the HSP sample, we further demand the variability index in the 3FGL to be smaller than 100, which corresponds to a significance of less than 4.2σ that the source flux is time-variable. This reduces the sample to 258 sources. Cascade photons can arrive with a significant time delay (Plaga 1995), and thus we exclude sources whose average flux might be dominated by strong flaring activity from which the cascade photons might not yet have reached Earth.
3. *Close-by HSPs with* $z < 0.2$. We also limit the first sample to close-by AGNs, as the cascade emission leads to a broader angular emission profile from closer sources (Ando & Kusenko 2010). This additional cut reduces the sample size to 72 objects.
4. *Extreme HSPs.* As a further subset of the HSP sample, we only consider extreme HSP (XHSPs) with $\nu_{\rm sync} > 10^{17}$ Hz that additionally show a large ratio of X-ray to radio flux, $F_X/F_R > 10^4$. The radio and X-ray fluxes are extracted from the 3LAC catalog. This criterion was identified in Bonnoli et al. (2015) as a promising tracer of sources that have a hard spectral index and thus are likely emitters of γ rays beyond multiple TeV. In total, there are 24 sources in this sample.

We also consider the same sample as in Chen et al. (2015a) (24 sources) and all TeV detected AGN listed in Biteau & Williams (2015) (38 sources).

Additionally, we define two control samples for which we do not expect to find any evidence for extension:

1. *Low synchrotron peak blazars (LSPs).* This control sample contains a subset of low synchrotron peak blazars (FSRQs, BL Lacs, and blazars of unknown type with $\nu_{\rm sync} < 10^{14}$ Hz) with $\nu_{\rm sync} < 10^{13}$ Hz. We infer from

Table 8
Analysis Results for Stacked Object Samples Testing Hypotheses of Extension and Halo Emission

Name	N_{obj}	TS_{ext}	R_{ext}(deg)	TS_{halo}	f_{halo} ($\Gamma_{halo} = 2$)		
					$R_{halo} = 0.^\circ1$	$R_{halo} = 0.^\circ316$	$R_{halo} = 1.^\circ0$
HSPs	300	30.5 (1.1)	$0.015 \pm 0.001 \pm 0.013$	0.0	<0.032	<0.005	<0.005
Non-Variable HSPs	258	24.3 (0.3)	$0.017 \pm 0.002 \pm 0.013$	2.0	<0.040	<0.006	<0.008
HSPs ($z < 0.2$)	72	15.6 (0.4)	$0.016 \pm 0.002 \pm 0.013$	2.2	<0.017	<0.006	<0.004
XHSPs	24	13.1 (0.1)	$0.018 \pm 0.003 \pm 0.014$	4.4	<0.063	<0.015	<0.009
Sample of Chen et al. (2015a)	24	0.6 (0.1)	<0.030	0.1	<0.043	<0.008	<0.013
TeV-Selected AGN	38	18.4 (0.7)	$0.015 \pm 0.002 \pm 0.013$	0.0	<0.040	<0.013	<0.010
LSPs	247	1.5 (0.2)	<0.040	1.8	<0.004	<0.008	<0.008
PSRs	88	26.3 (0.2)	$0.030 \pm 0.003 \pm 0.027$	3.8	<0.004	<0.004	<0.006

Note. The last two samples are control samples for which we do not expect to find any intrinsic extension. In the second column, N_{obj} denotes the number of sources in the sample. The value of TS_{ext} in parentheses is the minimum obtained with the two bracketing models of the PSF (see Section 2.3). Here, R_{ext} and R_{halo} are the best-fit intrinsic 68% containment radii obtained when fitting the sample with a Gaussian morphology and a Gaussian halo component, respectively. The R_{ext} column includes the statistical and systematic (IRF) errors. We provide 90% C.L. limits on the Halo flux ratio f_{Halo} because the halo is not detected in any sample. For easier comparison between the samples, the limits are provided for a fixed spectral index $\Gamma_{halo} = 2$ and different values of the halo extension.

predictions of the blazar sequence (Ghisellini et al. 2017) that such sources are unlikely to emit a significant amount of γ-rays at the highest energies. The sample consists of 246 sources.

2. *Pulsars.* As a second control sample, we consider a population of pulsars. We exclude the pulsars CTA1 and the Crab, for which we have identified the PWN as extended or possibly extended, as well as sources in the 3FGL with latitudes $|b| < 5^\circ$. This leaves us with 89 pulsars.

For each sample, we sum the likelihoods of individual sources, assuming common parameters for all sources. In the case of the extension hypothesis, the common parameter is R_{ext} and we use 2D Gaussian spatial profiles (no disks) for all sources. For the halo, the common parameters are R_{halo}, Γ_{halo}, and the ratio f_{halo} between the point source and halo energy flux integrated between 1 GeV and 1 TeV. We find the best-fit parameters for R_{ext} (R_{halo}, Γ_{halo}, and f_{halo}) for the extension (halo) hypothesis from the summed likelihoods. For the extension hypothesis, we repeat the procedure with the likelihoods obtained from the bracketing IRFs. In the case of a non-detection of extension or halo, we report upper limits on R_{ext} and f_{halo}, respectively. For the halo case, we do so by fixing $\Gamma_{halo} = 2$, which is the spectral shape generally expected for the cascade (e.g., Protheroe & Stanev 1993), and fixing R_{halo} to values of $0.^\circ1$, $0.^\circ316$, and $1.^\circ0$. Thus, we are left with one free parameter each for both extension and halo. We calculate one-sided 95% confidence limits on these quantities by stepping over them and profiling over the parameters of the other sources in the ROI until the summed likelihood changes by $2\Delta \ln \mathcal{L} = 2.71$.

We present the stacked TS values for a halo and extended emission for each sample in Table 8, along with the combined best-fit values of R_{ext} and the limit values for f_{Halo}, as well as the number of sources in each sample, N_{obj}.

We find the highest TS_{ext} values for the samples encompassing all HSPs and non-variable HSPs with best-fit values of $R_{ext} = 0.^\circ015 \pm 0.^\circ001 \pm 0.^\circ013$ and $R_{ext} = 0.^\circ017 \pm 0.^\circ002 \pm 0.^\circ013$, respectively. The second uncertainty represents half the difference between the best-fit values when the different bracketing PSFs are used to estimate the systematic uncertainty (cf. Section 2.3). The extension is found to be consistent with uncertainties in the PSF.[76] The interpretation is further supported by the fact that samples containing bright sources show larger TS_{ext} values. Indeed, the pulsar sample yields $TS_{ext} = 26.4$, indicating again that the high TS_{ext} value of the HSP sample is connected to the systematic uncertainty in the PSF modeling. In terms of a pair halo, the sources should not only be bright but also have a hard spectrum that extends well into the TeV range. However, the XHSP and TeV-selected AGN sample show lower TS_{ext} values than the "pure" HSP samples.

Similarly, we do not find any evidence for halo emission in any of the stacked samples. In contrast to the extension model, none of the control samples show evidence for a halo component. We did not compute systematic uncertainties in the halo case because—in contrast to the extension case—the likelihood depends on R_{halo} and Γ_{halo}, which would make it extremely computationally expensive. We expect these systematic effects to be subdominant in the halo-hypothesis case, compared to the statistical uncertainties. The reasons are the small flux of the halo component and the fact that most sources are located at high Galactic latitudes where uncertainties on the diffuse emission are less pronounced.

We cannot confirm the evidence for halo emission reported by Chen et al. (2015a). The stacked analysis for the low-redshift TeV blazars used in their sample results in the lowest values for TS_{ext} and TS_{halo} of all samples considered.

5. Limits on the Intergalactic Magnetic Field

With no clear evidence for an extension of individual blazars or stacked samples of BL Lac objects, we use the FHES to derive constraints on the coherence length, λ, and field strength, B, of the IGMF. We use both spectral and spatial information from the catalog, as well as spectra from imaging air Cherenkov telescopes (IACTs), to derive these constraints. A significant source detection at very high γ-ray energies with IACTs is essential for this study, in order to probe the intrinsic spectrum in the regime where it is strongly affected by EBL absorption.

[76] One should note, however, that the bracketing PSFs were derived by considering samples of blazars that were assumed to be pointlike; see https://fermi.gsfc.nasa.gov/ssc/data/analysis/LAT_caveats.html.

Table 9
Spectra from Ground-based Instruments Used in the IGMF Study Ordered by Increasing Redshift

Source	z	R.A. (deg)	Decl. (deg)	3FGL name	3FGL var. index	Experiment	Obs. Period	References
1ES 1312–423	0.105	198.76	−42.61	J1314.7-4237	45.0	H.E.S.S.	2004-2010	(1)
RGB J0710+591	0.125	107.63	59.14	J0710.3+5908	55.5	VERITAS	2008-2009	(2)
1ES 0229+200	0.14	38.20	20.29	J0232.8+2016	49.2	H.E.S.S.	2005-2006	(3)
						VERITAS	2009-2012	(4)
1RXS J101015.9–311909	0.143	152.57	−31.32	J1010.2-3120	86.3	H.E.S.S.	2006-2010	(5)
						VERITAS	2009-2012	(6)
H 2356–309	0.165	359.78	−30.63	J2359.3-3038	41.0	H.E.S.S.	2004	(7)
						H.E.S.S.	2005	(8)
						H.E.S.S.	2006	(9)
1ES 1218+304	0.182	185.34	30.18	J1221.3+3010	92.5	VERITAS	2007	(10)
						VERITAS	2008-2009	(11)
1ES 1101–232	0.186	165.91	−23.49	J1103.5-2329	36.5	H.E.S.S.	2004-2005	(12)
1ES 0347–121	0.185	57.35	−11.99	J0349.2-1158	44.3	H.E.S.S.	2006	(13)
1ES 0414+009	0.287	64.22	1.09	J0416.8+0104	55.8	H.E.S.S.	2005-2009	(14)
						VERITAS	2008-2011	(15)

Note. From left to right: source name, redshift, right ascension and declination (J2000), name of the source, variability index from the 3FGL catalog, experiment, observation period, and reference for the VHE spectra.
References. (1) Abramowski et al. (2013), (2) Acciari et al. (2010b), (3) Aharonian et al. (2007b), (4) Aliu et al. (2014), (5) Abramowski et al. (2012b), (6) Aliu et al. (2014), (7) Abramowski et al. (2010), (8) Abramowski et al. (2010), (9) Abramowski et al. (2010), (10) Acciari et al. (2009), (11) Acciari et al. (2010a), (12) Aharonian et al. (2007c), (13) Aharonian et al. (2007a), (14) Abramowski et al. (2012a), (15) Aliu et al. (2012).

5.1. Source Selection

We again use the list of VHE-emitting sources compiled in Biteau & Williams (2015) to select sources detected both with the *Fermi* LAT and IACTs. We set aside five objects with uncertain redshifts: S5 0716+714, 3C 66A, PKS 0447-439, PG 1553+113, and PKS 1424+240. We further limit the sample to IACT spectra with a well-measured EBL cutoff, i.e., significant spectral points up to an optical depth $\tau > 2$, assuming the EBL model of Domínguez et al. (2011). In this way, we guarantee that we have sufficient statistics in the very high energy part of the spectra, which is most important to model the contribution from the cascade. Moreover, we exclude sources that show evidence for variability beyond the 4.2σ level, corresponding to a variability index larger than 100 in the 3FGL catalog. In this way, we also exclude sources whose flux level is dominated by flaring events and whose quiescent state is much lower than the average flux level. In the case that the same emission mechanism is responsible for γ-rays at energies probed with the *Fermi* LAT and IACTs, this cut implies that the IACT spectra are also a good representation for the average flux level. We further discard H 1426+428, because the *Fermi*-LAT measurement does not match that recorded with HEGRA during their 2000 observation, which implies that the source was in a different emission state in the past. We note that the HEGRA Collaboration reported two spectra for H 1426+428, one corresponding to observations in 1999-2000 and one to observations in 2002 (Aharonian et al. 2003). These two spectra show a flux mismatch by a factor of 2.5, similar to that observed in X-rays, indicative of source variability. H 1426+428 has been detected again with VERITAS (Archambault et al. 2017b), but the spectrum is not yet published.

This selection leaves us with nine BL Lac objects, for which we have 15 IACT spectra for the IGMF analysis, as shown in Table 9. All objects listed in this table are high frequency peak blazars with redshifts ranging from 0.105 to 0.287. Most of these sources have already been used in the past to set constraints on the IGMF (e.g., Neronov & Vovk 2010; Dermer et al. 2011; Tavecchio et al. 2011; Taylor et al. 2011; Abramowski et al. 2014; Arlen et al. 2014; Finke et al. 2015).

5.2. Modeling of the Cascade Emission

In order to model the expected cascade emission from these sources, we generate a library of cascade templates for different IGMF configurations using the ELMAG Monte Carlo code (Kachelrieß et al. 2012). This open-source code computes the observed photon flux (primary and cascade photons) by sampling an input intrinsic γ-ray spectrum of a source assumed to be viewed on-axis, i.e., $\theta_{\rm obs} = 0°$, using a weighted sampling procedure (see Kachelrieß et al. 2012, for details). Interactions with the CMB and EBL are taken into account, and we choose to trace all secondary particles with an energy $\epsilon \geqslant \epsilon_{\rm thr}$, where $\epsilon_{\rm thr} = 100$ MeV. Energy losses due to inverse-Compton scattering and synchrotron radiation are integrated out for $\epsilon < \epsilon_{\rm thr}$. The energy ϵ, observation angle ϑ, and time delay Δt for the final γ-rays reaching the observer are recorded in a multidimensional histogram.

ELMAG adopts a simplified description of the IGMF, namely that its field strength is constant in cells that have a size equal to the coherence length. The e^+e^- pairs are deflected in a coherent manner in each cell. ELMAG uses the small-angle approximation (see Kachelrieß et al. (2012) for details), i.e., the total deflection angle β can be accumulated following a random-walk approximation, such that the emission angle α is related to the observation angle ϑ through $\alpha = \beta - \vartheta$ (see Figure 1 in Dolag et al. (2009)). If the total squared deflection angle exceeds $\pi^2/4$, the deflection angle β of the cascade photons is randomized. This occurs when (Neronov & Semikoz 2009; Meyer et al. 2012)

$$B/G \gtrsim \begin{cases} 2 \times 10^{-15}(1+z_r)^4(\epsilon/\mathrm{GeV}) & \lambda \gg 1\ \mathrm{kpc}, \\ 8 \times 10^{-15}(1+z_r)^4(\epsilon/\mathrm{GeV})^{3/4}(\lambda/\mathrm{kpc})^{-1/2} & \lambda \lesssim\ \mathrm{kpc}, \end{cases} \quad (8)$$

where B is the IGMF strength at $z = 0$, and z_r is the redshift where the pair production takes place, producing secondary γ rays of energy ϵ. We note that this formula includes the $(1 + z)^3$ dependence of the IGMF, which is neglected in the ELMAG implementation used here. Importantly, if $\beta - \vartheta > \theta_{\rm jet}$, where $\theta_{\rm jet}$ is the jet opening angle, the small-angle approximation breaks down and the photon is dismissed. Taking $\epsilon = 1$ GeV and $z_r \approx z$, more and more photons are randomized—and consequently, are likely to be dismissed for deflection angles larger than $\theta_{\rm jet}$ for magnetic fields larger than $\sim 10^{-15}$ G. Because $\theta_{\rm obs} = 0^\circ$ is assumed, the simulated cascades are symmetric in surface brightness and do not show the elongated features seen in 3D Monte Carlo simulations (Neronov et al. 2010). As shown by Arlen et al. (2014), an increasing viewing angle should increase the cascade contribution if the observed point-source spectrum is held constant. The rejection of high-angle photons is thus expected to yield conservative results.

We simulate the full cascade flux over a grid of redshifts and in bins of injected γ-ray energy ΔE between 100 MeV and 32 TeV (using eight bins per decade) using the EBL model of Domínguez et al. (2011). In each injected energy bin, we assume a power-law intrinsic spectrum with index $\Gamma_{\rm int} = 2$. We use an (8×8) logarithmic grid over the magnetic field and coherence length with $B/G \in [10^{-20}; 10^{-12}]$ and $\lambda/{\rm Mpc} \in [10^{-4}; 10^{4}]$. We thereby probe IGMF values for which hints have been claimed (Chen et al. 2015a, 2015b) and that are in a relevant range for astrophysical or primordial generation of the IGMF (Durrer & Neronov 2013). We also study different jet opening angles $\theta_{\rm jet} = 1^\circ, 3^\circ, 6^\circ, 10^\circ$. The corresponding bulk Lorentz factors for a conical jet, $\Gamma_L = \theta_{\rm jet}^{-1} \sim 60, 20, 10, 6$, are broadly consistent with typical values inferred from broadband emission modeling of AGN. We assume that the sources have been active for a particular time $t_{\rm max}$ and all cascade photons arriving with a time delay $\Delta t > t_{\rm max}$ are discarded. We test $t_{\rm max} = 10, 10^4, 10^7$ years, where the first case corresponds to the conservative case in which blazars have only been active during a timescale comparable to the observation time with the *Fermi* LAT. AGN activity times are nonetheless estimated to lie between 10^6 and 10^8 years (Parma et al. 2002), which is reflected by the maximum $t_{\rm max}$ value tested, whereas $t_{\rm max} = 10^4$ years is our choice for an intermediate case.

In this way, we end up with a multidimensional cube for the cascade flux $dN/d\epsilon\, d\Omega$ (in units per energy and per solid angle) in bins of observed energy ϵ, of observation angle ϑ that corresponds to the solid angle Ω, and of injected energy E for a source at redshift z with parameters $\mathcal{S} = (\theta_{\rm jet}, t_{\rm max})$ and IGMF parameters $\mathcal{B} = (B, \lambda)$. We simulate $N_{{\rm inj},j}$ photons and calculate the yield y_j of cascade flux per injected particle for narrow bins of injected energy ΔE_j,

$$y_j(\epsilon, \vartheta; z, \mathcal{S}, \mathcal{B}) = \frac{1}{N_{{\rm inj},j}} \frac{dN}{d\epsilon\, d\Omega}(\epsilon, \vartheta; E_j, z, \mathcal{S}, \mathcal{B}), \quad (9)$$

where E_j denotes the central energy of ΔE_j.[77] We obtain the cascade energy flux per solid angle in an observed energy bin $\Delta\epsilon_i$ for an arbitrary injected γ-ray spectrum $\phi(E, \boldsymbol{p})$ with parameters $\boldsymbol{p}$ by reweighting the yields y_j with a weight w_j and summing the cascade flux over all injected energy bins j,

$$F_i(\vartheta; z, \mathcal{B}, \mathcal{S}, \boldsymbol{p}) = \Delta\epsilon_i \sum_j w_j(\boldsymbol{p}) y_j(\epsilon, \vartheta; z, \mathcal{B}, \mathcal{S}), \quad (10)$$

where ϵ lies within the ith observed energy bin and the weights are given by

$$w_j(\boldsymbol{p}) = \int_{\Delta E_j} dE\ \phi(E, \boldsymbol{p}). \quad (11)$$

The final cascade flux $F_{{\rm casc},i}$ in the observed energy bin $\Delta\epsilon_i$ (the same energy binning is used as in Section 2) is then obtained by integrating over the entire solid angle filled by the cascade, $\Omega_{\rm casc}$:

$$F_{{\rm casc},i}(z, \mathcal{B}, \mathcal{S}, \boldsymbol{p}) = \int_{\Omega_{\rm casc}} F_i(\vartheta; z, \mathcal{B}, \mathcal{S}, \boldsymbol{p}) d\Omega. \quad (12)$$

The dependence of $F_{{\rm casc},i}$ on $\boldsymbol{p}$ is introduced through the weights w_j. Additionally, the 68% containment radius $R_{{\rm casc},i}(z, \mathcal{B}, \mathcal{S}, \boldsymbol{p})$ of the cascade is given through the relation

$$0.68 = \frac{2\pi}{F_{{\rm casc},i}} \int_0^{R_{{\rm casc},i}} F_i(\vartheta; z, \mathcal{B}, \mathcal{S}, \boldsymbol{p}) \sin\vartheta d\vartheta. \quad (13)$$

Note that $R_{{\rm casc},i}$ is, in general, also a function of observed energy, as well as the source and IGMF parameters.

5.3. IGMF Constraints

With the simulated cascades in hand, we are in a position to compare the theoretical cascade spectra and their spatial extension versus the results of the extended catalog for the case of a source with a halo. For the analysis, we make the following assumptions in addition to those made when calculating the cascade flux F (discussed in the previous section):

1. The source flux does not vary over the observation time and the IACT spectra are good representatives of the average flux level of the sources.
2. The intrinsic spectrum for each source over the whole *Fermi*-LAT and IACT energy range can be parameterized with a single LP function with exponential cutoff. The observed spectrum is then obtained by multiplying the intrinsic spectrum by the EBL absorption, which is parameterized through $\exp(-\tau(E, z))$, where $\tau(E, z)$ is the optical depth, which we assume to follow the model of Domínguez et al. (2011). The optical depth is a function of primary γ-ray energy and source redshift and is given by the same EBL model that we use for the ELMAG simulation. The observed spectrum is then given by the function
$$\phi_{\rm obs}(E, \boldsymbol{p}, z) = N(E/E_0)^{-(\alpha + \beta \ln(E/E_0))} \times \exp[-(E/E_{\rm cut} + \tau(E, z))], \quad (14)$$
which has four free fit parameters, $\boldsymbol{p} = (N_0, \alpha, \beta, E_{\rm cut})$. We only assume concave spectra, i.e., $\beta \geqslant 0$ and set $E_0 = 1$ TeV throughout. Enforcing $\beta \geqslant 0$ should lead to conservative results for the cascade contribution, as it will decrease the intrinsic source flux at high energies.
3. Accounting for the cascade contribution does not change the best-fit spectrum of the central point source in the

[77] The number of injected particles is given by the sum over the initial Monte Carlo weights calculated by ELMAG in the jth energy bin. We inject 600 particles for each energy bin. For $2 \leqslant \tau < 4$, we increase the number of particles by a factor of $w_{{\rm init},j} = \lfloor \tau \rfloor$. For $\tau \geqslant 4$, we increase the number by a factor of 4. The initial Monte Carlo weights are adjusted accordingly by $w_{{\rm init},j}^{-1}$.

entire *Fermi*-LAT energy band by more than 5σ (see Section 2.5).

4. In each energy bin i, the spatial morphology of the cascade can be approximated using a 2D Gaussian halo component with a 68% containment radius equal to that of the cascade, i.e., $R_{\mathrm{halo},i} = R_{\mathrm{casc},i}$.
5. The cascade is not suppressed by the dissipation of energy of the e^+e^- beam into plasma instabilities (the efficiency of these instabilities is a matter of ongoing debate; see, e.g., Broderick et al. (2012); Sironi & Giannios (2014); Menzler & Schlickeiser (2015); and Chang et al. (2016)).

Given these assumptions, we can use the computed source likelihoods of the extended source catalog to constrain the IGMF parameters. The extraction of the likelihoods is described in Section 2.5. We use the SED likelihoods for the halo, $\mathcal{L}_{\mathrm{halo},i}(F_{\mathrm{halo}}, R_{\mathrm{halo}}) \equiv \mathcal{L}_{\mathrm{halo},i}(F_{\mathrm{halo}}, R_{\mathrm{halo}}; \hat{\boldsymbol{\theta}}|\boldsymbol{D})$ (given in the `halo_sed_dloglike` column in the catalog fits file, see Appendix B), which are provided as a function of the halo flux F_{halo}, the 68% containment radius R_{halo}, for each observed energy bin $\Delta\epsilon_i$. Here, $\boldsymbol{D}$ denotes the data from the considered source, with the parameters $\boldsymbol{\theta}$ of the other sources in the ROI having already been profiled over.

The likelihood for a cascade with flux $F_{\mathrm{casc},i}$ (calculated through Equation (12)) and containment radius $R_{\mathrm{casc},i}$ is then simply given by

$$\mathcal{L}_{\mathrm{casc}}(z, \mathcal{B}, \mathcal{S}, \boldsymbol{p}) = \prod_i \mathcal{L}_{\mathrm{halo},i}(F_{\mathrm{casc},i}(z, \mathcal{B}, \mathcal{S}, \boldsymbol{p}), \times R_{\mathrm{casc},i}(z, \mathcal{B}, \mathcal{S}, \boldsymbol{p})). \quad (15)$$

The catalog also provides the likelihood for the central point source in each energy bin, $\mathcal{L}_{\mathrm{src},i}(\phi(E_i, \boldsymbol{p}, z)) \equiv \mathcal{L}_{\mathrm{src},i}(\phi(E_i, \boldsymbol{p}, z); \hat{\boldsymbol{\theta}}|\boldsymbol{D})$ (in the `src_sed_dloglike` column in the catalog fits file; see Appendix B). For the likelihood of the IACT spectrum, $\mathcal{L}_{\mathrm{IACT}}(\phi(E_i, \boldsymbol{p}, z)) \equiv \mathcal{L}_{\mathrm{IACT}}(\phi(E_i, \boldsymbol{p}, z)|\boldsymbol{D}_{\mathrm{IACT}})$, we assume a normal distribution centered on the reported flux and a width equal to the flux uncertainty of the measured IACT spectrum ($\boldsymbol{D}_{\mathrm{IACT}}$). We neglect any contribution of the reprocessed cascade flux to the IACT spectrum, which is generally well-justified, given the source spectra and IGMF parameters under consideration. In the case that multiple IACT spectra are available for the same source (cf. Table 9), we test whether the observed spectra are compatible with one another by fitting them with a simple power law. For sources where this is the case within 2σ statistical uncertainties, we use all the IACT data points simultaneously (1ES 0229+200, 1ES 1218+304, H 2356–309, 1ES 0414+009).

In order to find the best-fit intrinsic parameters $\boldsymbol{p}$ for a given IGMF and source, we maximize the product of the cascade and point source likelihoods,

$$\mathcal{L}(z, \mathcal{B}, \mathcal{S}, \boldsymbol{p}) = \mathcal{L}_{\mathrm{casc}}(z, \mathcal{B}, \mathcal{S}, \boldsymbol{p}) \times \left(\prod_i \mathcal{L}_{\mathrm{src},i}(\phi_{\mathrm{obs}}(E_i, \boldsymbol{p}, z))\right) \times \left(\prod_j \mathcal{L}_{\mathrm{IACT},j}(\phi(E_j, \boldsymbol{p}, z))\right). \quad (16)$$

As an example, we show the best-fit spectrum and cascade contribution for various magnetic-field strengths in the left panel of Figure 16 for 1ES 1101–232. In this example, we have assumed that the source has been active for $t_{\mathrm{max}} = 10^7$ years. This maximum value of t_{max} yields the largest cascade contribution, and the differences in the fit for the different IGMF values are most pronounced. As the magnetic field decreases, the contribution from the cascade becomes larger at lower energies. To compensate for this, the fit of the intrinsic spectrum (dotted lines) prefers lower values of the cutoff energy, E_{cut}. For high B-field values, the fit is insensitive to the cutoff at the highest energies. In the right panel of Figure 16, we show the containment radii R_{casc} and the 68% containment radius for the *Fermi*-LAT PSF for the event class PSF3. Only for the largest tested IGMF strengths does the halo size increase beyond the PSF. For $B \lesssim 10^{-16}$ G, the halo appears point-like over the entire *Fermi*-LAT energy range. For this reason, the constraints are driven primarily by spectral features of the cascade. We show the same figure for the other considered blazars in Appendix A for the minimum and maximum considered activity times, along with the best-fit parameters of the sources yielding constraints on the IGMF.

For each tested IGMF realization and selected source (fixing z and $\mathcal{S}$), we maximize the likelihood of Equation (16) by profiling over the intrinsic spectral parameters $\boldsymbol{p}$. We then calculate the likelihood ratio test statistic:

$$\mathrm{TS}(B, \lambda) = -2\ln\left(\frac{\mathcal{L}(B, \lambda, \hat{\boldsymbol{p}}(B, \lambda))}{\mathcal{L}(\hat{\hat{B}}, \hat{\hat{\lambda}})}\right). \quad (17)$$

In the numerator, $\hat{\boldsymbol{p}}$ denotes the best-fit nuisance parameters for fixed values of (B, λ), and the denominator gives the unconditionally maximized likelihood with maximum likelihood estimators $\hat{\hat{B}}$ and $\hat{\hat{\lambda}}$.

For all tested sources, we find that the best-fit parameters $\hat{\hat{B}}$ and $\hat{\hat{\lambda}}$ coincide with IGMF parameters that lead to a strong deflection of the e^+e^- pairs and a consequent suppression of the cascade flux. We therefore derive 95% confidence lower limits on the IGMF by excluding parameters for which $\mathrm{TS}(B, \lambda) \geqslant 5.99$, corresponding to a χ^2 distribution with two degrees of freedom (B-field strength and coherence length). The limits for the individual sources are shown in the left panel of Figure 17 for $\theta_{\mathrm{jet}} = 6^\circ$ and a conservative choice of $t_{\mathrm{max}} = 10$ years.

Clearly, a number of spectra yield strong constraints and the lower limit of the IGMF lies between 10^{-17} G and 10^{-16} G. These constraints are driven by the $\mathcal{L}_{\mathrm{casc}}$ term in Equation (16), as it gives the largest contribution to the $\mathrm{TS}(B, \lambda)$ values. The strongest constraints come from the observations of 1ES 0229+200, as well as the H.E.S.S. observations of 1ES 0347–121, H 2356–309, and 1ES 1101–232. The non-monotonic behavior of the limits of H 2356–309 can be explained by the fit stability, particularly the best-fit value for E_{cut}. Less than 5% of the tested parameter space is excluded for the combined VERITAS and H.E.S.S. spectrum of 1ES 0414+009, as well as for 1ES 1312–423 and RGB 0710+591, and we do not show those results here.

We derive combined limits on the IGMF by stacking the individual IGMF likelihoods of the individual sources. We consider only the six sources that yield strong constraints by themselves. The results for different choices of t_{max} are shown in the right panel of Figure 17.[78] Even for the most

[78] The limits on the IGMF are available in plain ASCII files at http://www-glast.stanford.edu/pub_data/1261/ and https://zenodo.org/record/1324474.

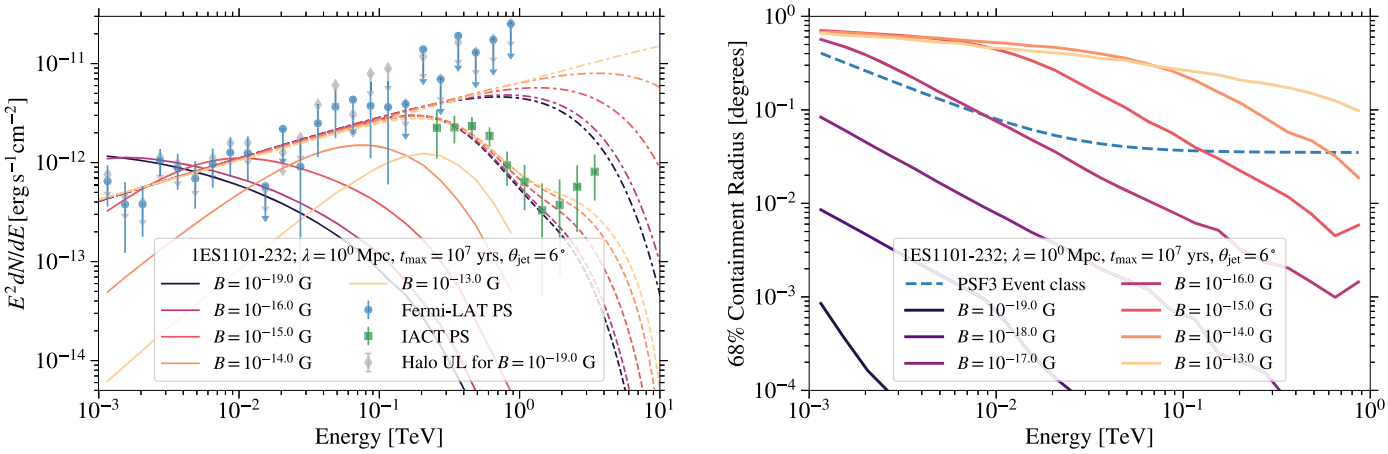

Figure 16. Left: fit of the intrinsic spectrum and cascade component to the IACT and *Fermi*-LAT data of 1ES 1101–232 ($z = 0.186$) for different IGMF strengths. A source activity time of $t_{max} = 10^7$ years and a jet opening angle of $\theta_{jet} = 6°$ are assumed, along with a coherence length of 1 Mpc. The best-fit intrinsic spectra multiplied with EBL absorption are shown as dashed lines with colors matching those of the cascade component (solid lines). The intrinsic spectra are shown as dash-dotted lines. Upper limits on the halo energy flux for widths equal to that of the cascade for $B = 10^{-19}$ G are shown as gray diamonds. Right: containment radii for the cascade (R_{casc}) for different B-field strengths and the PSF (PSF3 event class) as a function of energy for the same source and parameters as the right panel. We show the containment radii for two additional B-field strengths (10^{-18} G and 10^{-17} G) compared to the left panel to better illustrate the IGMF dependence on this quantity. The spectra for these values of B would be very similar to the ones shown for 10^{-19} G or 10^{-16} G.

conservative case of $t_{max} = 10$ years, we are able to exclude magnetic fields below $\sim 3 \times 10^{-16}$ G for $\lambda > 10^{-2}$ Mpc. If we additionally exclude the sources 1ES 1218+304 and 1ES 0229-200, for which evidence for variability has been found (Aliu et al. 2014), the limits weaken only marginally for short activity times—but by almost a factor of 5 for $t_{max} = 10^7$ years (solid lines in the right panel of Figure 17). For such long activity times, the limits improve by three orders of magnitude compared to $t_{max} = 10$ years, limiting the B field to be above 3×10^{-13} G. For such high B fields, however, one can see from Equation (8) that the small angle approximation adopted by ELMAG breaks down, as indicated by the blue dashed line for cascade photons of $\epsilon = 1$ GeV. Due to the fact that ELMAG randomizes the deflection angles for large deflections and discards the photons when $\beta > \theta_{jet}$, the results for long activity times also depend on the assumed opening angle. Assuming $\theta_{jet} = 1°$ instead of $\theta_{jet} = 6°$ decreases the limits by a factor of $1/2$, as more photons are discarded. For $\theta_{jet} = 10°$, the results are comparable to $\theta_{jet} = 6°$.This effect is not observed for $t_{max} = 10$ years where the limits are independent of θ_{jet}.

We do not test the impact of different EBL models, as we expect the difference in the limits to be negligible. This has been shown in a sensitivity study by Meyer et al. (2016) for the Cherenkov Telescope Array (CTA) that also utilized the ELMAG code and compared results for the EBL model of Domínguez et al. (2011) and Finke et al. (2010). The slightly larger photon density of the Finke et al. model gives rise to more electron-positron pairs, estimated to be on the order of 5%, when comparing the two EBL models above (Meyer et al. 2016). The resulting difference of the limits should consequently be small, compared to the effect of the uncertain blazar activity timescales.

A larger impact on the limits is given by the systematic uncertainty of the energy scale of IACTs. This is commonly assumed to be on the order of ±15%, but a cross-calibration between the *Fermi* LAT and IACTs, using the spectrum of the Crab Nebula, found the uncertainty to be on the order of 5% (Meyer et al. 2010). Nevertheless, recalculating the limits for $\theta_{jet} = 6°$ and $t_{max} = 10$ years with a rescaling of the IACT energy scale by +15% and −15% results in $B \gtrsim 4 \times 10^{-16}$ G and $B \gtrsim 10^{-16}$ G, respectively, for $\lambda > 10^{-2}$ Mpc.

5.4. Discussion of IGMF Constraints

Even for the extremely conservative choice of $t_{max} = 10$ years, our results limit the IGMF to be larger than 3×10^{-16} G for $\lambda \gtrsim 10^{-2}$ Mpc. Therefore, our results improve the limits derived by Finke et al. (2015) by more than three orders of magnitude, even though we have used a similar source sample and assumptions (Finke et al. 2015 tested $t_{max} = 3$ years and a maximum primary γ-ray energy equal to the highest-energy data point of the IACT spectrum). One major difference is that Finke et al. (2015) use a semi-analytic calculation of the cascade (Dermer et al. 2011; Meyer et al. 2012) that only considers the first generation of the cascade. Repeating our analysis using the semi-analytic model in Meyer et al. (2012), our limits weaken by a factor of five. The remaining differences can be explained by the very different analysis techniques used. In the present analysis, we simultaneously fit the intrinsic spectrum and the cascade contribution to the data, profiting from the results of the FHES derived in bins of energy. In contrast to that, Finke et al. (2015) exclude IGMF models that lead to an integrated cascade flux larger than the measured flux between 0.1 and 300 GeV. Therefore, the present analysis uses more information (spectral and spatial) and is consequently more sensitive to the cascade emission.

In contrast to Arlen et al. (2014), we are able to rule out $B = 0$ with high significance. As noted in Finke et al. (2015), Arlen et al. (2014) use EBL models with low photon densities, partly incompatible with lower limits on the EBL from galaxy number counts. More importantly, they allow for a spectral break at lower γ-ray energies and very hard spectral indices below a few tens of GeV. As a result, the point-source flux at these energies is strongly suppressed and the entire GeV flux is dominated by the cascade. Such extreme assumptions are in

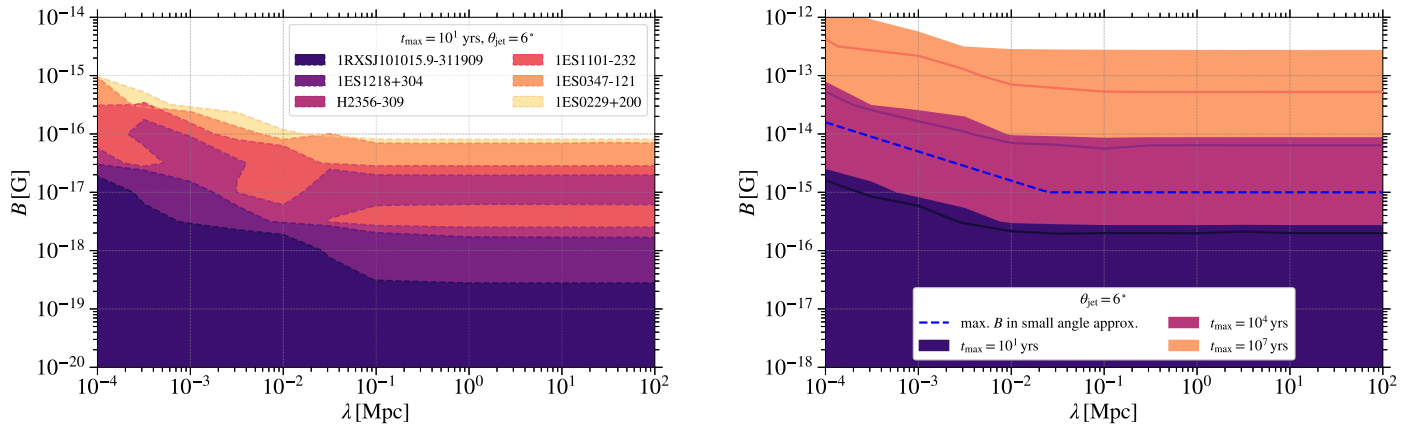

Figure 17. Ninety-five percent lower limits on the field strength of the IGMF for $\theta_{jet} = 6°$. Left: exclusions for $t_{max} = 10$ years for individual sources. Right: combined exclusion limits for different blazar activity times. The solid lines indicate the combined limits if the sources 1ES 0229+200 and 1ES 1218+304 are excluded from the sample. Above the blue dashed line, the small angle approximation adopted by ELMAG breaks down for an increasing number of cascade photons (cf. Equation (8), where an energy of 1 GeV has been assumed for the cascade photons).

tension with the assumption adopted here that the spectral parameters of the point sources are allowed to vary from the broadband energy fit by a maximum of 5σ in each energy bin. However, we do allow for curvature in the spectra by using a log-parabola in addition to the exponential cutoff. As can be seen from Figures 16, 18, and 19, large values of β are not preferred.

Under the assumption that the considered blazars have been active for more than 10 years, our limits agree with the values found in a recent study by the VERITAS collaboration (Archambault et al. 2017b). That study places a lower limit on the IGMF strength, which lies between $\sim 5 \times 10^{-15}$ and $\sim 7 \times 10^{-14}$ G (for coherence lengths larger than the inverse-Compton cooling length) due to the absence of a broadening of the angular distribution of γ-rays from the source 1ES 1218+304. The limits also agree with H.E.S.S. measurements from PKS 2155–305 that ruled out IGMF strengths of (0.3–3) $\times 10^{-15}$ G for $\lambda = 1$ Mpc (Abramowski et al. 2014). Both of these studies assumed blazar activity times long enough for the pair halo to be observable with IACTs.

For an activity time $t > 10^4$ years, our analysis also excludes B field values suggested in Chen et al. (2015b), where hints for a helical IGMF were found from correlations of arrival directions of diffuse γ-rays. It should be noted, however, that the cascade flux and spatial extension depend on the helicity of the IGMF, which is not included in the ELMAG 1D simulation (Alves Batista et al. 2016). We cannot confirm hints for pair halos as found in Chen et al. (2015a) with our stacking analysis nor with our dedicated IGMF analysis, which rules out the values suggested therein. Likely reasons for this discrepancy are the use of the updated `Pass 8` instrumental response and the usage of the dedicated PSF event classes in the present analysis (cf. Section 2). Furthermore, we run dedicated source-finding algorithms, providing a complete modeling of each ROI, while the analysis in Chen et al. (2015a) relied on the two-year LAT point source catalog.

The obtained limits are on the same order of magnitude as the projected exclusion limits for the future CTA presented in Meyer et al. (2016), which, however, only took the spectral features of the cascade into account and only used simulated observations from four blazars.

6. Conclusions

We have presented the first *Fermi* catalog of high-latitude ($|b| > 5°$) extended sources (FHES) for energies between 1 GeV and 1 TeV. Using the improved `Pass 8` event reconstruction and data analysis, we are able to identify 24 extended sources, 19 of which are identified as such for the first time.

We are able to associate 5 of the 19 new sources with counterparts from multiwavelength catalogs. We identify two SNRs (SNR G119.5+10.2 and SNR G332.5−05.6) and emission beyond the *WMAP* template in the radio lobes of Cen A. We also find evidence for extension of $R_{ext} = 0.^\circ030 \pm 0.^\circ003 \pm 0.^\circ007$ from the Crab Nebula. Even though the detection is not significant when systematic uncertainties of the PSF are taken into account, it should be noted that the measured extension agrees well with predictions from synchrotron self-Compton emission scenarios and is not observed in blazars with a similar flux above 10 GeV (Mkn 421, PG 1553+113, and PKS 2155−304). It is also in accordance with the extension recently reported by the H.E.S.S. collaboration (Holler et al. 2017). Furthermore, we have found evidence for extended γ-ray emission toward three SFRs (NGC 7822, NGC 1579, and IC 1396). However, NGC 7822 and NGC 1579 have been identified as spurious via limitations in the IEM. IC 1396 remains as a tentative association.

Three of the five unassociated newly discovered extended sources have hard spectra with $\Gamma \lesssim 2$, suggesting an association with an SNR or PWN. However, our search for radio, X-ray, or TeV counterparts in archival data was inconclusive. Among these objects, we identify FHES J1723.5−0501 and FHES J1741.6−3917 as the two most promising SNR candidates. Follow-up observations at other wavelengths are encouraged in order to identify the origin of the γ-ray emission.

None of the newly discovered extended sources are located at a Galactic latitude $|b| > 20°$, and the only extragalactic sources reported here have been previously identified as extended (including M 31, Fornax A, and the Cen A lobes). After correcting for trials, we do not find evidence of extended emission in high-latitude sources whether considered individually or as a population. This is also true for the sample of 38 IACT-detected blazars in the sample of Biteau & Williams (2015). Among the sources in this sample, PKS 1510−08

shows the strongest evidence for halo emission ($TS_{halo} = 9.4$), which corresponds to a local significance of 2.6σ. However, in this case, the model including a halo is only marginally preferred over the model with an additional point source in the ROI. The rather large TS values found for extension in stacked source samples of high-synchrotron peaked BL Lac objects are consistent with systematic uncertainties in the PSF. None of the unassociated sources above $|b| > 20^{\circ}$ show evidence for extension, and we cannot confirm the DM sub-halo interpretation of two 3FGL sources (Bertoni et al. 2016; Xia et al. 2017).

Using the results of the extended source catalog, we are able to derive strong limits on the IGMF, limiting $B \gtrsim 3 \times 10^{-16}$ G for $\lambda \gtrsim 10$ kpc, for a conservative assumption of the activity time of the considered blazars of 10 years. The modeling of the extension performed here makes the results more conservative, as we did not assume that the cascade emission is point-like. Compared to previous studies of the IGMF, our analysis uses both spatial and spectral information in the *Fermi*-LAT energy range and simultaneously fits the intrinsic source spectrum and cascade contribution. Even though the constraints are driven mostly by the spectral features caused by the cascade, the detection of pair halos remains a "smoking gun" signature of the IGMF that can only be addressed with a full modeling of the spectrum and the spatial source morphology. Using longer activity times of 10^4 (10^7) years improves the limits to $B \gtrsim 9 \times 10^{-15}$ G ($B \gtrsim 3 \times 10^{-13}$ G). For such large fields, however, the actual jet opening and viewing angle of the blazar become important to accurately model the halo. The influence of these effects in the limit of large field strength ($B \gtrsim 10^{-15}$ G) is not considered in the simplified 1D Monte-Carlo calculation used by ELMAG.

In the future, dedicated 3D Monte Carlo codes should be to search for the cascade emission at higher values of the IGMF, in order to accurately model the source extension and take into account the viewing angle of the blazar (Neronov et al. 2010; Alves Batista et al. 2016; Fitoussi et al. 2017). Such an analysis should also re-examine our assumption that the point-source spectrum does not change by more than 5σ when the halo component is derived. Further extensions could include more realistic models of the intergalactic field, including a full treatment of its turbulence spectrum (Caprini & Gabici 2015) and its helicity (Chen et al. 2015).

The authors would like to thank Ievgen Vovk for helpful discussions and Gloria Dubner for providing the VLA high resolution map of the Crab Nebula. The *Fermi*-LAT Collaboration acknowledges generous ongoing support from a number of agencies and institutes that have supported both the development and the operation of the LAT as well as scientific data analysis. These include: the National Aeronautics and Space Administration and the Department of Energy in the United States; the Commissariat à l'Energie Atomique and the Centre National de la Recherche Scientifique/Institut National de Physique Nucléaire et de Physique des Particules in France; the Agenzia Spaziale Italiana and the Istituto Nazionale di Fisica Nucleare in Italy; the Ministry of Education, Culture, Sports, Science, and Technology (MEXT), the High Energy Accelerator Research Organization (KEK), and the Japan Aerospace Exploration Agency (JAXA) in Japan; and the K. A. Wallenberg Foundation, the Swedish Research Council, and the Swedish National Space Board in Sweden.

Additional support for science analysis during the operations phase is gratefully acknowledged from the Istituto Nazionale di Astrofisica in Italy and the Centre National d'Études Spatiales in France. This work performed in part under DOE Contract DE-AC02-76SF00515.

This research has made use of the SIMBAD database, operated at CDS, Strasbourg, France and the NASA/IPAC Extragalactic Database (NED), which is operated by the Jet Propulsion Laboratory, California Institute of Technology, under contract with the National Aeronautics and Space Administration.

Software: ELMAG (Kachelrieß et al. 2012), fermipy (version 00-15-01, Wood et al. 2017).

Appendix A
Blazar Spectra for IGMF Constraints

In Figures 18 and 19, we show all blazar spectra obtained with *Fermi* LAT and IACTs that yield constraints on the IGMF as described in Section 5.3. We show the two extreme cases for the assumed activity time, $t_{max} = 10$ years and 10^7 years. For larger magnetic fields, it is obvious that the cascade flux is increased for the larger values of t_{max}. For 1ES 0229+200, 1ES 1218+304, and H 2356–309, the IACT spectra are fitted simultaneously, as they are not significantly different from each other.

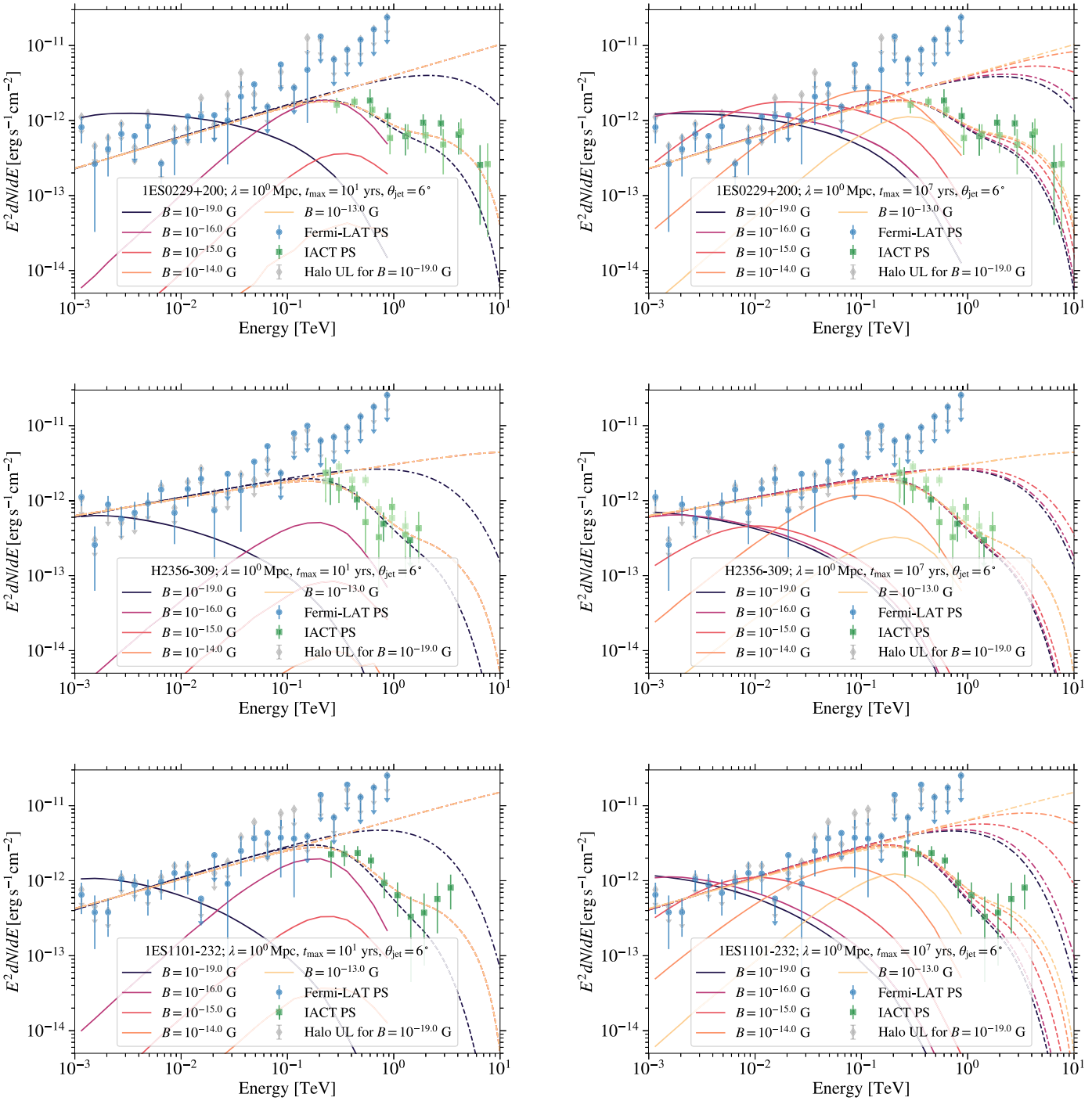

Figure 18. Same as Figure 16 (left) for the TeV detected blazars 1ES 0229+200, H 2356–309, and 1ES 1101–232 that yield constraints on the IGMF. The left column shows the constraints for $t_{max} = 10$ years, while the right column shows results for $t_{max} = 10^7$ years.

In Figure 20, we show the r_{68} extension of the halo as a function of energy for the case of $t_{max} = 10^7$ years. For the smaller values of t_{max} considered here, too many cascade photons are lost to lead to an extension beyond the *Fermi*-LAT PSF (shown by the dashed line).

Finally, in Table 10, we show the best-fit parameters of all six spectra that lead to constraints on the IGMF for the B-field values plotted in Figures 18 and 19 for $\lambda = 1$ Mpc, $t_{max} = 10$ years, and $\theta_{jet} = 6°$. The table shows that, for the high B-field values, the best-fit parameters do not change but are very different for the $B = 10^{-20}$ G, the lowest B field considered.

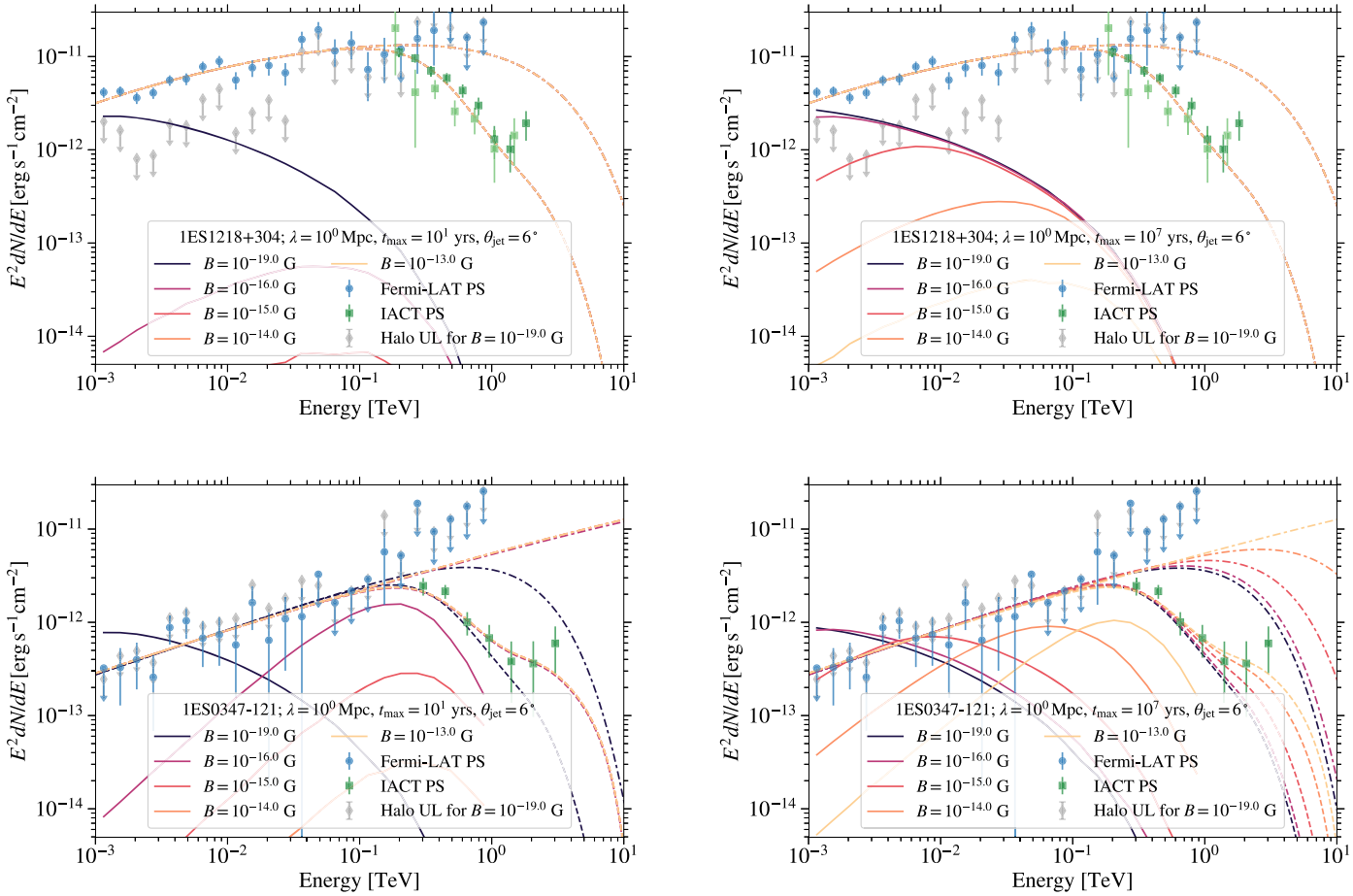

Figure 19. Same as Figure 18 for the TeV detected blazars 1ES 1218+304 and 1ES0347–121 that yield constraints on the IGMF.

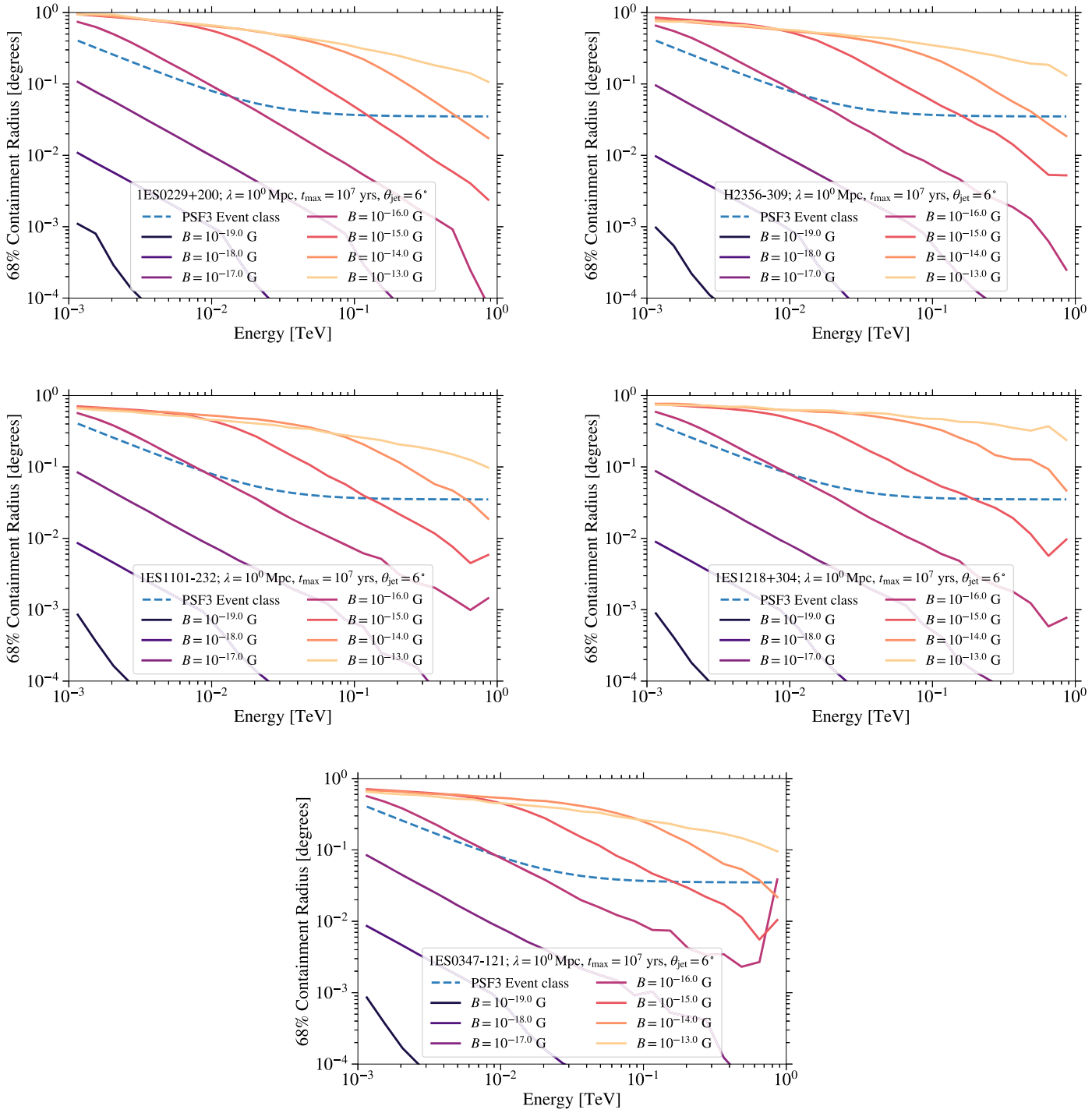

Figure 20. Same as Figure 16 (right) for the TeV-detected blazars that yield constraints on the IGMF, assuming a maximum activity time of $t_{max} = 10^7$ years.

Table 10
Best-fit Parameters for the Intrinsic Spectra of the Sources Used to Derive IGMF Constraints

$\log_{10}(B/\mathrm{G})$	N_0 ($10^{-13}\mathrm{TeV}^{-1}\mathrm{s}^{-1}\mathrm{cm}^{-2}$)	α	β (10^{-3})	E_{cut} (TeV)
		1ES0229+200		
−19.0	1.422	−1.569	0.000	4.834
−16.0	1.440	−1.587	0.000	⋯
−15.0	1.439	−1.586	0.000	⋯
		1ES0347–121		
−19.0	1.714	−1.515	0.000	1.319
−16.0	1.773	−1.524	7.483	⋯
−15.0	1.773	−1.523	6.867	⋯
		1ES0414+009		
−19.0	5.537	−1.769	0.000	0.265
		1RXSJ101015.9–311909		
−19.0	3.801	−1.500	43.932	7.680
−16.0	3.801	−1.500	43.932	7.680
		1ES1101–232		
−19.0	2.551	−1.565	0.000	1.725
−16.0	2.652	−1.605	0.000	⋯
		1ES1218+304		
−19.0	19.740	−1.528	35.404	2.589
−16.0	19.740	−1.528	35.404	2.589
		1ES1312–423		
−19.0	1.768	−1.500	34.197	2.537
−16.0	1.770	−1.500	34.983	3.044
		H2356–309		
−19.0	3.778	−1.735	0.000	2.627
−16.0	3.925	−1.769	0.000	⋯

Note. The same B-field strengths as in Figure 16 are used here. If they are not displayed in the table, the best-fit parameters are the same as for a lower B-field strength. Parameters are shown for $t_{\mathrm{max}} = 10$ years, $\lambda = 1$ Mpc, and $\theta_{\mathrm{jet}} = 6°$. If no value for E_{cut} is given, this fit parameter is unconstrained, i.e., the spectrum does not show an exponential cutoff.

Table 11
FHES Source Table Format (CATALOG HDU)

Column	Unit	Description
name[a]	...	Source designation
assoc_3fgl	...	3FGL Source association
assoc_3fhl	...	3FHL Source association
assoc_fl8y	...	Name of associated source in preliminary LAT eight-year point source list (FL8Y)
sep_fl8y	deg	Angular separation of between FHES source and associated source in FL8Y
assoc	...	Source association from 3FGL (column ASSOC1) or 3FHL (column ASSOC)
class	...	Source class from 3FGL (column CLASS1) or 3FHL (column CLASS)
redshift	...	Redshift from 3FHL or 3LAC
nupeak	Hz	Synchrotron peak frequency from 3FHL or 3LAC
RAJ2000[b]	deg	Right ascension of 3FGL or 3FHL source
DEJ2000[b]	deg	Declination of 3FGL or 3FHL source
GLON[b]	deg	Galactic longitude of 3FGL or 3FHL source
GLAT[b]	deg	Galactic longitude of 3FGL or 3FHL source
pos_r68[b]	deg	Symmetric statistical error (68%) on position
pos_r68_sys[b,c]	deg	Symmetric systematic error (68%) on position
pos_r95[b]	deg	Symmetric statistical error (95%) on position
index	...	Spectral slope at 1 GeV
index_err	...	Statistical error on index
index_sys_err[c]	...	Systematic error (1σ) on index
SpectrumType	...	Spectral type (PowerLaw, LogParabola, PLSuperExpCutoff)
ts	...	Detection test statistic (TS)
ts_ext	...	Extension test statistic TS_{ext}
ts_ext_sys[c]	...	Minimum extension test statistic (TS_{ext}) under bracketing models for systematics
ts_halo	...	Halo test statistic TS_{halo}
flux	$cm^{-2}\ s^{-1}$	Integrated photon flux (1 GeV—1 TeV)
flux_err	$cm^{-2}\ s^{-1}$	Statistical error (1σ) on flux
flux_sys_err[c]	$cm^{-2}\ s^{-1}$	Systematic error (1σ) on flux
eflux	MeV $cm^{-2}\ s^{-1}$	Integrated energy flux (1 GeV—1 TeV)
eflux_err	MeV $cm^{-2}\ s^{-1}$	Statistical error (1σ) on eflux
ext_model	...	Best-fit spatial morphology (RadialGaussian, RadialDisk, PointSource)
ext_r68[d]	deg	Best-fit extension (R_{ext})
ext_r68_err	deg	Statistical error (1σ) on ext_r68
ext_r68_sys_err[c]	deg	Systematic error (1σ) on ext_r68
ext_r68_ul95	deg	95% CL upper limit on ext_r68

Notes.
[a] The source designation is the FHES name for extended sources and the name of the associated 3FGL or 3FHL source for point sources.
[b] If the source was found to be extended, the measured position and position uncertainties from the FHES are given. If the source was found to be point-like, position and position uncertainties are taken from the 3FGL or 3FHL.
[c] Systematic uncertainties are only given for sources with detected extension listed in Tables 3 and 4.
[d] For sources best-fit with the disk model, $R_{ext} = 0.82R$, where R is the disk radius.

Appendix B
Catalog File Format

Complete analysis results for all FHES sources are provided in the gll_hes_v20.fits catalog file available at http://www-glast.stanford.edu/pub_data/1261/ and https://zenodo.org/record/1324474. This FITS catalog includes all analysis seeds with a detection TS > 25. The catalog file contains six FITS extensions. The contents of each extension are detailed in the following tables:

1. A CATALOG table with best-fit parameters and likelihood ratios (TS, TS_{ext}, and TS_{halo}) for each source (see Table 11).
2. An SED table with the likelihood profiles for the SEDs for each source (see Table 12).
3. Two tables LIKELIHOOD_FHES_SOURCES and LIKELIHOOD_IGMF_SOURCES with likelihood profiles versus flux and angular extension for the Gaussian, halo, and disk model for the sources with detected extension and the blazars used to derive limits on the IGMF, respectively (see Table 13). The likelihood profiles for other sources can be obtained from the authors upon request.
4. A SCAN_PARS table defining the grid values used in the LIKELIHOOD_FHES_SOURCES and LIKELIHOOD_IGMF_SOURCES tables (see Table 14).

Table 12
FHES Source SED Table Format (SED HDU)

Column	Format	Unit	Description
name[a]	...	...	Source designation
norm	24D	...	Normalization in each bin, in units of the reference model
norm_err	24D	...	Symmetric error on the normalization in each bin, in units of the reference model
norm_errp	24D	...	Upper 1σ error on the normalization in each bin, in units of the reference model
norm_errn	24D	...	Lower 1σ error on the normalization in each bin, in units of the reference model
norm_ul	24D	...	Upper limit on the normalization in each bin, in units of the reference model
norm_scan[b]	24×9D	...	Array of 24×9 normalization values for the profile likelihood scan
dloglike_scan	24×9D	...	Array of 24×9 delta-loglikelihood values for the profile likelihood scan in 24 energy bins and 9 scan points

Notes.
[a] The source designation is the FHES name for extended sources and the name of the associated 3FGL or 3FHL source for point sources.
[b] A row-wise multiplication with any of the ref columns in the EBOUNDS HDU can be used to convert this matrix to the respective unit.

Table 13
FHES Likelihood Table Format (LIKELIHOOD HDUs)

Column	Format	Unit	Description
name[a]	...	...	Source designation
ext_gauss_dloglike	31E	...	$\Delta \ln \mathcal{L}$ values for extension likelihood scan of 2D Gaussian ($R_{\rm ext}$)
ext_disk_dloglike	31E	...	$\Delta \ln \mathcal{L}$ values for extension likelihood scan of 2D Disk ($R_{\rm ext}$)
halo_dloglike	$15 \times 13 \times 61$E	...	$\Delta \ln \mathcal{L}$ values for halo likelihood grid scan ($R_{\rm halo}$, $\Gamma_{\rm halo}$, $F_{\rm halo}$)
halo_sed_dloglike	$15 \times 24 \times 61$E	...	$\Delta \ln \mathcal{L}$ values for halo SED likelihood grid scan ($R_{\rm halo}$, $E_{\rm ref}$, $F_{\rm halo}$)
halo_src_sed_dloglike	24×9E	...	$\Delta \ln \mathcal{L}$ values for halo_src_sed_eflux
halo_src_sed_eflux	24×9E	MeV cm^{-2} s^{-1}	Energy flux evaluation points for source SED likelihood scan

Note.
[a] The source designation is the FHES name for extended sources and the name of the associated 3FGL or 3FHL source for point sources.

Table 14
FHES Parameter Table Format (SCAN_PARS HDU)

Column	Format	Unit	Description
ext_r68	30D	deg	Evaluation points for likelihood scan versus source extension ($R_{\rm ext}$)
halo_r68	15D	deg	$R_{\rm halo}$ values for halo likelihood scan (halo_dloglike)
halo_index	13D	...	$\Gamma_{\rm halo}$ values for halo likelihood scan (halo_dloglike)
halo_eflux	61D	MeV cm^{-2} s^{-1}	$R_{\rm halo}$ values for halo likelihood scan (halo_dloglike)

Table 15
FHES SED Parameter Table Format (EBOUNDS HDU)

Column	Unit	Description
e_min	MeV	Lower edge of energy bin
e_max	MeV	Upper edge of energy bin
e_ref	MeV	Central energy of bin
ref_flux	cm^{-2} s^{-1}	Flux of the reference model in each bin
ref_eflux	MeV cm^{-2} s^{-1}	Energy flux of the reference model in each bin
ref_dnde	MeV^{-1} cm^{-2} s^{-1}	Differential flux of the reference model evaluated at the bin center

5. An EBOUNDS table defining the energy bins as well as reference flux values used in the LIKELIHOOD_FHES_SOURCES, LIKELIHOOD_IGMF_SOURCES, and SED tables (see Table 15).

ORCID iDs

M. Ajello https://orcid.org/0000-0002-6584-1703
L. Baldini https://orcid.org/0000-0002-9785-7726
J. Ballet https://orcid.org/0000-0002-8784-2977
D. Bastieri https://orcid.org/0000-0002-6954-8862
R. Bellazzini https://orcid.org/0000-0002-2469-7063
E. Bissaldi https://orcid.org/0000-0001-9935-8106
T. J. Brandt https://orcid.org/0000-0003-4087-1786
R. Caputo https://orcid.org/0000-0002-9280-836X
E. Charles https://orcid.org/0000-0002-3925-7802
C. C. Cheung https://orcid.org/0000-0002-4377-0174
J. Cohen-Tanugi https://orcid.org/0000-0001-9022-4232
F. D'Ammando https://orcid.org/0000-0001-7618-7527
A. Desai https://orcid.org/0000-0001-7405-9994
A. Franckowiak https://orcid.org/0000-0002-5605-2219
Y. Fukazawa https://orcid.org/0000-0002-0921-8837
S. Funk https://orcid.org/0000-0002-2012-0080
P. Fusco https://orcid.org/0000-0002-9383-2425
F. Gargano https://orcid.org/0000-0002-5055-6395
D. Gasparrini https://orcid.org/0000-0002-5064-9495
N. Giglietto https://orcid.org/0000-0002-9021-2888
M. Giroletti https://orcid.org/0000-0002-8657-8852
S. Guiriec https://orcid.org/0000-0001-5780-8770
E. Hays https://orcid.org/0000-0002-8172-593X
J. W. Hewitt https://orcid.org/0000-0001-5254-2248
G. Jóhannesson https://orcid.org/0000-0003-1458-7036
M. Kuss https://orcid.org/0000-0003-1212-9998
S. Larsson https://orcid.org/0000-0003-0716-107X
M. Lemoine-Goumard https://orcid.org/0000-0002-4462-3686
F. Longo https://orcid.org/0000-0003-2501-2270
F. Loparco https://orcid.org/0000-0002-1173-5673
P. Lubrano https://orcid.org/0000-0003-0221-4806
J. D. Magill https://orcid.org/0000-0001-9231-2965
S. Maldera https://orcid.org/0000-0002-0698-4421
A. Manfreda https://orcid.org/0000-0002-0998-4953
M. N. Mazziotta https://orcid.org/0000-0001-9325-4672
M. Meyer https://orcid.org/0000-0002-0738-7581
T. Mizuno https://orcid.org/0000-0001-7263-0296
M. E. Monzani https://orcid.org/0000-0002-8254-5308
A. Morselli https://orcid.org/0000-0002-7704-9553
I. V. Moskalenko https://orcid.org/0000-0001-6141-458X
N. Omodei https://orcid.org/0000-0002-5448-7577
V. S. Paliya https://orcid.org/0000-0001-7774-5308
J. S. Perkins https://orcid.org/0000-0001-9608-4023
M. Pesce-Rollins https://orcid.org/0000-0003-1790-8018
T. A. Porter https://orcid.org/0000-0002-2621-4440
S. Rainò https://orcid.org/0000-0002-9181-0345
R. Rando https://orcid.org/0000-0001-6992-818X
S. Razzaque https://orcid.org/0000-0002-0130-2460
O. Reimer https://orcid.org/0000-0001-6953-1385
C. Sgrò https://orcid.org/0000-0001-5676-6214
G. Spandre https://orcid.org/0000-0003-0802-3453
D. J. Suson https://orcid.org/0000-0003-2911-2025
H. Tajima https://orcid.org/0000-0002-1721-7252
L. Tibaldo https://orcid.org/0000-0001-7523-570X
D. F. Torres https://orcid.org/0000-0002-1522-9065
G. Tosti https://orcid.org/0000-0002-0839-4126
J. Biteau https://orcid.org/0000-0002-4202-8939

References

Abdalla, H., Abramowski, A., Aharonian, F., et al. 2017, arXiv:1702.08280
Abdo, A. A., Ackermann, M., Ajello, M., et al. 2010a, A&A, 523, A46
Abdo, A. A., Ackermann, M., Ajello, M., et al. 2010b, Sci, 328, 725
Abdo, A. A., Ackermann, M., Ajello, M., et al. 2010c, ApJS, 188, 405
Abdo, A. A., Ackermann, M., Ajello, M., et al. 2010d, ApJL, 710, L92
Abdo, A. A., Ackermann, M., Ajello, M., et al. 2010e, A&A, 512, A7
Abdo, A. A., Ackermann, M., Atwood, W. B., et al. 2008, Sci, 322, 1218
Abergel, A., Ade, P. A. R., Aghanim, N., et al. 2014, A&A, 571, A11
Ábrahám, P., Balázs, L. G., & Kun, M. 2000, A&A, 354, 645
Abrahams, R. D., Teachey, A., & Paglione, T. A. D. 2017, ApJ, 834, 91
Abramowski, A., Acero, F., Aharonian, F., et al. 2010, A&A, 516, A56
Abramowski, A., Acero, F., Aharonian, F., et al. 2012a, A&A, 538, A103
Abramowski, A., Acero, F., Aharonian, F., et al. 2012b, A&A, 542, A94
Abramowski, A., Acero, F., Aharonian, F., et al. 2013, MNRAS, 434, 1889
Abramowski, A., Aharonian, F., Ait Benkhali, F., et al. 2014, A&A, 562, A145
Abramowski, A., Aharonian, F., Ait Benkhali, F., et al. 2015, Sci, 347, 406
Acciari, V. A., Aliu, E., Arlen, T., et al. 2009, ApJ, 695, 1370
Acciari, V. A., Aliu, E., Arlen, T., et al. 2010a, ApJL, 709, L163
Acciari, V. A., Aliu, E., Arlen, T., et al. 2010b, ApJL, 715, L49
Acero, F., Ackermann, M., Ajello, M., et al. 2013, ApJ, 773, 77
Acero, F., Ackermann, M., Ajello, M., et al. 2015, ApJS, 218, 23
Acero, F., Ackermann, M., Ajello, M., et al. 2016a, ApJS, 223, 26
Acero, F., Ackermann, M., Ajello, M., et al. 2016b, ApJS, 224, 8
Acero, F., Aharonian, F., Akhperjanian, A. G., et al. 2011, A&A, 525, A45
Ackermann, M., Ajello, M., Albert, A., et al. 2017a, ApJ, 836, 208
Ackermann, M., Ajello, M., Albert, A., et al. 2017b, ApJ, 840, 43
Ackermann, M., Ajello, M., Allafort, A., et al. 2011, Sci, 334, 1103
Ackermann, M., Ajello, M., Allafort, A., et al. 2013, ApJ, 765, 54
Ackermann, M., Ajello, M., Atwood, W. B., et al. 2015, ApJ, 810, 14
Ackermann, M., Ajello, M., Atwood, W. B., et al. 2016a, ApJS, 222, 5
Ackermann, M., Ajello, M., Baldini, L., et al. 2016b, ApJ, 826, 1
Ackermann, M., Ajello, M., Baldini, L., et al. 2017c, ApJ, 843, 139
Ackermann, M., Albert, A., Atwood, W. B., et al. 2016c, A&A, 586, A71
Ackermann, M., Albert, A., Baldini, L., et al. 2012, ApJ, 747, 121
Aharonian, F., Akhperjanian, A., Beilicke, M., et al. 2003, A&A, 403, 523
Aharonian, F., Akhperjanian, A. G., Anton, G., et al. 2009, ApJL, 695, L40
Aharonian, F., Akhperjanian, A. G., Barres de Almeida, U., et al. 2007a, A&A, 473, L25
Aharonian, F., Akhperjanian, A. G., Barres de Almeida, U., et al. 2007b, A&A, 475, L9
Aharonian, F., Akhperjanian, A. G., Bazer-Bachi, A. R., et al. 2006, A&A, 449, 223
Aharonian, F., Akhperjanian, A. G., Bazer-Bachi, A. R., et al. 2007c, A&A, 470, 475
Aharonian, F., Akhperjanian, A. G., Bazer-Bachi, A. R., et al. 2008, A&A, 481, 401
Aharonian, F. A., Coppi, P. S., & Voelk, H. J. 1994, ApJL, 423, L5
Ajello, M., Atwood, W. B., Baldini, L., et al. 2017, ApJS, 232, 18
Akaike, H. 1974, ITAC, 19, 716
Aliu, E., Archambault, S., Arlen, T., et al. 2012, ApJ, 755, 118
Aliu, E., Archambault, S., Arlen, T., et al. 2013, ApJ, 764, 38
Aliu, E., Archambault, S., Arlen, T., et al. 2014, ApJ, 782, 13
Alves Batista, R., Saveliev, A., Sigl, G., & Vachaspati, T. 2016, PhRvD, 94, 083005
Ando, S., & Kusenko, A. 2010, ApJL, 722, L39
Araya, M. 2018, MNRAS, 474, 102
Archambault, S., Archer, A., Benbow, W., et al. 2017a, ApJ, 836, 23
Archambault, S., Archer, A., Benbow, W., et al. 2017b, ApJ, 835, 288
Arlen, T. C., Vassilev, V. V., Weisgarber, T., Wakely, S. P., & Yusef Shafi, S. 2014, ApJ, 796, 18
Atwood, W., Albert, A., Baldini, L., et al. 2013, arXiv:1303.3514
Atwood, W. B., Abdo, A. A., Ackermann, M., et al. 2009, ApJ, 697, 1071
Bartoli, B., Bernardini, P., Bi, X. J., et al. 2014, ApJ, 790, 152
Bertoni, B., Hooper, D., & Linden, T. 2016, JCAP, 5, 049
Biteau, J., & Williams, D. A. 2015, ApJ, 812, 60
Bonnoli, G., Tavecchio, F., Ghisellini, G., & Sbarrato, T. 2015, MNRAS, 451, 611
Broderick, A. E., Chang, P., & Pfrommer, C. 2012, ApJ, 752, 22

Buckley, M. R., Charles, E., Gaskins, J. M., et al. 2015, PhRvD, 91, 102001
Buckley, M. R., & Hooper, D. 2010, PhRv, D82, 063501
Bykov, A. M. 2014, A&ARv, 22, 77
Bykov, A. M., & Toptygin, I. N. 2001, AstL, 27, 625
Caprini, C., & Gabici, S. 2015, PhRvD, 91, 123514
Caprioli, D. 2015, Proc. ICRC (The Hague), 34, 8
Caputo, R., Buckley, M. R., Martin, P., et al. 2016, PhRvD, 93, 062004
Chang, P., Broderick, A. E., Pfrommer, C., et al. 2016, ApJ, 833, 118
Chaves, R. C. G., Renaud, M., Lemoine-Goumard, M., & Goret, P. 2008, in AIP Conf. Ser 1085, High-energy Gamma-ray Astronomy (Melville, NY: AIP), 372
Chen, W., Buckley, J. H., & Ferrer, F. 2015a, PhRvL, 115, 211103
Chen, W., Chowdhury, B. D., Ferrer, F., Tashiro, H., & Vachaspati, T. 2015, MNRAS, 450, 3371
Chen, W., Chowdhury, B. D., Ferrer, F., Tashiro, H., & Vachaspati, T. 2015b, MNRAS, 450, 3371
Chernoff, H. 1954, Ann. Math. Statist., 25, 573
Condon, B., Lemoine-Goumard, M., Acero, F., & Katagiri, H. 2017, ApJ, 851, 100
Condon, J. J., Cotton, W. D., Greisen, E. W., et al. 1998, AJ, 115, 1693
de Gasperin, F., Evoli, C., Brüggen, M., et al. 2014, A&A, 568, A107
de Naurois, M. & H.E.S.S. Collaboration 2013, AdSpR, 51, 258
Dermer, C. D., Cavadini, M., Razzaque, S., et al. 2011, ApJL, 733, L21
Dolag, K., Kachelrieß, M., Ostapchenko, S., & Tomàs, R. 2009, ApJ, 703, 1078
Dolag, K., Kachelriess, M., Ostapchenko, S., & Tomàs, R. 2011, ApJL, 727, L4
Domínguez, A., Primack, J. R., Rosario, D. J., et al. 2011, MNRAS, 410, 2556
Dubner, G., Castelletti, G., Kargaltsev, O., et al. 2017, ApJ, 840, 82
Durrer, R., & Neronov, A. 2013, A&ARv, 21, 62
Dwek, E., & Krennrich, F. 2013, APh, 43, 112
Finke, J. D., Razzaque, S., & Dermer, C. D. 2010, ApJ, 712, 238
Finke, J. D., Reyes, L. C., Georganopoulos, M., et al. 2015, ApJ, 814, 20
Fitoussi, T., Belmont, R., Malzac, J., et al. 2017, MNRAS, 466, 3472
Ghisellini, G., Righi, C., Costamante, L., & Tavecchio, F. 2017, MNRAS, 469, 255
Gould, R. J., & Schréder, G. P. 1967a, PhRv, 155, 1408
Gould, R. J., & Schréder, G. P. 1967b, PhRv, 155, 1404
Grondin, M.-H., Romani, R. W., Lemoine-Goumard, M., et al. 2013, ApJ, 774, 110
Hauser, M. G., & Dwek, E. 2001, ARA&A, 39, 249
Hester, J. J. 2008, ARA&A, 46, 127
Hillas, A. M., Akerlof, C. W., Biller, S. D., et al. 1998, ApJ, 503, 744
Holler, M., Berge, D., Hahn, J., Khangulyan, D., & Parsons, R. D. 2017, arXiv:1707.04196
Israel, F. 1998, A&ARv, 8, 237
Kachelrieß, M., Ostapchenko, S., & Tomàs, R. 2012, CoPhC, 183, 1036
Kashlinsky, A. 2005, PhR, 409, 361
Katsuta, J., Uchiyama, Y., & Funk, S. 2017, ApJ, 839, 129
Kerr, M., Ray, P., Johnston, S., Shannon, R., & Camilo, F. 2015, ApJ, 814, 128
Kharchenko, N. V., Piskunov, A. E., Schilbach, E., Röser, S., & Scholz, R.-D. 2013, A&A, 558, A53
Kinzer, R. L., Johnson, W. N., Dermer, C. D., et al. 1995, ApJ, 449, 105
Kotelnikov, E., Rubtsov, G., & Troitsky, S. 2015, MNRAS, 450, L44
Kuhlen, M., Diemand, J., & Madau, P. 2008, ApJ, 686, 262
Kun, M., Kiss, Z. T., & Balog, Z. 2008, in Handbook of Star Forming Regions Vol. I, ed. B. Reipurth (San Francisco, CA: ASP), 136
Lande, J., Ackermann, M., Allafort, A., et al. 2012, ApJ, 756, 5
Lang, C. C., Johnson, K. E., Goss, W. M., & Rodríguez, L. F. 2005, AJ, 130, 2185
Li, J., Torres, D. F., de Oña Wilhelmi, E., Rea, N., & Martin, J. 2016, ApJ, 831, 19
Lyne, A. G., Pritchard, R. S., & Graham-Smith, F. 1993, MNRAS, 265, 1003
Maurin, G., Marcowith, A., Komin, N., Krayzel, F., & Lamanna, G. 2016, A&A, 591, A71
Mayer-Hasselwander, H. A., Buccheri, R., Kanbach, G., et al. 1980, NYASA, 336, 211
Menzler, U., & Schlickeiser, R. 2015, MNRAS, 448, 3405
Meyer, M., Conrad, J., & Dickinson, H. 2016, ApJ, 827, 147
Meyer, M., Horns, D., & Zechlin, H.-S. 2010, A&A, 523, A2
Meyer, M., Raue, M., Mazin, D., & Horns, D. 2012, A&A, 542, A59
Mirabal, N., Frias-Martinez, V., Hassan, T., & Frias-Martinez, E. 2012, MNRAS, 424, L64
Neronov, A., Semikoz, D., Kachelriess, M., Ostapchenko, S., & Elyiv, A. 2010, ApJL, 719, L130
Neronov, A., & Semikoz, D. V. 2009, PhRvD, 80, 123012
Neronov, A., Semikoz, D. V., Tinyakov, P. G., & Tkachev, I. I. 2011, A&A, 526, A90
Neronov, A., & Vovk, I. 2010, Sci, 328, 73
Nikishov, A. I. 1962, JETP, 14, 393
Ohm, S., Hinton, J. A., & White, R. 2013, MNRAS, 434, 2289
Olive, K. A. 2003, arXiv:astro-ph/0301505
Parma, P., Murgia, M., de Ruiter, H. R., & Fanti, R. 2002, NewAR, 46, 313
Pieri, L., Bertone, G., & Branchini, E. 2008, MNRAS, 384, 1627
Pineault, S., Landecker, T. L., Swerdlyk, C. M., & Reich, W. 1997, A&A, 324, 1152
Plaga, R. 1995, Natur, 374, 430
Protheroe, R. J., & Stanev, T. 1993, MNRAS, 264, 191
Quireza, C., Rood, R. T., Bania, T. M., Balser, D. S., & Maciel, W. J. 2006, ApJ, 653, 1226
Remy, Q., Grenier, I. A., Marshall, D. J., & Casandjian, J. M. 2017, A&A, 601, A78
Reynoso, E. M., & Green, A. J. 2007, MNRAS, 375, 92
Rubin, V., Thonnard, N., & Ford, W. K. J. 1980, ApJ, 238, 471
Schlegel, D. J., Finkbeiner, D. P., & Davis, M. 1998, ApJ, 500, 525
Seward, F. D., Schmidt, B., & Slane, P. 1995, ApJ, 453, 284
Sironi, L., & Giannios, D. 2014, ApJ, 787, 49
Slane, P., Seward, F. D., Bandiera, R., Torii, K., & Tsunemi, H. 1997, ApJ, 485, 221
Slane, P., Zimmerman, E. R., Hughes, J. P., et al. 2004, ApJ, 601, 1045
Strong, A. W., Bignami, G. F., Bloemen, J. B. G. M., et al. 1982, A&A, 115, 404
Suárez, A. E., Combi, J. A., Albacete-Colombo, J. F., et al. 2015, A&A, 583, A84
Sun, X.-n., Yang, R.-z., Mckinley, B., & Aharonian, F. 2016, A&A, 595, A29
Swanenburg, B. N., Bennett, K., Bignami, G. F., et al. 1981, ApJL, 243, L69
Tavecchio, F., Ghisellini, G., Bonnoli, G., & Foschini, L. 2011, MNRAS, 414, 3566
Taylor, A. M., Vovk, I., & Neronov, A. 2011, A&A, 529, A144
Thompson, D. J., Bertsch, D. L., Dingus, B. L., et al. 1995, ApJS, 101, 259
Vovk, I., Taylor, A. M., Semikoz, D., & Neronov, A. 2012, ApJL, 747, L14
Wood, M., Caputo, R., Charles, E., et al. 2017, arXiv:1707.09551
Xia, Z.-Q., Duan, K.-K., Li, S., et al. 2017, PhRvD, 95, 102001
Yang, R.-Z., & Aharonian, F. 2017, A&A, 600, A107
Yang, R.-Z., de Oña Wilhelmi, E., & Aharonian, F. 2017, arXiv:1710.02803
Zechlin, H.-S., & Horns, D. 2012, JCAP, 1211, 050, (Erratum: 2015, JCAP, 1502, E01)
Zhu, H., Tian, W. W., & Wu, D. 2015, MNRAS, 452, 3470
Zwicky, F. 1933, AcHPh, 6, 110